

**MODELING AND CONTROL OF A LOW POWER  
ELECTRONICS CIRCUIT FOR ENERGY  
HARVESTING APPLICATIONS**

by

Shahrzad Faghihi

B.Sc., Imam Khomeini International University, 2009

A THESIS SUBMITTED IN PARTIAL FULFILLMENT  
OF THE REQUIREMENTS FOR THE DEGREE OF  
MASTER OF APPLIED SCIENCE  
in the School  
of  
Mechatronic Systems Engineering

© Shahrzad Faghihi 2011

SIMON FRASER UNIVERSITY

Fall 2011

All rights reserved. However, in accordance with the Copyright Act of Canada, this work may be reproduced without authorization under the conditions for Fair Dealing. Therefore, limited reproduction of this work for the purposes of private study, research, criticism, review and news reporting is likely to be in accordance with the law, particularly if cited appropriately.

## APPROVAL

**Name:** Shahrzad Faghihi  
**Degree:** Master of Applied Science  
**Title of Thesis:** Modeling and Control of a Low Power Electronics Circuit  
for Energy Harvesting Applications

**Examining Committee:** Dr. Siamak Arzanpour  
Chair

---

Dr. Mehrdad Moallem Senior Supervisor

---

Dr. Ahmad Rad Supervisor

---

Dr. Ash Parameswaran SFU External Examiner

**Date Approved:**

5 December 2011

---

## Partial Copyright Licence



The author, whose copyright is declared on the title page of this work, has granted to Simon Fraser University the right to lend this thesis, project or extended essay to users of the Simon Fraser University Library, and to make partial or single copies only for such users or in response to a request from the library of any other university, or other educational institution, on its own behalf or for one of its users.

The author has further granted permission to Simon Fraser University to keep or make a digital copy for use in its circulating collection (currently available to the public at the "Institutional Repository" link of the SFU Library website ([www.lib.sfu.ca](http://www.lib.sfu.ca)) at <http://summit/sfu.ca> and, without changing the content, to translate the thesis/project or extended essays, if technically possible, to any medium or format for the purpose of preservation of the digital work.

The author has further agreed that permission for multiple copying of this work for scholarly purposes may be granted by either the author or the Dean of Graduate Studies.

It is understood that copying or publication of this work for financial gain shall not be allowed without the author's written permission.

Permission for public performance, or limited permission for private scholarly use, of any multimedia materials forming part of this work, may have been granted by the author. This information may be found on the separately catalogued multimedia material and in the signed Partial Copyright Licence.

While licensing SFU to permit the above uses, the author retains copyright in the thesis, project or extended essays, including the right to change the work for subsequent purposes, including editing and publishing the work in whole or in part, and licensing other parties, as the author may desire.

The original Partial Copyright Licence attesting to these terms, and signed by this author, may be found in the original bound copy of this work, retained in the Simon Fraser University Archive.

Simon Fraser University Library  
Burnaby, British Columbia, Canada

# Abstract

In this thesis, we propose a new low power electronics converter for energy harvesting applications. The proposed converter exhibits a resistive input behavior which can be adjusted by using a controller. Furthermore, a self-powered MOSFET gate drive circuit is designed and tested that obtains its power from the input power source. These characteristics offer a huge advantage in dealing with harvestable sources of energy. The theoretical analysis of the circuit is done by deriving the mathematical formulas describing the behavior of the circuit, the extracted power, the harvested power in the battery, and the efficiency of the circuit. All the derived formulas and the theoretical analysis of the circuit are verified by simulation results using Matlab/Simulink environment and Ltspice. A vibrational piezoelectric transducer was used along with a PI controller to verify the theoretical and simulation results. The self-powered and low power consumption characteristics of the circuit are demonstrated in another experiment.

*To my family, especially my father for his support and hope and my mother for her love  
and sacrifices.*

# Acknowledgments

I would like to express my gratitude to everyone who helped me in this project. First of all, I would first like to thank my supervisor, Dr. Moallem for his advice, patience, and assistance. His guidance and inspiration have provided an invaluable experience that will help me in the rest of my life. I am also grateful to my committee members, Dr. Ash Parameswaran and Dr. Ahmad Rad for taking the time to serve as my committee members. My special thanks to my lab mates specially, Sepehr Attarchi, Ali ShagerdMootaab, Yaser Mohammadian Roshan, and Maryam Nasri for their continued support and kind suggestions and the friendly environment they provided in the lab.

Last but not least, I would like to thank my family in Iran. My father, for being an unending source of encouragement and hope and supporting my study at SFU. My mother for her constant love and support and sacrifices.

# Contents

<b>Approval</b>	<b>iii</b>
<b>Abstract</b>	<b>iv</b>
<b>Dedication</b>	<b>v</b>
<b>Acknowledgments</b>	<b>vi</b>
<b>Contents</b>	<b>vii</b>
<b>List of Tables</b>	<b>x</b>
<b>List of Figures</b>	<b>xi</b>
<b>1 Introduction</b>	<b>1</b>
<b>2 Literature Review</b>	<b>6</b>
2.1 Vibrational Energy . . . . .	6
2.1.1 Introduction . . . . .	6
2.1.2 Vibrational Energy Harvesting Circuits . . . . .	8
2.1.3 Vibrational Energy Harvesting Applications . . . . .	12
2.2 Solar Power . . . . .	16
2.2.1 Introduction . . . . .	16
2.2.2 Maximum Power Point Tracking Methods . . . . .	21
2.2.3 Solar cell power converters . . . . .	26

2.2.4	Solar Power Applications . . . . .	28
<b>3</b>	<b>Theoretical Analysis of the Proposed Circuit</b>	<b>31</b>
3.1	Introduction . . . . .	31
3.2	Theoretical Analysis . . . . .	31
3.3	Design of the Controller to Control the Input Resistance of the Converter . .	42
3.4	MOSFET Gate Drive Circuits . . . . .	45
3.4.1	MOSFET Gate Drive Circuit Using Positive Feedback . . . . .	45
3.4.2	Self-Powered MOSFET Gate Drive Circuit . . . . .	47
3.5	Harvested Power and Efficiency of the Circuit . . . . .	56
3.5.1	Harvested Power in the Battery . . . . .	56
3.5.2	Extracted Power . . . . .	58
3.5.3	Efficiency of the Low Power Electronics Circuit . . . . .	59
3.6	Applications of the Proposed Low-Power Electronics Circuitry . . . . .	60
3.6.1	Harvesting solar energy using solar cell . . . . .	60
3.6.2	Harvesting Vibrational Energy using Piezoelectric Transducers . . .	62
<b>4</b>	<b>Simulation Studies of the Proposed Circuit</b>	<b>63</b>
4.1	Introduction . . . . .	63
4.2	Simulation Studies of the Proposed Circuit Using Independent Voltage Source	63
4.3	Simulations Studies of the Proposed Circuit using Self-Powered Driven Cir-	
cuit	. . . . .	70
4.4	Conclusion . . . . .	74
<b>5</b>	<b>Experimental Studies of the Proposed Circuit</b>	<b>76</b>
5.1	Experimental Studies of the Proposed Converter using Independent Voltage	
Source	. . . . .	77
5.1.1	Circuit Implementation . . . . .	77
5.1.2	Experimental results . . . . .	79
5.2	Experimental Studies of the Proposed Converter using Feedback Controller	84
5.2.1	Circuit Implementation . . . . .	84



5.2.2	Experimental Results . . . . .	85
5.3	Experimental Studies of the Proposed Converter using Self-Powered Driven Circuit . . . . .	90
5.3.1	Circuit Implementation . . . . .	90
5.3.2	Experimental Results . . . . .	91
5.4	Conclusion . . . . .	94
<b>6</b>	<b>Conclusions and Future Work</b>	<b>95</b>
<b>A</b>	<b>Duracell Rechargeable Battery</b>	<b>97</b>
<b>B</b>	<b>Power MOSFET, (IRF540)</b>	<b>99</b>
<b>C</b>	<b>Switching Diode (IN4148),</b>	<b>102</b>
<b>D</b>	<b>Optocoupler (4N26),</b>	<b>105</b>
<b>E</b>	<b>NPN Switching Transistor (PN2222A)</b>	<b>108</b>
<b>F</b>	<b>Surface Mount Schottkey Barrier Diode (BAT43WS)</b>	<b>111</b>
<b>G</b>	<b>Low Threshold Voltage (SI1563EDH)</b>	<b>113</b>
<b>H</b>	<b>Op-amp (LT6004)</b>	<b>116</b>

# List of Tables

- 1.1 Battery operated versus energy harvesting sensor. . . . . 3
- 2.1 Ranking of major Canadian cities in terms of yearly PV potential. Table from [36]. . . . . 18

# List of Figures

1.1	Power requirement for processors. [1]. . . . .	1
1.2	Advances in battery technology and computing technology [2]. . . . .	2
1.3	Power density for different sources of power. Image from [9]. . . . .	3
1.4	Bridge collapse in Minneapolis, 2007. . . . .	5
2.1	Principle of operation of piezoelectric. . . . .	7
2.2	Piezoelectric transducer model. . . . .	7
2.3	Energy Harvesting circuit using a step-down DC-DC converter proposed in [13], [14]. . . . .	8
2.4	Steady-state battery current as a function of duty cycle for energy harvesting circuit presented in [13] , [14] . Image from [13] , [14] . . . . .	9
2.5	Efficiency of the energy harvesting circuit presented in [13] , [14] . Image from [13] , [14] . . . . .	10
2.6	Energy harvesting circuitry using flyback switching mode DC-DC converter proposed in [16]. . . . .	10
2.7	Energy harvesting circuit using Synchronized Switch Harvesting on Inductor, SSHI technique proposed in [17]- [19]. . . . .	11
2.8	Energy harvesting circuit using SSHI-in parallel method proposed in [21]. . . . .	11
2.9	Experimental and theoretical results of standard and SSHI circuits proposed in [17]. Image from [17]. . . . .	12
2.10	Buck-Boost converter proposed in [22] for vibrational energy harvesting. . . . .	13
2.11	Piezoelectric-powered Radio Frequency Identification Tag shoes. Image from [24]. . . . .	13

2.12	Wearable knee mounted prototype energy harvester presented in [26]. . . . .	14
2.13	Harvesting short duration vibration of passing vehicles in a road. Image from [28], [29]. . . . .	15
2.14	Energy harvesting using a pushbutton. Image from [30]. . . . .	16
2.15	Yearly PV potential map in Canada. Image from [36]. . . . .	17
2.16	Generating electricity using PV. . . . .	19
2.17	Solar panel. . . . .	19
2.18	Solar cell, solar module, and solar array. . . . .	20
2.19	Solar cell model. . . . .	20
2.20	Characteristics of a PV array. . . . .	21
2.21	slop of i-v curve at $V_{OC}$ and $I_{SC}$ . . . . .	22
2.22	The influence of temperature on I-V curve of a solar cell. . . . .	22
2.23	The influence of light on I-V curve of a solar cell. . . . .	23
2.24	The effect of changing atmosphere conditions on tracking MPP of the i-v curve of a solar panel using Hill-Climbing / Perturb and Observe methods .	25
2.25	Efficiency of MPPT algorithms: incremental conductance technique (ICT) and P&O method. Image from [54] . . . . .	25
2.26	Commonly used DC to DC converter: (a) buck converter, (b) boost converter, (c) buck-boost converter . . . . .	27
2.27	Installing solar panels on the roof of a house. . . . .	28
2.28	Solar powered street light. . . . .	29
2.29	Solar Power Automatic Irrigation System. Image from [57]. . . . .	29
3.1	Power electronics circuit. . . . .	32
3.2	Power electronics circuit. . . . .	33
3.3	Voltage behavior of the rechargeable battery. Image from [62]. . . . .	33
3.4	Power electronics circuit. . . . .	34
3.5	Simplified power electronics circuit when MOSFET is on. . . . .	34
3.6	The waveform of capacitor voltage in one period of MOSFET switching, during second and third phases, while $i_{in}(t) > 0$ . . . . .	36

3.7	The waveform of capacitor voltage in one period of switching, during second and third phases, while $i_{in}(t) < 0$ .	36
3.8	The simplified waveform of $v_C$ in one period of MOSFET switching, during second and third phases, while $i_{in}(t) > 0$ .	39
3.9	The simplified waveform of $v_C$ in one period of switching during second and third phase, while $i_{in}(t) < 0$ .	40
3.10	Equivalent power electronics circuit.	41
3.11	Block diagram of a PI controller.	43
3.12	Positive feedback for MOSFET Driver.	45
3.13	Optocoupler	46
3.14	Energy harvesting circuit and peak detector	48
3.15	$V_S$ and $v_C$ in the peak detector	48
3.16	Low Frequency Oscillator Circuit.	49
3.17	Connection of low frequency oscillator to the circuit [?].	50
3.18	Internal circuit of an ideal opamp.	51
3.19	Waveforms of the opamp output and op amp inverting input terminal circuit shown on fig. 3.18.	51
3.20	Circuit to change the duty cycle of the PWM signal.	54
3.21	Energy harvesting circuit with self-powered MOSFET gate-drive.	55
3.22	Battery current in one period of MOSFET switching.	56
3.23	Current-Voltage curve of a solar cell.	61
3.24	Flowchart of Incremental Conductance Method.	61
4.1	Piezoelectric model.	64
4.2	Implementation of the piezoelectric transducer and energy harvesting circuit in Maltlab/ Simulink environment.	64
4.3	Circuit implementation in Maltlab/ Simulink environment.	65
4.4	Input voltage and current of the circuit for a single frequency mechanical vibration.	65
4.5	Input voltage and current of the circuit for a multi frequency mechanical vibration.	66

4.6	Input resistance of the converter as a function of switching frequency and duty cycle. . . . .	67
4.7	Piezoelectric voltage before and after applying the low-pass filter for a single frequency vibration. . . . .	67
4.8	Piezoelectric voltage before and after applying the low-pass filter for a multi-frequency frequency vibration. . . . .	68
4.9	Average power of the source and battery in one period of source signal. . .	68
4.10	Efficiency of the proposed energy harvesting circuit as a function of the duty cycle of the MOSFET switching . . . . .	69
4.11	Efficiency of the proposed converter as a function of the forward voltage drop of diodes in the diode bridge. . . . .	69
4.12	Implementing the piezoelectric transducer model and the converter in simulink environment. . . . .	71
4.13	Input current and voltage of the converter for a single frequency vibration. .	72
4.14	Input current and voltage of the converter for a multi frequency excitation. .	72
4.15	Charging of the capacitor when MOSFET is off ( $V_{gate-source} = 0V$ ) and discharging of the capacitor when MOSFET is on ( $V_{gate-source} = 10V$ ). . . .	73
4.16	Voltage across the piezoelectric before and after applying the low pass filter.	73
4.17	Theoretical and simulation results for the input resistance of the converter. .	74
4.18	The voltage across the storing capacitor of the peak detector. . . . .	74
5.1	Connection of float voltage source to the circuit. . . . .	77
5.2	Connection of the power electronics circuit, dSPACE, and the PC. . . . .	78
5.3	Power electronics circuit and the positive feedback . . . . .	79
5.4	Implementation of PI controller. . . . .	80
5.5	Experimental setup. . . . .	80
5.6	Capacitor Voltage $v_C$ and Voltage source $v_{in}$ waveforms. . . . .	81
5.7	Charging of the $C$ when MOSFET is off ( $V_{gate-source} = 0V$ ) and discharging of $C$ when MOSFET is on ( $V_{gate-source} = 10V$ ). . . . .	81
5.8	$v_C$ before and after passing through a low-pass-filter. . . . .	82

5.9	Capacitor voltage $v_C$ and voltage source $v_P$ for a multi-frequency excitation. . . . .	82
5.10	Input resistance of the buck converter circuit as a function of the duty cycle.	83
5.11	$v_{R_{eq}}$ and $R_{Pi}$ for a single frequency voltage source. . . . .	83
5.12	$v_{R_{eq}}$ and $R_{Pi}$ for a multi-frequency voltage source. . . . .	84
5.13	Piezoelectric transducer model. . . . .	85
5.14	Power Electronics Circuit. . . . .	86
5.15	Connection of piezoelectric transducer model and the Power Electronics Circuit. . . . .	86
5.16	Experimental setup. . . . .	87
5.17	Charging of the piezoelectric capacitor $C_P$ when MOSFET is off ( $V_{gate-source} < V_{Threshold}$ ) and discharging of the capacitor when MOSFET is on ( $V_{gate-source} > V_{Threshold}$ ) . . . . .	87
5.18	Piezoelectric voltage $v_P$ before and after passing through a low-pass filter. .	88
5.19	Input resistance of the buck converter circuit $R_{eq}$ as a function of duty cycle of the PWM signal. . . . .	89
5.20	Voltage and current of the piezoelectric transducer. . . . .	89
5.21	Converter wave-form in the feedback loop. . . . .	90
5.22	Piezoelectric transducer, the proposed converter, the peak detector and the MOSFET gate drive circuit. . . . .	92
5.23	Voltage across the hold capacitor, $C_S$ and the voltage across the piezoelectric transducer. . . . .	93
5.24	Voltage across the input of the buck converter $v_{R_{eq}}$ , and voltage of piezoelectric resistor $R_{Pi}$ for a single frequency excitation. . . . .	93

# Chapter 1

## Introduction

In recent years, the power requirement for electronic devices has been steadily decreasing. In [1], the power requirement for processors has been studied. The result of this work is shown in Fig. 1.1. As this figure illustrates, since 1990, the operating voltage of processors has decreased by 15 percent every year. But still these devices need battery as the power supply.

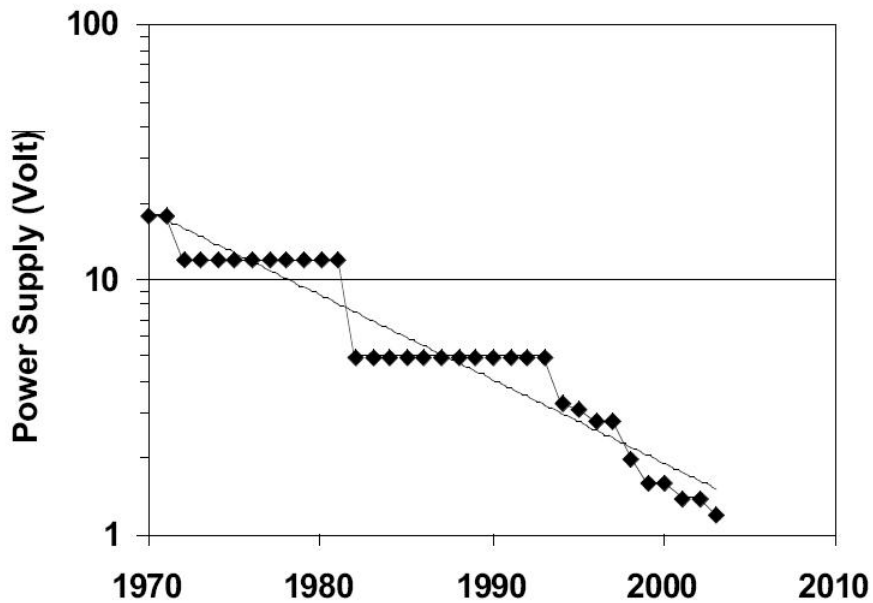


Figure 1.1: Power requirement for processors. [1].



The authors in [2] have done research on the growth of technology in different areas which reveals that the battery technology has not progressed along with the increasing power demands of current electronics. The result of this study is shown in Fig. 1.2. As this figure shows, battery energy has the slowest trend of improvement.

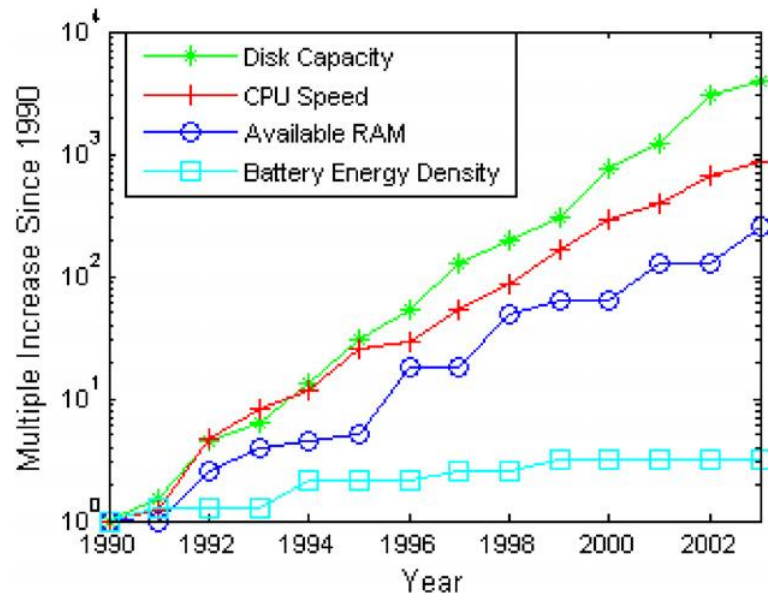


Figure 1.2: Advances in battery technology and computing technology [2].

The problem with batteries is that they have a limited lifespan. Therefore when the battery uses all of its power, it needs to be replaced. However this task could be expensive and challenging. Some applications do not tolerate the possibility of batteries dying without warning may cause serious problems in the case of security monitoring. Besides, the development of wireless monitoring systems has been of great interest because wireless transmission is a convenient means to transmit signals.

In [9], the authors compare the power density of solar power, mechanical vibrational energy, and batteries. The results of this paper are shown in Fig. 1.3 where different types of batteries (NiMh, Lithium, Alkaline, ...) are considered. As the figure illustrates, even the most advanced battery technologies are not sufficient to provide power to a wireless sensor node for several years. Table 1.1 demonstrates the comparison between the battery based sensor and energy harvesting sensor. As this table shows, by using energy from surrounding mediums to provide power to the wireless sensor node (WSN), there is no time limitation

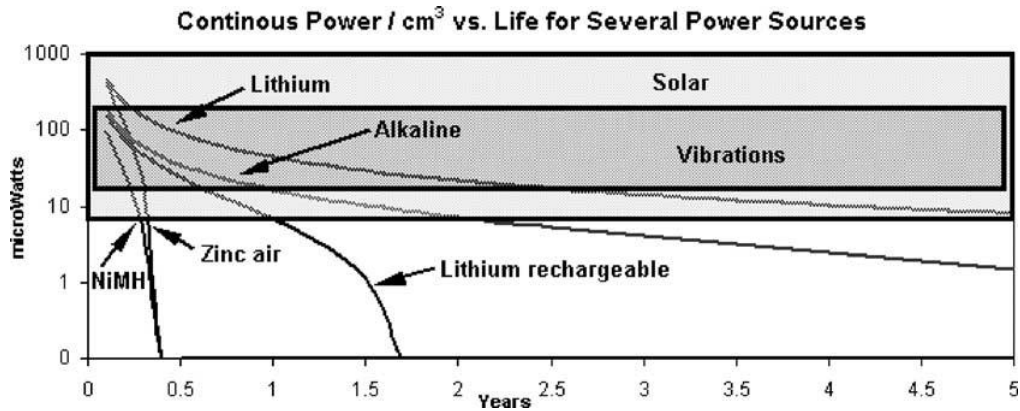


Figure 1.3: Power density for different sources of power. Image from [9].

Features	Battery Operated Sensor	Energy Harvesting Sensor
Energy Source	Charged battery	Surrounding environment
Maintenance cost	High, require recharge and replacement	Low, self-sustaining
Requirement	Energy efficient, Long-life battery	Energy-neutral
Quality of service	As low as possible/acceptable	As high as possible
Predictability	High, battery models	Low, fluctuation

Table 1.1: Battery operated versus energy harvesting sensor.

for the operation of the sensor.

Oftentimes, wireless sensors are placed in remote locations such as bridge structures or in global positioning systems (GPS) for tracking animals, where it is not easy to replace the battery. Moreover, in some locations there is no access to the utility grid (off grid locations) or it is costly to build the power grid. In these situations an alternative source of power is essential.

A great deal of research has been conducted in obtaining electrical energy from the surrounding mediums. The process of obtaining the energy surrounding a system and converting this energy into usable electrical energy is called power harvesting. Harvestable sources of energy are solar [3] - [6], flow of gases [7], ambient RF [8], thermal [10]. and mechanical [29]-[33],

Humans are a rich source of energy. An average-sized person stores as much energy in fat as a 1000-kg battery [11]. People use muscle to convert this stored chemical energy into positive mechanical work. Many research has been done on harvesting energy from every day human activities such as walking, mountain climbing, and sleeping.

By using a generator such as photovoltaic cells, thermoelectric generators (TEGs), thermopiles or piezoelectric transducers, we can convert the source of energy into electrical energy. Piezoelectric crystals generate a small voltage whenever they are mechanically deformed. Thermoelectric generators consist of the junction of two dissimilar materials and the presence of a thermal gradient. Large voltage outputs are possible by connecting many junctions electrically in series and thermally in parallel. Typical performance is  $100 - 200 \mu V / \text{degreeC}$  per junction.

Sometimes the source voltage is very low and must be up-converted to be useful, or even rectified and then down-converted so, the next step is using an energy harvesting circuit to store the harvested power in a temporary storage system such as an ultra capacitor or a rechargeable battery. This energy can then be used to provide the required power supply for electric devices that are used in transportation infrastructure, medical devices, tire pressure sensing, industrial sensing, building automation and asset tracking. These systems generally spend the majority of their operational lives in standby mode asleep requiring only a handful of  $\mu W$ . When awakened, a sensor measures parameters such as pressure, temperature or mechanical deflection and then transmits this data to a remote control system wirelessly. The entire measurement, processing and transmission time is usually only tens of milliseconds, but may require hundreds of mW of power for this brief period. Since the duty cycles of these applications are low, the average power that must be harvested can also be relatively low.

Another interesting energy harvesting application is using ambient energy is to monitor the health of architectural structures such as bridges. Embedded sensor systems, powered by energy-harvesting materials, can monitor bridge stresses such as those that led to the 2007 bridge collapse in Minneapolis, Mn, USA, and trigger warnings before they occur. Another energy harvesting application is human health monitoring. Sensors can be embedded in beds, sofas and, for example, in a room such as the kitchen, to determine the frequency of



Figure 1.4: Bridge collapse in Minneapolis, 2007.

human activities. Data collection can determine, for example, how many times an individual stepped on a particular area and how much time was spent lying on a bed or sofa.

The area of energy harvesting is not new but building efficient energy harvesting circuits is still a key research challenge. For example, in harvesting solar energy using solar cells, there is an operating point that the maximum power can be harvested from the solar cell. Thus, the energy harvesting circuit should direct the operating point of the solar cell to work at that specific point to harvest the maximum power. In this regard, different techniques and different energy harvesting circuits has been proposed.

In harvesting mechanical vibration using piezoelectric transducers, the generated power is very low, in the range of mW. Therefore, maximizing the efficiency of the energy harvesting circuit and power consumption are very important.

# Chapter 2

## Literature Review

### 2.1 Vibrational Energy

#### 2.1.1 Introduction

One of the harvestable source of energy is mechanical vibration. There are environments that are exposed to ambient vibration such as bridges, roads, and rail tracks. Thus vibration is an abundant source of harvestable energy. There are several methods to harvest vibrational energy and convert it to electrical energy. In this regard, piezoelectric materials have received attention because these materials can directly convert the applied strain into electric charge [12].

Piezoelectric materials are composed of polar molecules aligned along a certain axis, and therefore present a dipolar moment. Dipolar moment is the magnitude of the charge times the distance between one pair of opposite charges. By applying a mechanical strain, some of the mechanical work done on the device is stored in the electric field. as a result of modification the distance between the dipoles. This effect is shown in Fig. 2.1. Fig. 2.2 illustrates the vibrational piezoelectric model which consists of an ac current source in parallel with a capacitor, represented by  $C_P$  and a resistor, denoted by  $R_P$ .

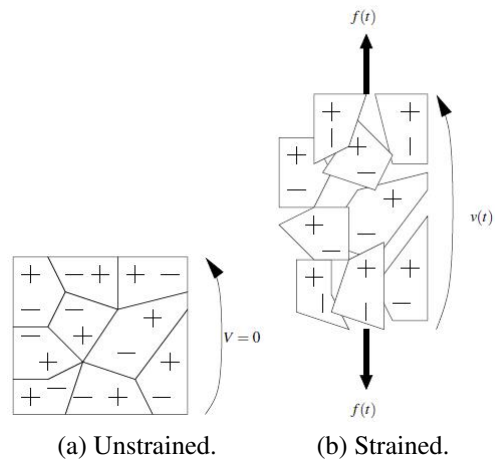


Figure 2.1: Principle of operation of piezoelectric.

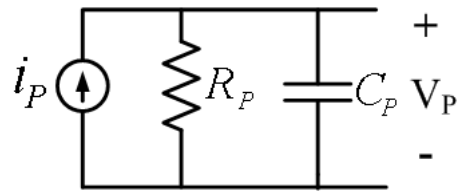


Figure 2.2: Piezoelectric transducer model.

### 2.1.2 Vibrational Energy Harvesting Circuits

The harvested energy from a vibrational piezoelectric device is very low in the range of  $\mu W$ . A great deal of research has been done in designing energy harvesting circuits with efficiency. In this regard, [13], [14] suggested an energy harvesting circuit to optimize the harvested vibrational energy. The proposed circuit is shown in Fig. 2.3 which consists of an ac-dc rectifier (full diode bridge) with an output capacitor and a step-down DC-DC converter that operates in the discontinuous conduction mode. The step down converter was chosen because the piezoelectric voltage is often relatively high, in the range of 10 to 30 volts which must be reduced to the voltage of the battery. In this work, it is proven that there is an optimum duty cycle that the harvested power would be maximum as shown in Fig. 2.4. As this figure shows, at a specific duty cycle, the current that flows into the battery and charges the battery is maximum.

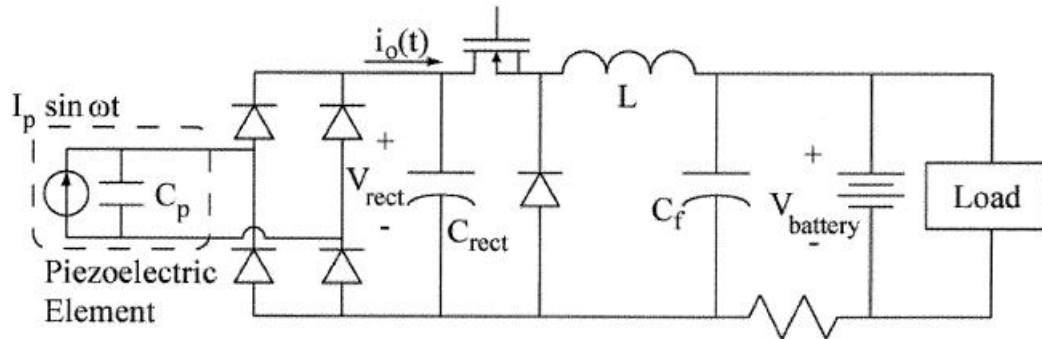


Figure 2.3: Energy Harvesting circuit using a step-down DC-DC converter proposed in [13], [14].

It was shown that optimal duty cycle of the converter is a function of the excitation frequency. Thus the proposed circuit works just for single frequency vibrations which may be a disadvantage when the frequency varies. Besides, theoretical analysis proves that the value of optimal duty cycle changes at low excitations and becomes constant as the mechanical excitation frequency increases. The efficiency of the converter was calculated to be between 0% and 70%, depending on excitation frequency. The proposed energy harvesting circuit achieves the maximum efficiency when the mechanical excitation produces 48V across the piezoelectric transducer as shown in Fig. 2.5. The proposed energy harvesting

circuit was further improved in [15]. In this paper, an adaptive algorithm was proposed that actively changes the duty cycle of the DC-DC converter during operation. It was found that the charge accumulation of the battery is faster, but the power consumption of the adaptive circuitry was not considered.

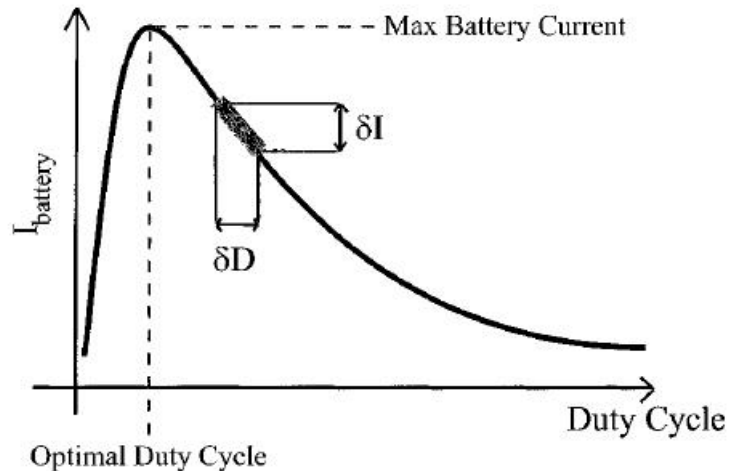


Figure 2.4: Steady-state battery current as a function of duty cycle for energy harvesting circuit presented in [13] , [14] .  
Image from [13] , [14]

In [16], a self-adaptive power harvesting circuit has been developed. The proposed circuit consists of a rectifying diode bridge and a flyback switching mode DC-DC converter as shown in Fig. 2.6. When the absolute value of the energy that is stored in the piezoelectric capacitor reaches a maximum, or in other words, when the voltage across the piezoelectric reaches a maximum, the flyback converter is activated by the control circuit. In this case, the electric charge on the piezoelectric transducers is transferred to the battery. The method that is proposed in this paper is called “synchronous electric charge extraction” because the charge extraction is synchronized with the mechanical vibration of the system. The efficiency of the suggested energy harvesting circuit was found to be 70% when the output voltage of the flyback converter (the voltage across the load or battery) is in the range of 5 V to 25 V. Moreover, the suggested circuit has many elements which results in increasing the cost of the circuit. Also, the controller circuit is not presented in the paper.

In [17]- [19] a nonlinear process called Synchronized Switch Harvesting on Inductor (SSHI)



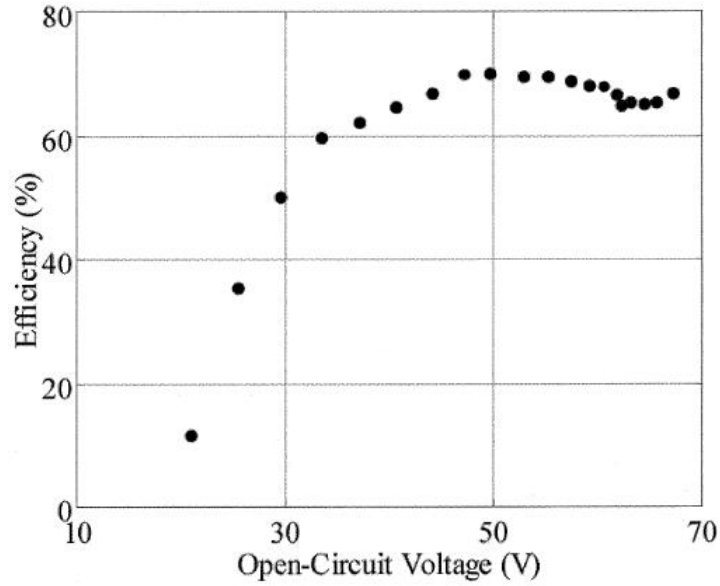


Figure 2.5: Efficiency of the energy harvesting circuit presented in [13] , [14] .  
Image from [13] , [14]

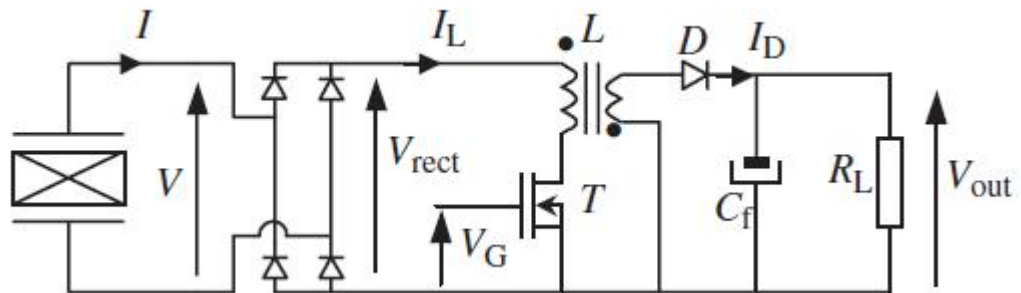


Figure 2.6: Energy harvesting circuitry using flyback switching mode DC-DC converter proposed in [16].

was proposed. The technique proposed in this paper as it is shown in Fig. 2.7, which consists of a switch and an inductor connected in series and placed in parallel with piezoelectric element. When displacement reaches a maximum, the switch is closed, the capacitor in the piezoelectric element and the inductance constitute an oscillator. The switch is closed for a half period of the oscillation ( $t = \pi\sqrt{c+L}$ ) until the voltage across the piezoelectric element is reversed and all of the charge has been removed. In [21], a new configuration of SSHI technique is proposed. This circuit is very similar to the parallel SSHI but the switching device and the inductor are placed in series with the piezoelectric element, as it is shown in Fig. 2.8. Both SSHI techniques (serial and parallel) are compared to standard energy harvesting circuit which consists of a an ac-dc rectifier and a capacitor. The results show that under a constant displacement excitation environment, these two circuits have a higher efficiency than the standard circuit shown in Fig. 2.9.

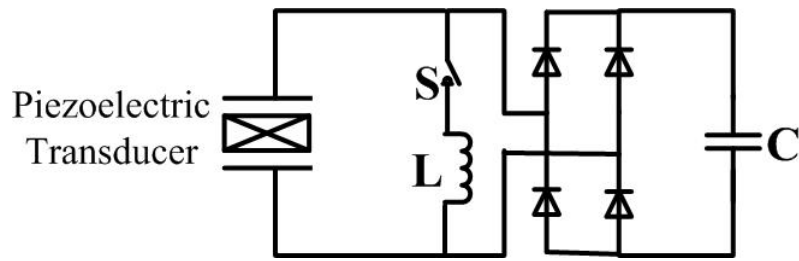


Figure 2.7: Energy harvesting circuit using Synchronized Switch Harvesting on Inductor, SSHI technique proposed in [17]- [19].

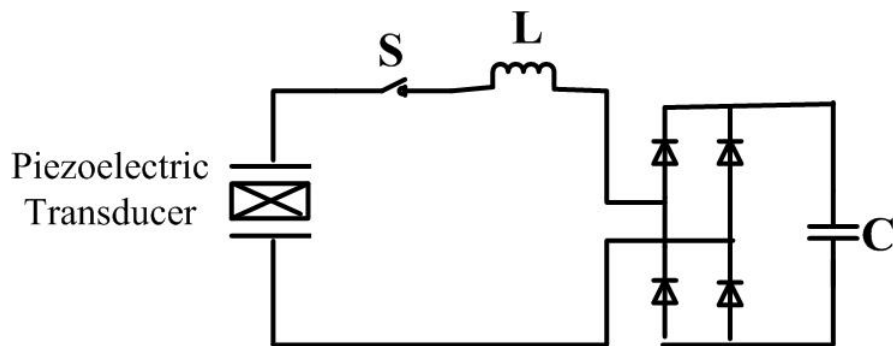


Figure 2.8: Energy harvesting circuit using SSHI-in parallel method proposed in [21].

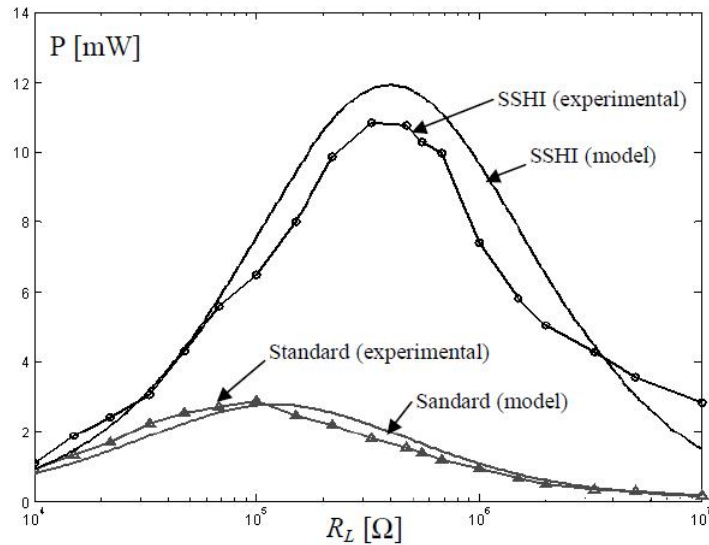


Figure 2.9: Experimental and theoretical results of standard and SSHI circuits proposed in [17].

Image from [17].

In [22], a buck-boost converter that works in the discontinuous conduction mode is suggested to harvest vibrational energy using a piezoelectric generator. As Fig. 2.10 shows, the proposed circuit consists of a full diode bridge, a smoothing capacitor and a DC-DC converter. The buck-boost converter is controlled to track the generator's optimal working point. This energy harvesting circuit was found to have an efficiency of between 71% to 79% for input voltages between 1.6 and 5.5 V. Besides the controller circuit needs a power supply in the range of 1.2 V to 5.5 V. This range of voltage imposes a limitation on the mechanical excitation level that is applied to the piezoelectric transducer.

### 2.1.3 Vibrational Energy Harvesting Applications

In recent years the use of wearable devices has growth significantly. These devices need battery to provide power to the electronics inside the devices. Decreasing the power requirement for these devices, has attracted interest of many researchers to develop systems to harvest energy lost in everyday human life. In [23], generating power from human body activities and using this energy in different applications are studied. They studied different

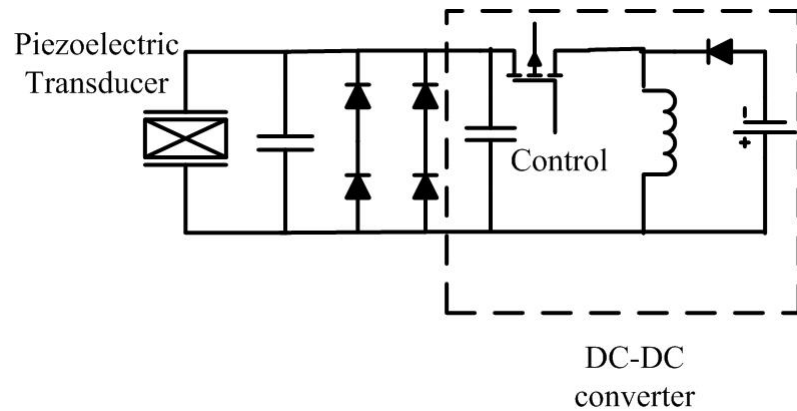


Figure 2.10: Buck-Boost converter proposed in [22] for vibrational energy harvesting.

human activities such as pushing a button or squeezing a hand and they investigated the amount of power that be generated in each activity.

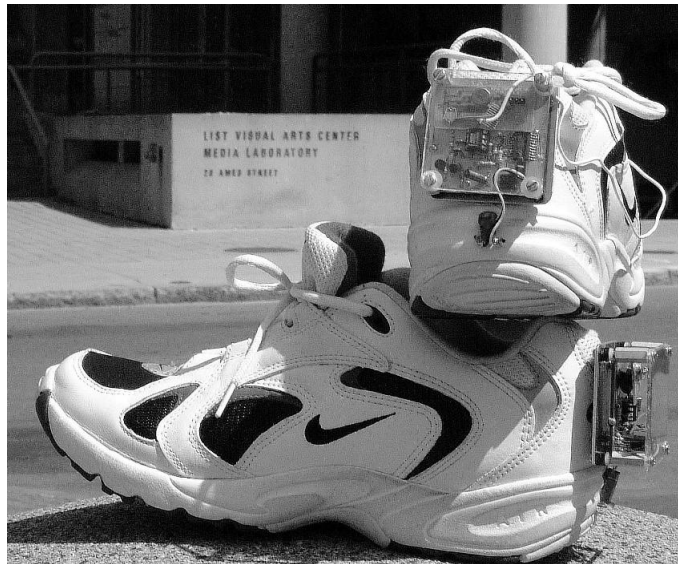


Figure 2.11: Piezoelectric-powered Radio Frequency Identification Tag shoes. Image from [24].

In [24], S. Shenk et.al. harvested the energy that is dissipated in bending the ball of the foot using PVDF bimorphs mounted under the insole. They also harvested foot strike energy using PZT under the heel of a US navy work boot. To demonstrate the feasibility

and usefulness of the energy harvesting in shoes, a radio frequency transmitter tag was installed into an athletic shoe as shown in Fig. 2.11. It was shown that this tag is capable of transmitting a 12-bit wireless identification code while walking.

In [25], it is shown that by inserting two piezoelectric films parallel into a shoe, the charge generation will increase and the results show that  $18\mu W$  could be harvested using this method under specific conditions. In [26], a wearable knee mounted prototype energy harvester is proposed as shown in Fig. 2.12. The results of this research show that an average of 5 watts of electricity can be generated by mounting the energy harvester device on each leg.

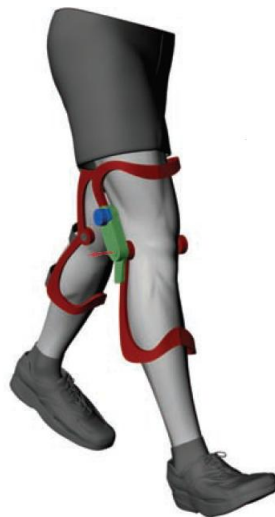


Figure 2.12: Wearable knee mounted prototype energy harvester presented in [26].

In [27] an energy harvesting system for generating electricity from a backpack instrumented with piezoelectric polymer polyvinylidene fluoride (PVDF) shoulder straps was developed. The result of this work showed that  $45.6mW$  of power could be obtained from this system. In [28], [29], the short duration vibrations of passing vehicles in a road was used to power a wireless sensor to measure traffic flow rate and the vehicles weight as illustrated in Fig. 2.13. In this study, to develop a low power control algorithm that can be implemented on the sensor, three control algorithms were developed and tested. The authors claim that the proposed sensor is reliable, low cost, and can be installed easily.

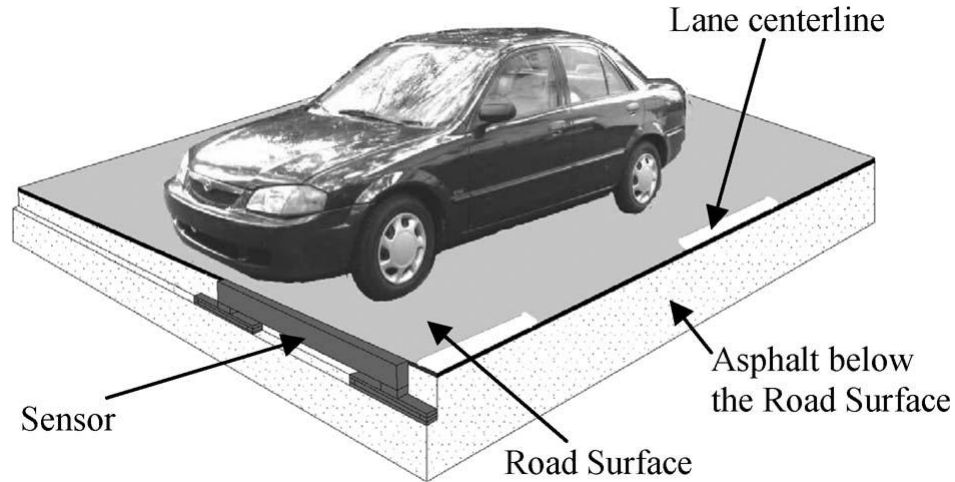


Figure 2.13: Harvesting short duration vibration of passing vehicles in a road.  
Image from [28], [29].

In [30], it is shown that harvesting mechanical force from depressing a pushbutton is sufficient to power a radio frequency unit. In this research, a self-contained piezoelectric pushbutton is attached to an energy harvesting circuitry as shown in Fig. 2.14, which contains of a full diode bridge rectifier and a capacitor to store the energy. The results show that two complete 12-bit digital word information can be transmitted by the wireless radio transmitter.

The feasibility of piezoelectric energy harvesting from pneumatic tires is studied in [31] and the results of this research show that 8.4 mW electrical power output from the system. In [32] the possibility of harvesting vibrational energy using a PZT decoupler retrofitted in a hydraulic engine mount is investigated.

Another relevant area is the research activities in the field of low-power and low cost wireless sensor nodes. One application would be monitoring indoor environments for climate control. In [33], a sensor node is mounted on a wooden staircase and a piezoelectric is used to harvest vibrational energy generated as a result of walking on the staircase. This piezoelectric transducer is able to generate sufficient electricity for the sensor. The sensor node contains a temperature sensor and a wireless radio. The prototype detailed in this paper requires 50 minutes of continuous staircase traffic from two people to acquire and transmit a set of two temperature reading.

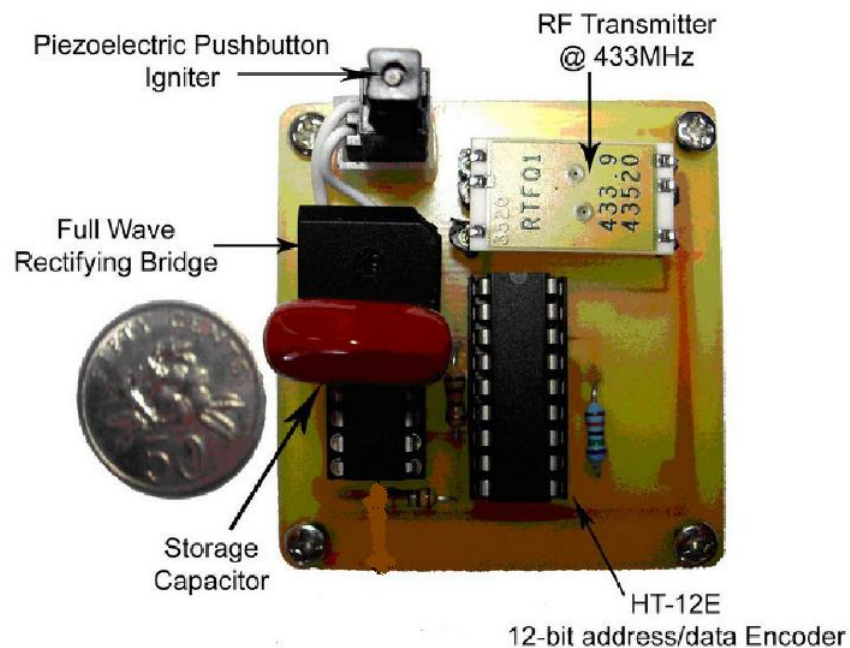


Figure 2.14: Energy harvesting using a pushbutton.  
Image from [30].

The harvestable vibrational energy using a piezoelectric element is relatively small, usually in micro-watt power or below. Usually an energy storage device is used to store and accumulate the harvested energy. In [34], a capacitor is used to store the energy. In [35], it is shown that rechargeable batteries can be used to store the harvested energy from the mechanical vibration using piezoelectric device.

## 2.2 Solar Power

### 2.2.1 Introduction

With the threat of global warming, and the gradual depletion of petroleum supplies, another source of power such as wind power or solar energy should be used. Fig. 2.15 shows the yearly photovoltaic (PV) potential map in Canada and the 13 "PV hotspots" in each province of Canada. Table. 2.1 illustrates the ranking of major Canadian cities and in terms of yearly PV potential.

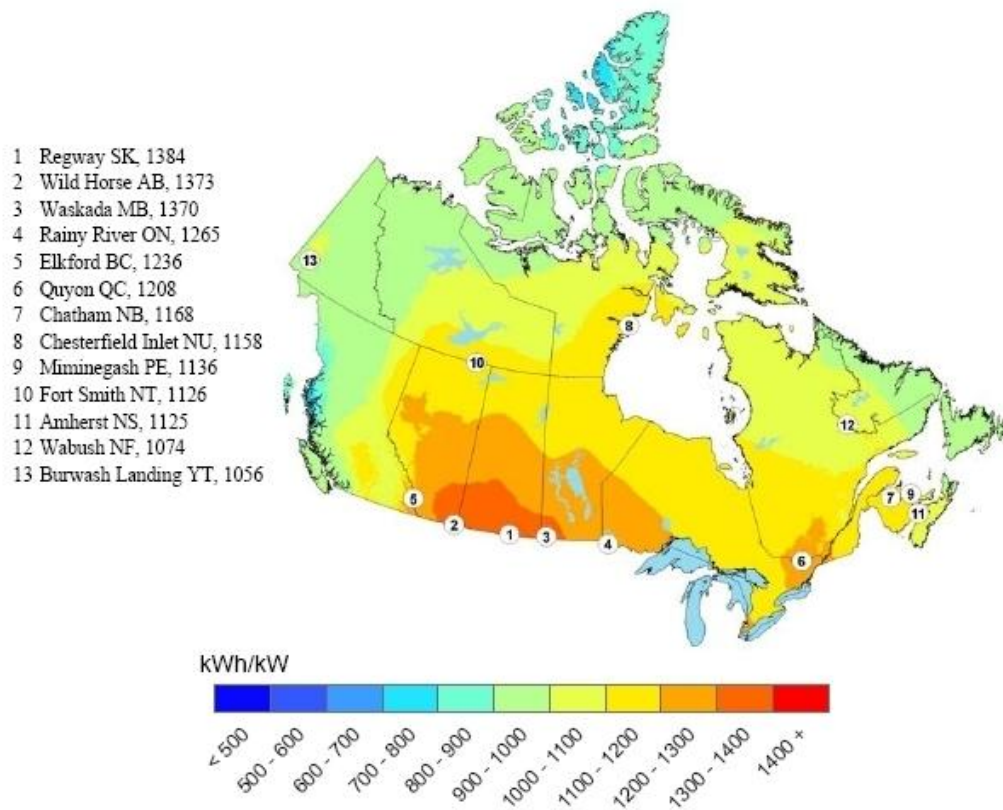


Figure 2.15: Yearly PV potential map in Canada.  
 Image from [36].



Capital City	Yearly PV potential (kWh/ kW)
Regina (Saskatchewan)	1361
Calgary (Alberta)	1292
Winnipeg (Manitoba)	1277
Edmonton (Alberta)	1245
Ottawa (Ontario)	1198
Montreal (Quebec)	1185
Toronto (Ontario)	1161
Fredericton (New Brunswick)	1145
Quebec (Quebec)	1134
Charlottetown (Prince Edward Island)	1095
Yellowknife (Northwest Territories)	1094
Victoria (British Columbia)	1091
Halifax (Nova Scotia)	1074
Vancouver (British Columbia)	1009
Whitehorse (Yukon)	960

Table 2.1: Ranking of major Canadian cities in terms of yearly PV potential. Table from [36].

A solar cell, or a photovoltaic is a semiconductor P-N junction diode. In the presence of sunlight, the electrons go to a higher energy state which results in flowing current from the solar cell to the circuit as shown in Fig. 2.16. This current is proportional to the intensity of light that falls on the cell. Fig. 2.17 illustrates a solar cell panel.

A number of solar cells can be connected to each other to form a photovoltaic module and several PV modules can be wired together to form an array as it is shown in Fig. 2.18

Fig. 2.19 shows the equivalent circuit model for a photovoltaic cell. As this figure indicates, the equivalent circuit consists of a current source, a diode, a shunt resistance represented by  $R_{sh}$  and a series resistance represented by  $R_s$ . For an ideal cell,  $R_{sh}$  would be infinite and  $R_s$  would be zero. In this case no voltage would drop across  $R_s$ .

Fig. 2.20 shows the  $P - V$  and  $i - V$  characteristics of a solar cell. As this figure shows, the current and voltage of a solar cell have a nonlinear relationship and at a specific point which is called the Maximum Power Point (MPP) where maximum power can be generated

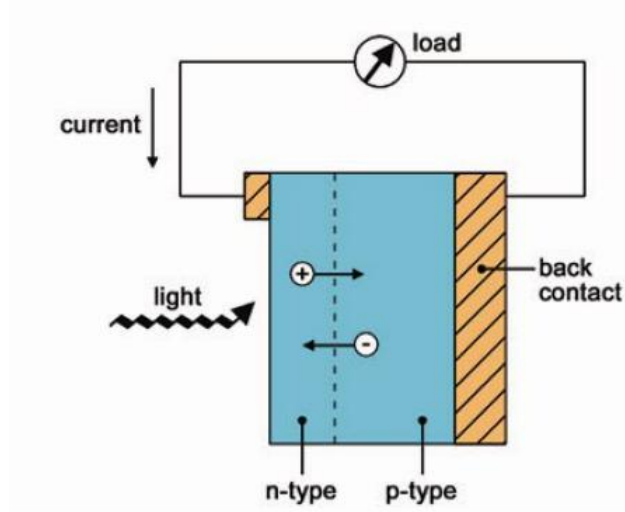


Figure 2.16: Generating electricity using PV.



Figure 2.17: Solar panel.

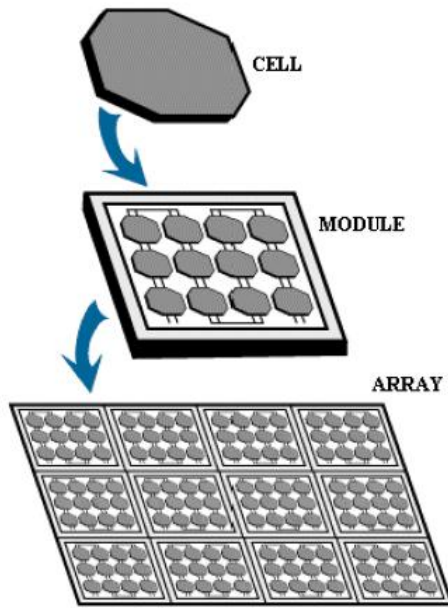


Figure 2.18: Solar cell, solar module, and solar array.

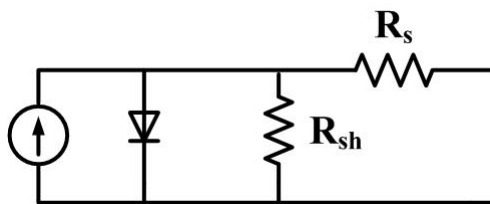


Figure 2.19: Solar cell model.

by the photovoltaic cell. In this figure,  $I_{MPP}$  and  $V_{MPP}$  represent the current and voltage at maximum power point respectively.

The inverse of curve slope of  $i_V$  at  $V_{OC}$  is an approximate value for  $R_s$  and the inverse slope of the  $i_V$  curve at  $I_{SC}$  can be used as an approximate of  $R_{sh}$  as shown in Fig. 2.21.

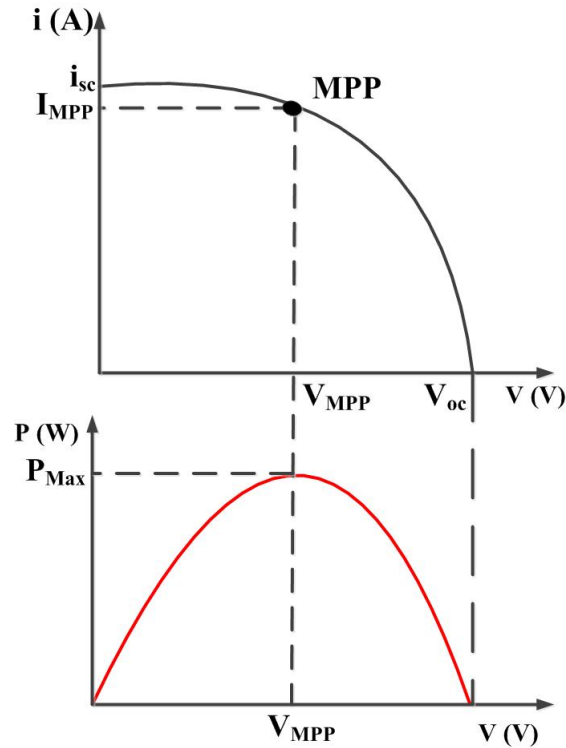


Figure 2.20: Characteristics of a PV array.

In [37], the effect of the temperature and radiation on the PV cell are studied. Fig. 2.22 and Fig. 2.23 show the influence of environmental temperature and radiation on the  $i - V$  curve of a solar cell. As these two figures illustrate, MPP moves by changing the temperature or light radiation on the solar cell.

## 2.2.2 Maximum Power Point Tracking Methods

There are different techniques to adjust the operating point of a solar cell to achieve MPP in which a PV array should operate in order to generate the maximum output power ( $P_{MPP}$ ). Some of the popular schemes are: incremental- conductance technique (ICT) [38]-[42],

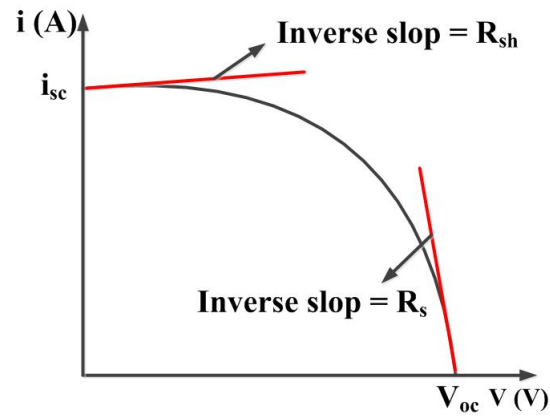


Figure 2.21: slope of i-v curve at  $V_{OC}$  and  $I_{SC}$ .

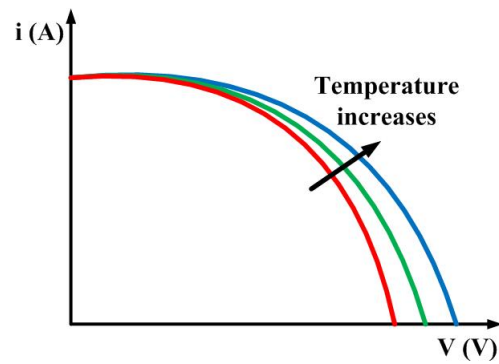


Figure 2.22: The influence of temperature on I-V curve of a solar cell.

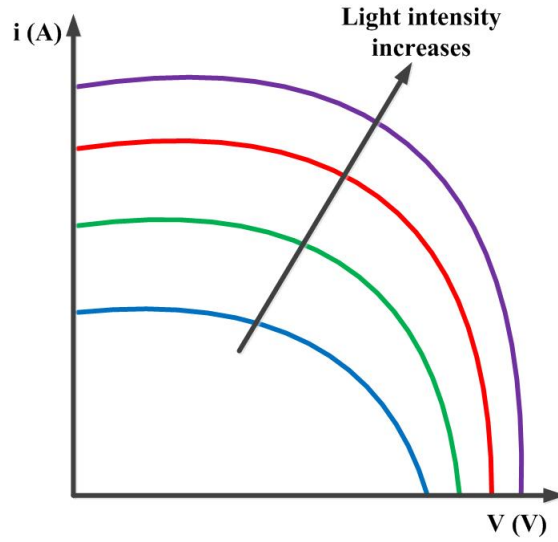


Figure 2.23: The influence of light on I-V curve of a solar cell.

Hill-Climbing / Perturb and Observe methods [43]-[46], fractional open-circuit voltage method [47]-[50], fractional short circuit current method [51]-[53].

### Incremental- Conductance Technique (ICT)

This technique is based on the fact that the slope of the P-V curve of a solar cell is zero at MPP and by adjusting the input resistance of the converter to the optimum impedance of the panel, the panel will work at MPP. The solar cell output power is

$$P = VI \quad (2.1)$$

and partial differential of  $P$  would be

$$\frac{\partial P}{\partial V} = I + V \frac{\partial I}{\partial V} \quad (2.2)$$

As Fig. 2.20 shows, at MPP,  $\frac{\partial P}{\partial V} = 0$ , thus by applying this concept to (3.7), the following equation can be achieved

$$\frac{\partial V}{\partial I} = -\frac{V}{I} \quad (2.3)$$

In this equation  $\frac{\partial V}{\partial I}$  is the impedance of the solar cell which should be equal to the optimum impedance of the solar cell represented by  $R_{MPP}$  to get the maximum power from the cell.

Equation 3.8 reveals that by matching  $\frac{V}{I}$  ( the input impedance of the converter that is connected to the solar cell panel ) to  $R_{MPP}$  the solar cell can generate the maximum output power. Thus if the converter that is connected to the solar cell has resistive input behavior that can be adjusted to  $R_{MPP}$ , the operating point of the solar cell would be MPP which result is getting  $P_{max}$  and also the unity power factor can be achieved.

In this method, two sensors, a voltage sensor and a current sensor are needed to measure the voltage and the current of the solar cell panel. This increases the cost of the system but this technique has high performance and reliability and is suitable for applications such as space satellites.

### **Hill-Climbing / Perturb and Observe**

These two methods perturb the operating point of the PV panel to find the direction in which the power would be at its maximum. From Fig. 2.20, it can be seen that when the solar array operates on the left of MPP, increasing the voltage increases the power, and when operating on the right of MPP, decreasing the voltage increases the power. Therefore, if there is an increase in power, the same path should be followed to reach MPP and the feedback controller forces the derivative of power to be zero.

The methods described above are simple to implement, but similar to the Incremental Conductance technique, these two techniques also need two sensors, one for current and one for voltage. Referring to Fig. 2.24, when the operating point is A and the atmospheric conditions stay approximately constant, the operating point will go to B by a perturbation of  $\Delta V$ . At this time, the perturbation will be reversed because the power is decreased. In this case, if the atmospheric conditions change the i-v curve of the solar panel is shifted to  $P_2$ , hence the operating point will move to C. This shift will increase the power, so the perturbation will result in divergence from the MPP. When atmospheric conditions change rapidly, hill-climbing and perturb and observe methods can fail. In [54], the authors compare the efficiency of the Incremental Conductance method and Perturb and Observe method in the Matlab simulation environment. As shown in Fig. 2.25, the incremental conductance technique reaches the MPP faster than the P&O method. Besides, incremental conductance method does not have continuous oscillation of the operating point around the MPP.

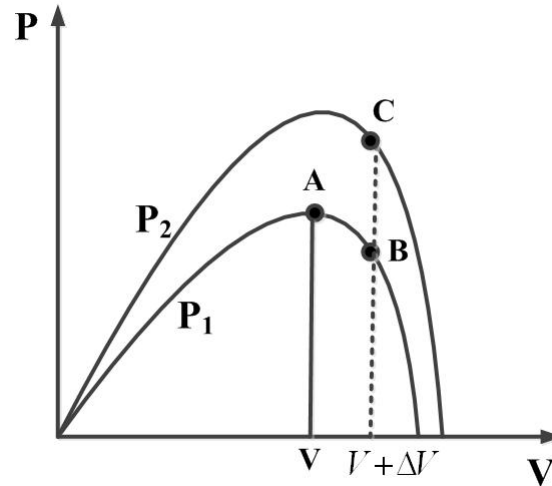


Figure 2.24: The effect of changing atmosphere conditions on tracking MPP of the i-v curve of a solar panel using Hill-Climbing / Perturb and Observe methods .

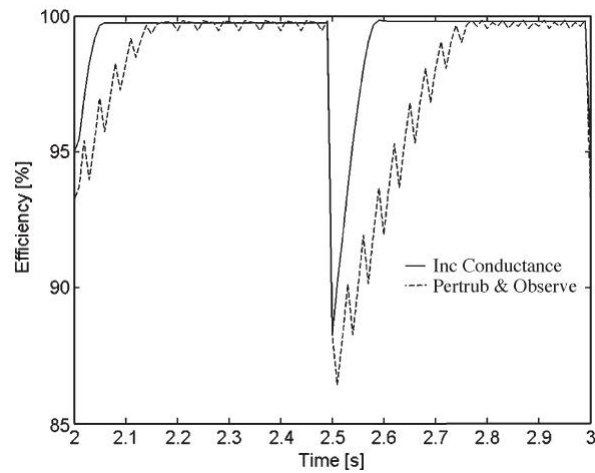


Figure 2.25: Efficiency of MPPT algorithms: incremental conductance technique (ICT) and P&O method.

Image from [54]



### Fractional Open-Circuit Voltage

This method uses the assumption that a near linear relationship between  $V_{MPP}$  and  $V_{OC}$  exists which is given by

$$V_{MPP} \approx k_1 V_{oc} \quad (2.4)$$

In this equation,  $k_1$  is constant depending on the characteristics of the PV array. The term  $k_1$  can be computed and  $V_{oc}$  can be measured by shutting down the power converter for a short time. When  $k_1$  and  $V_{oc}$  are known,  $V_{MPP}$  can be computed using (2.4). One of the disadvantages of this method is the temporary loss of power to measure  $V_{oc}$ .

### Fractional Short-Circuit Current

In this method, the following assumption is used

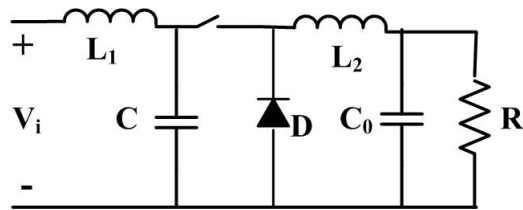
$$I_{MPP} \approx k_2 I_{sc} \quad (2.5)$$

Referring to (2.5), in this method  $I_{MPP}$  and  $I_{sc}$  have a near linear relationship. In this technique, an additional switch should be added to the MPPT circuit to short the PV panel and measure  $I_{sc}$  periodically, which result in increasing the cost and the number of elements in the circuit.

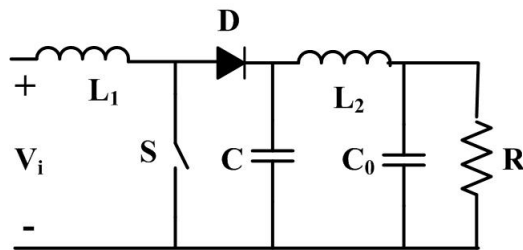
## 2.2.3 Solar cell power converters

Fig. 2.26 shows the commonly used dc/dc converters that are connected to the solar cell panel [55]. These converters operate both in the Continuous-Conduction-Mode (CCM) or Discontinuous-Conduction-Mode (DCM). By using MPPT methods the equivalent input resistance of the converter can be adjusted to the optimum resistance of the PV array at MPP ( $R_{MPP}$ ) [55]. This can be done by tuning the duty cycle of the dc/dc converter. Using this method the operating point of the PV array would be the desired MPP at which point the solar panel can generate maximum power.

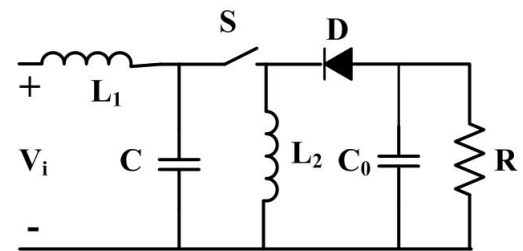
In [56], it is shown that among all these converters, buck-boost converter has the highest efficiency and can track the MPP regardless of the cell temperature, the load, and the irradiation that the cell receives. Moreover, it is shown that the results obtained using the buck-boost converter are not dependent on the MPP tracking method.



(a)



(b)



(c)

Figure 2.26: Commonly used DC to DC converter: (a) buck converter, (b) boost converter, (c) buck-boost converter

## 2.2.4 Solar Power Applications

Solar power is probably one of the cleanest renewable source of energy that is available and can be used in several forms. This source of power can have promising solutions to the world's energy. PV systems can have industrial/commercial and residential applications.

### Residential Applications

As Fig. 2.27 shows, the solar panels can be located on the roofs of houses and buildings to harvest solar power. In this case, the PV system supplies electricity to the house/ building. The solar systems is also connected to the electrical grid. Thus at any time during the day that the PV system generates power more than the required power for the building or during the low/no consumption periods, the excess power can be exported to the grid.



Figure 2.27: Installing solar panels on the roof of a house.

### Industrial and commercial applications

One of the main applications of using PV technology is lighting. Currently PV systems are used to provide lighting in public streets as it is shown in Fig. 2.28, traffic lights, and billboards. Another application of this technology is water pumping. PV cells can power water pumping for irrigation, as it is shown in Fig. 2.29.



Figure 2.28: Solar powered street light.

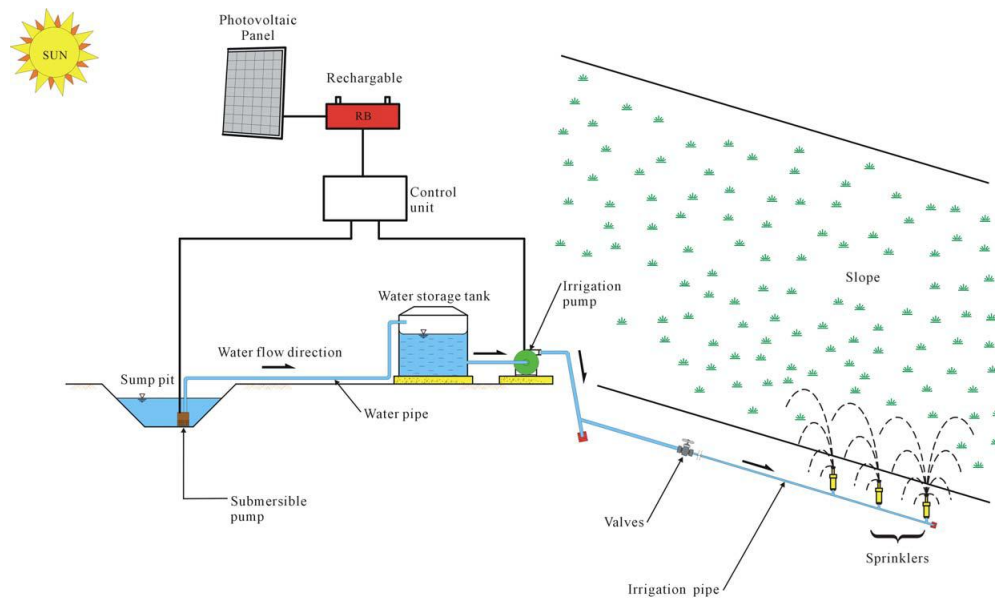


Figure 2.29: Solar Power Automatic Irrigation System.  
Image from [57].

**Solar power advantages and disadvantages**

One of the disadvantages of solar power is that it can only be harvested during the day, thus a back-up system is necessary when the system is not connected to the grid to provide power during the time that the solar power is not available, like during the night or when the weather is cloudy. For indoor locations where the lighting is not sufficient, the efficiency of the harvested power is very low. Given the above disadvantage, the strong advantage of solar power is that it is pollution-free and is highly scalable to match electrical demand.

## Chapter 3

# Theoretical Analysis of the Proposed Circuit

### 3.1 Introduction

In this chapter, the proposed power electronics circuit for energy harvesting applications will be introduced and analyzed. Section 2.2 presents the theoretical modeling and analysis of the circuit. Section 2.3 discusses the design of a feedback controller to adjust the magnitude of the input resistance of the proposed circuit based on the model derived in section 2.2. Section 2.4 presents two different designs for a MOSFET gate drive circuit. The efficiency of the proposed converter is considered in Section 2.5. Section 2.6 discusses the applications of the proposed power electronics circuit in the energy harvesting area.

### 3.2 Theoretical Analysis

Fig. (3.1) shows the proposed power electronics circuitry for energy harvesting applications such as vibrational energy harvesting using piezoelectric transducers and harvesting solar power using solar cells. As this figure shows, this circuit consists of a capacitor, a diode bridge, a MOSFET, and a rechargeable battery as the storage element. The current generated by energy harvester is represented by  $i_{in}$ , this current is the input current to the circuit

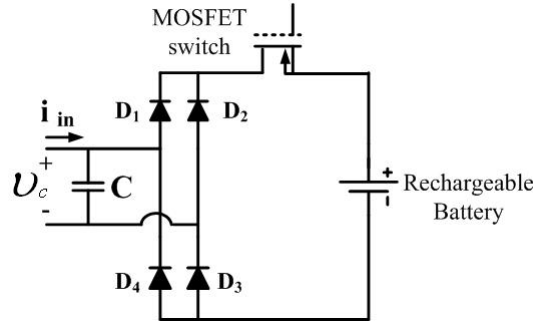


Figure 3.1: Power electronics circuit.

and is time varying . As Fig. (3.1) shows, in this project a rechargeable battery is used as the storage element. A diode bridge, which is an AC to DC rectifier, is used to rectify the voltage across the capacitor. When  $v_C$  is positive,  $D_1$  and  $D_3$  are on and when  $v_C$  is negative  $D_2$  and  $D_4$  are on. The average output voltage across the electrochemical batteries is low, in the range of 1 – 4V, however the magnitude of the generated voltage across the capacitor, represented by  $v_C$ , is relatively high. Therefore after rectifying  $v_C$ , the next step is to step down the input voltage to the level of battery. This is done by using a MOSFET switch, as shown in Fig. 3.1.

To provide an accurate model of the circuit, the internal resistance of the battery and the switching losses are included in the circuit, as shown in Fig. (3.2). In this figure  $r_b$  represents the internal resistance of the battery and  $r_{ds}$  indicates the on resistance of the MOSFET switch when it is on. The forward voltage of each diode is  $V_D$ .

Fig. 3.3 shows the voltage behavior of the rechargeable battery that was used in this project at different rates of discharge. In this figure,  $C$  is the capacity (mAh) of the battery. This battery has a nominal voltage of 1.2V. As the figure shows, the voltage across the battery does not drop below 1V. Thus we can use the assumption that the voltage across the battery is constant, represented by  $V_B$ .

By replacing  $R$  with  $r_b + r_{ds}$ , Fig. (3.2) can be simplified to Fig. (3.4). Fig. 3.5 illustrates the simplified circuit when the MOSFET is on and the magnitude of the input voltage is large enough to turn the diodes ON. Fig. (3.5a) shows the simplified circuit when  $v_C$  is positive, which means that  $D_1$  and  $D_3$  are ON. Fig. (3.5b) illustrates the equivalent circuit when  $v_C$  is negative, in which case  $D_2$  and  $D_4$  are ON.

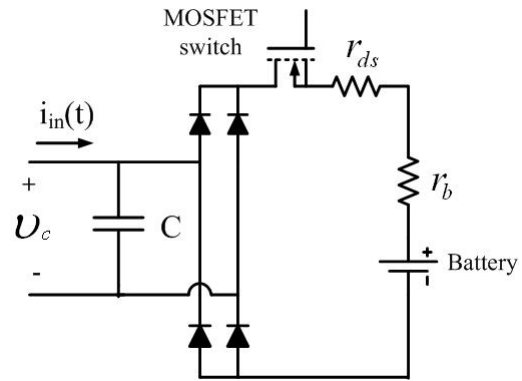


Figure 3.2: Power electronics circuit.

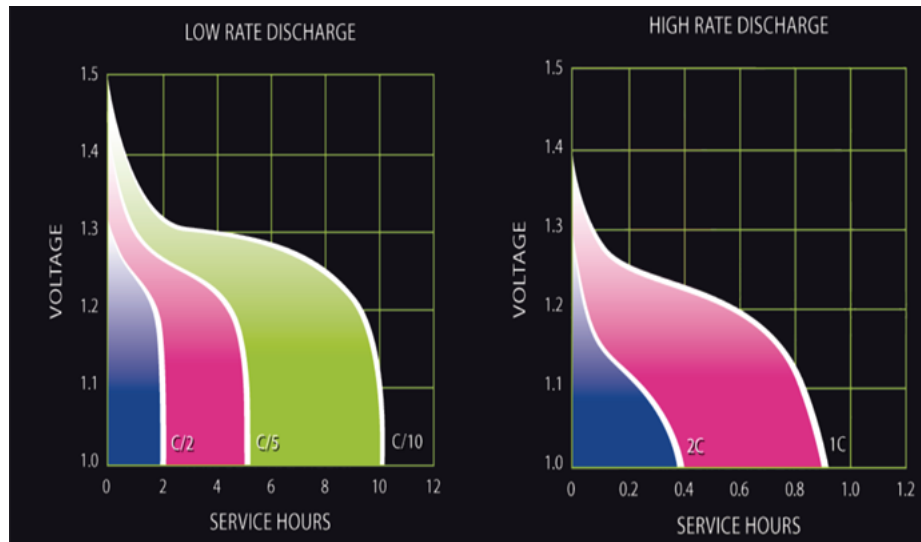


Figure 3.3: Voltage behavior of the rechargeable battery.  
Image from [62].



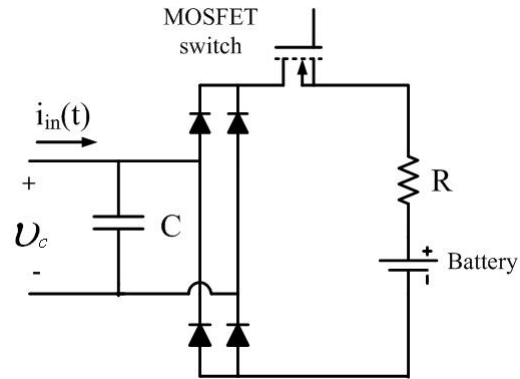


Figure 3.4: Power electronics circuit.

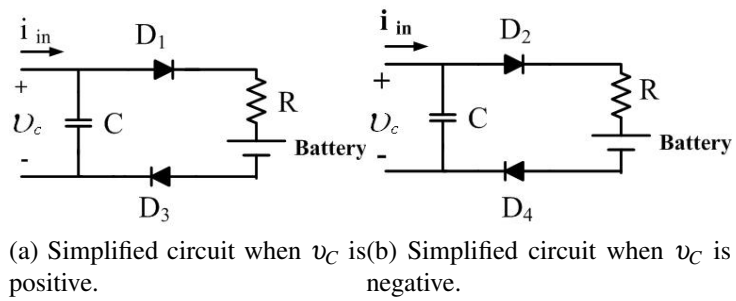


Figure 3.5: Simplified power electronics circuit when MOSFET is on.

The main operation of the circuit can be divided into three phases. In the first phase,  $v_C$  is not large enough to turn on the diode bridge, thus no current flows into the battery and the circuit input current, which is represented by  $i_{in}$ , charges  $C$ . In the second phase which the magnitude of  $v_C$  is large enough to turn on the diode bridge but the MOSFET is off is similar to the first phase. In this case, no current flows into the battery and  $i_{in}$  charges the capacitor. During the third phase, the MOSFET is on and the voltage across the capacitor is greater than the forward voltage of diodes in the diode bridge plus the voltage of battery. Therefore the diode bridge conducts and  $C$  discharges into the battery. The current that comes from the source flows into the battery during this time. The voltage across the capacitor during the second and third phases is shown in Fig. (3.6) and Fig. (3.7), respectively. In these two figures,  $t_1$  refers to the time that the MOSFET is off (second phase) and  $t_2$  refers to the time that the MOSFET is on (third phase). In Fig. (3.6), the voltage across the capacitor is shown when  $i_{in}$  is positive and Fig. (3.7) illustrates the voltage across the capacitor when  $i_{in}$  is negative.

In Fig. (3.6)

$$V_1 = V_B + 2V_D + Ri_{in}((k-1)T_{sw}). \quad (3.1)$$

$$V_2 = V_B + 2V_D + Ri_{in}(kT_{sw}). \quad (3.2)$$

$$V_3 = V_B + 2V_D + Ri_{in}(kT_{sw}) + \frac{1}{C}i_{in}(kT_{sw}t_1). \quad (3.3)$$

In Fig. 3.7

$$V_1 = -V_B - 2V_D + Ri_{in}((k-1)T_{sw}). \quad (3.4)$$

$$V_2 = -V_B - 2V_D + Ri_{in}(kT_{sw}). \quad (3.5)$$

$$V_3 = V_B + 2V_D + Ri_{in}(kT_{sw}) + \frac{1}{C}i_{in}(kT_{sw}t_1). \quad (3.6)$$

In the equations above,  $k$  represents the switching step.

As Fig. (3.6) and Fig. (3.7) illustrate, when the MOSFET is off during  $t_1$ , the magnitude of  $v_C$  increases because the  $i_{in}$  charges the capacitor. However during the on interval of the MOSFET, which is represented by  $t_2$ , the magnitude of  $v_C$  decreases as a result of discharging the capacitor into the battery.

The next step is to calculate the average of  $v_C$  in one period of MOSFET switching.

When the MOSFET switch is off, no current flows into the battery and capacitor charges

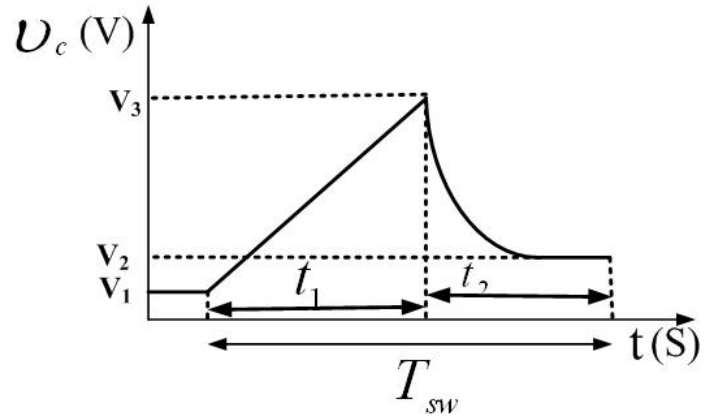


Figure 3.6: The waveform of capacitor voltage in one period of MOSFET switching, during second and third phases, while  $i_{in}(t) > 0$ .

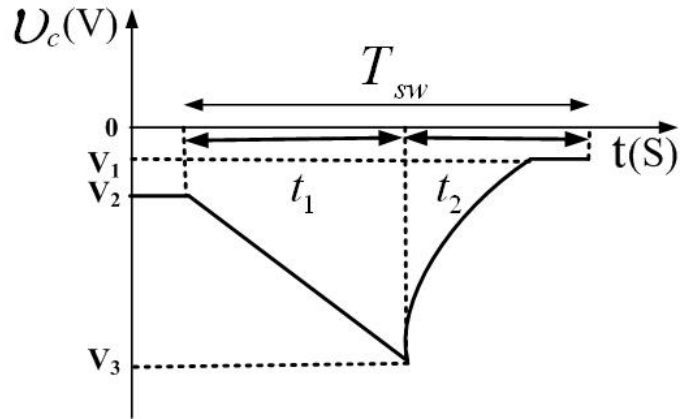


Figure 3.7: The waveform of capacitor voltage in one period of switching, during second and third phases, while  $i_{in}(t) < 0$ .

by  $i_{in}(t)$  that flows into the circuit. The capacitor voltage during the off interval of the MOSFET is given by

$$v_C(t) = \frac{1}{C} \int_{kT_{Sw}}^{kT_{Sw}+t} i_{in}(t) dt + v_C(kT_{Sw}) \quad kT_{Sw} < t < kT_{Sw} + t_1 \quad (3.7)$$

In this equation,  $v_C(kT_{Sw})$  is the initial voltage of capacitor in each period of MOSFET switching. This value is given by

$$v_C(kT_{Sw}) = \begin{cases} V_B + 2V_D + Ri_{in}((k-1)T_{Sw}). & i_{in}(t) \geq 0 \\ -V_B - 2V_D + Ri_{in}((k-1)T_{Sw}). & i_{in}(t) < 0 \end{cases} \quad (3.8)$$

By substituting  $V_{DC}$  with  $V_B + 2V_D$ , (3.8) can be written as

$$v_C(kT_{Sw}) = \begin{cases} V_{DC} + Ri_{in}((k-1)T_{Sw}). & i_{in}(t) \geq 0 \\ -V_{DC} + Ri_{in}((k-1)T_{Sw}). & i_{in}(t) < 0 \end{cases} \quad (3.9)$$

The switching frequency is higher than the frequency of  $i_{in}(t)$ , thus we can use the assumption that  $i_{in}(t)$  is approximately constant during one period of MOSFET switching. The integral in (3.7) can be simplified to

$$\int_{kT_{Sw}}^{kT_{Sw}+t} i_{in}(t) dt = i_{in}(kT_{Sw})t \quad (3.10)$$

By replacing  $v_C(kT_{Sw})$  with (3.9), and using the assumption that the input current to the circuit  $i_{in}(t)$  is constant in one period of MOSFET switching, (3.7) can be written as

$$v_C(t) = \begin{cases} V_{DC} + Ri_{in}((k-1)T_{Sw}) + \frac{1}{C}i_{in}(kT_{Sw})t. & i_{in}(t) \geq 0 \\ -V_{DC} + Ri_{in}((k-1)T_{Sw}) + \frac{1}{C}i_{in}(kT_{Sw})t. & i_{in}(t) < 0 \end{cases} \quad (3.11)$$

As Fig. 3.6 illustrates, at  $t = t_1$  the MOSFET turns on. By replacing  $t_1$  with  $t$  in (3.11), we can obtain the voltage across the capacitor at  $t = t_1$ , which is given by

$$v_C(kT_{Sw} + t_1) = \begin{cases} V_{DC} + Ri_{in}((k-1)T_{Sw}) + \frac{1}{C}i(kT_{Sw})t_1. & i_P(t) \geq 0 \\ -V_{DC} + Ri_{in}((k-1)T_{Sw}) + \frac{1}{C}i(kT_{Sw})t_1. & i_P(t) < 0 \end{cases} \quad (3.12)$$

The MOSFET turns on at  $t = t_2$ . If the magnitude of  $v_C$  is greater than  $V_{DC}$ , the capacitor can turn on the diode bridge. At this point, the capacitor discharges into the battery which results in the decrease of  $v_C$  during  $t_2$ . Also,  $v_C$  during the on time of the MOSFET is given by

$$v_C(t) = \begin{cases} V_{DC} + Ri_{in}(kT_{Sw}) + (v_C(kT_{Sw} + t_1) - V_{DC} - Ri_{in}(kT_{Sw}))e^{\frac{-t}{RC}} & i_{in}(t) \geq 0 \\ -V_{DC} + Ri_{in}(kT_{Sw})(v_C(kT_{Sw} + t_1) + V_{DC} - Ri_{in}(kT_{Sw}))e^{\frac{-t}{RC}} & i_{in}(t) < 0 \end{cases} \quad (3.13)$$

Substituting  $v_C(kT_{Sw} + t_1)$  from (3.12) into (3.13) yields

$$v_C(t) = \begin{cases} V_{DC} + Ri_{in}(kT_{Sw}) + \\ [\frac{1}{C}i_{in}(kT_{Sw})t_1 + R(i_{in}(kT_{Sw}) - i_{in}((k-1)T_{Sw}))]e^{\frac{-t}{RC}} & i_{in}(t) \geq 0 \\ -V_{DC} + Ri_{in}(kT_{Sw}) + \\ [\frac{1}{C}i(kT_{Sw})t_1 + R(i_{in}(kT_{Sw}) - i_{in}((k-1)T_{Sw}))]e^{\frac{-t}{RC}} & i_{in}(t) < 0 \end{cases} \quad (3.14)$$

It should be noted that  $i_{in}$  comes from a harvestable source of energy and is very small. Also  $R$ , which is the summation of the internal resistance of the battery and the on resistance of the MOSFET is relatively small, in the range of  $0.5 - 2\Omega$ . Therefore, we can assume  $|V_{DC}| \gg Ri_{in}((k-1)T_{Sw})$ . By using this assumption, Fig. (3.6) and Fig. (3.7) can be simplified to Fig. (3.8) and Fig. (3.9) respectively. Moreover (3.11) can be further simplified to

$$v_C(t) = \begin{cases} V_{DC} + \frac{1}{C}i_{in}(kT_{Sw})t. & i_{in}(t) \geq 0 \\ -V_{DC} + \frac{1}{C}i_{in}(kT_{Sw})t. & i_{in}(t) < 0 \end{cases} \quad (3.15)$$

and (3.14) can be simplified to

$$v_C(t) = \begin{cases} V_{DC} + \frac{1}{C} i_{in}(kT_{Sw}) t_1 e^{-\frac{t}{RC}} & i_{in}(t) \geq 0 \\ -V_{DC} + \frac{1}{C} i_{in}(kT_{Sw}) t_1 e^{-\frac{t}{RC}} & i_{in}(t) < 0 \end{cases} \quad (3.16)$$

$v_C$  contains high frequency components due to the switching of the MOSFET switch, while

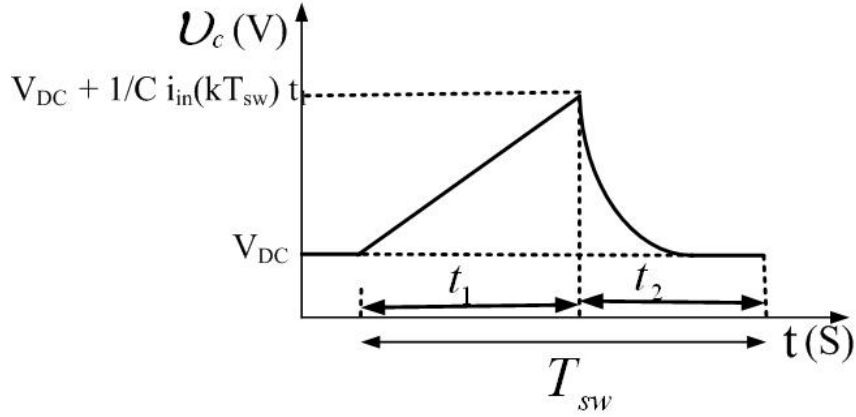


Figure 3.8: The simplified waveform of  $v_C$  in one period of MOSFET switching, during second and third phases, while  $i_{in}(t) > 0$ .

the frequency of  $i_{in}(t)$  is assumed to be much lower than the PWM frequency. Using the area of triangle in Fig. 3.8, when the current source  $i_{in}(t)$  is positive, and Fig. (3.9) when  $i_{in}(t)$  is negative, the average voltage across the capacitor during one period of the PWM signal, represented by  $\overline{v_C(t)}$ , is given by

$$\overline{v_C(t)} = \begin{cases} V_{DC} + \frac{t_1^2}{2CT_{Sw}} i_{in}(kT_{Sw}) + \\ \frac{1}{T} \frac{t_1}{C} i_{in}(kT_{Sw}) \int_0^{T_{Sw}-t_1} e^{-\frac{t}{RC}} dt & i_{in}(t) \geq 0 \\ -V_{DC} + \frac{t_1^2}{2CT_{Sw}} i_{in}(kT_{Sw}) + \\ \frac{1}{T_{Sw}} \frac{t_1}{C} i_{in}(kT_{Sw}) \int_0^{T-t_1} e^{-\frac{t}{RC}} dt & i_{in}(t) < 0 \end{cases} \quad (3.17)$$

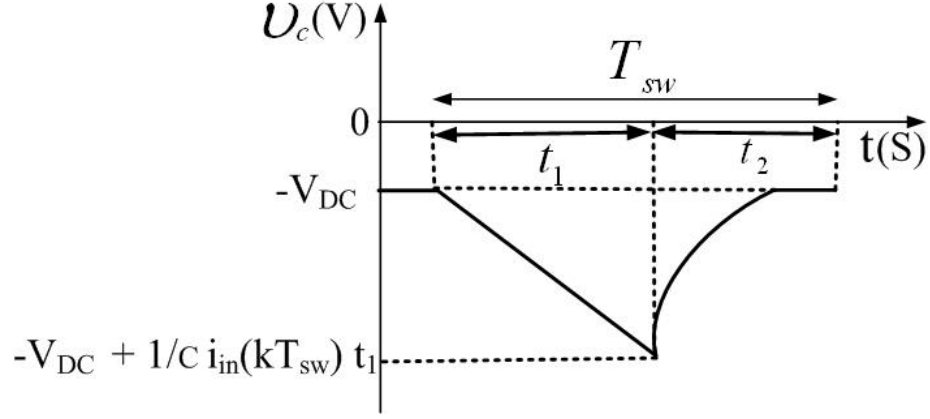


Figure 3.9: The simplified waveform of  $v_c$  in one period of switching during second and third phase, while  $i_{in}(t) < 0$ .

Solving the integrals in this equation results in

$$\overline{v_c(t)} = \begin{cases} V_{DC} + \frac{t_1^2}{2CT_{sw}} i_{in}(kT_{sw}) + \\ \frac{Rt_1}{T_{sw}} (1 - e^{-\frac{(T_{sw}-t_1)}{RC}}) i_{in}(kT_{sw}). & i_{in}(t) \geq 0 \\ -V_{DC} + \frac{t_1^2}{2CT_{sw}} i_{in}(kT_{sw}) + \\ \frac{Rt_1}{T_{sw}} (1 - e^{-\frac{(T_{sw}-t_1)}{RC}}) i_{in}(kT_{sw}). & i_{in}(t) < 0 \end{cases} \quad (3.18)$$

Thus (3.18) can be written as

$$\overline{v_c(t)} = \begin{cases} V_{DC} + R_{eq} i_{in}(kT_{sw}). & i_{in}(t) \geq 0 \\ -V_{DC} + R_{eq} i_{in}(kT_{sw}). & i_{in}(t) < 0 \end{cases} \quad (3.19)$$

with  $R_{eq}$  given by

$$R_{eq} = \frac{t_1^2}{2CT_{sw}} + R \frac{t_1}{T_{sw}} (1 - e^{-\frac{(T_{sw}-t_1)}{RC}}). \quad (3.20)$$

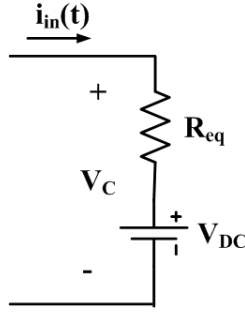


Figure 3.10: Equivalent power electronics circuit.

Fig. 3.10 illustrates the equivalent energy harvesting circuit described by (3.19). (3.19) indicates that,  $\overline{v_C(t)}$  and  $i_{in}(t)$  have a resistive relationship and the proposed power electronics circuit exhibits a purely resistive input behavior. This equation also reveals that this resistive behavior between the input voltage and current of the circuit works for any given frequency. More details about applications of this concept are discussed in Section VI. Furthermore, this resistive behavior can be used to maximize the power that can be transferred from the source to the circuit.

The duty cycle, represented by  $d$ , is the ratio of the duration that the MOSFET is on to the total period of MOSFET switching.  $t_2$  is the time that MOSFET is on and  $T_{Sw}$  is the total period of switching. Thus the duty cycle of the MOSFET is given by

$$d = \frac{t_2}{T_{Sw}} \quad (3.21)$$

Replacing  $t_2$  with  $T_{Sw} - t_1$ , (3.21) can be further written as

$$d = \frac{T_{Sw} - t_1}{T_{Sw}} \quad (3.22)$$

From (3.22),  $t_1$  can be calculated as

$$t_1 = (1 - d)T_{Sw} \quad (3.23)$$

Substituting  $t_1$  from (3.23) into (3.20),  $R_{eq}$  can be further written as



$$R_{eq} = \frac{(1-d)^2 T_{Sw}}{2C} + R(1-d) \left(1 - e^{-\frac{T_{Sw}d}{RC}}\right). \quad (3.24)$$

As mentioned earlier,  $R$  is the summation of the internal resistance of the battery and the on resistance of the switching MOSFET and is very small. Furthermore,  $C$  which is the input capacitor of the circuit is small as well. Thus we can make the assumption that  $T_{Sw}D \gg RC$  and  $1 \gg e^{-\frac{T_{Sw}D}{RC}}$ . Therefore, (3.24) can be further simplified to

$$R_{eq} = \frac{(1-d)^2 T_{Sw}}{2C} + R(1-d). \quad (3.25)$$

This equation indicates that the input resistance of the circuit is a factor of the switching frequency and the switching duty cycle, as well as  $C$ . Therefore, by changing these three factors, we can change the value of  $R_{eq}$  and adjust it to a desired value.

Referring to Fig. 3.10, KVL can be applied to the equivalent circuit, which results in

$$\overline{v_C(t)} = \begin{cases} V_{DC} + R_{eq}i_{in}(kT_{Sw}) & i_{in}(t) \geq 0 \\ -V_{DC} + R_{eq}i_{in}(kT_{Sw}) & i_{in} < 0 \end{cases} \quad (3.26)$$

Using this equation,  $R_{eq}$  can be obtained as follows

$$R_{eq} = \begin{cases} \frac{\overline{v_C(t)} - V_{DC}}{i_{in}(kT_{Sw})} & i_{in}(t) \geq 0 \\ \frac{\overline{v_C(t)} + V_{DC}}{i_{in}(kT_{Sw})} & i_{in} < 0 \end{cases} \quad (3.27)$$

Equation (3.27) can be used to express  $R_{eq}$  in simulation environment and experiment.

### 3.3 Design of the Controller to Control the Input Resistance of the Converter

In this section, a Proportional Integral (PI) controller is designed to control the input resistance of the circuit,  $R_{eq}$ . From (3.25), it follows that the input resistance of the circuit,

$R_{eq}$ , is a function of the frequency and duty cycle of the PWM signal. Therefore  $R_{eq}$  can be varied by changing the duty cycle of the MOSFET switch. To achieve a desired resistance, we develop a feedback controller such that the error between  $R_{eq}$  and a desired resistor  $R_P$  approaches zero. To obtain the control scheme, let us assume that the desired resistance has been reached, e.g.,

$$R_{eq} = R_P. \quad (3.28)$$

In this work, it is assumed that the duty cycle of the PWM signal that is applied to the MOSFET switch consists of a nominal value represented by  $d_n$  in addition to a value provided by the controller, represented by  $\Delta d$  as follows

$$d = d_n + \Delta d. \quad (3.29)$$

In this work, a PI controller (Proportional Integral Controller) is used to change the value of  $R_{eq}$  to achieve a desired value. Fig. 3.11 shows the block diagram of a PI controller, that consists of a proportional gain represented by  $K_P$  and an integral gain represented by  $K_I$ . As this figure indicates, the controller output is  $\Delta d$ . Referring to (3.29), this duty cycle is added to  $d_n$  and the result of this summation is the total duty cycle of the PWM signal that is applied to the MOSFET.

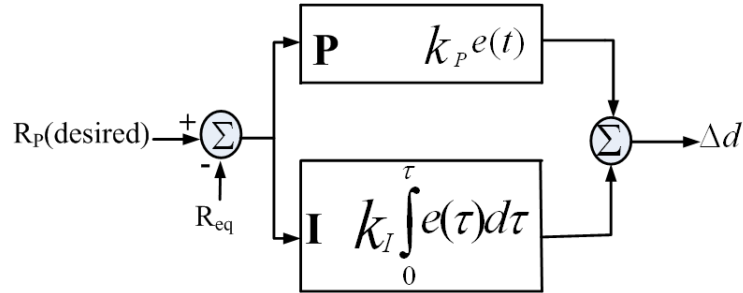


Figure 3.11: Block diagram of a PI controller.

By substitute  $d$  with  $d_n + \Delta d$ ,  $R_{eq}$  can be written as

$$R_{eq} = \frac{(1 - d_n - \Delta d)^2 T_{Sw}}{2C} + R(1 - d_n - \Delta d). \quad (3.30)$$

The controller error is given by

$$e = R_P - R_{eq}. \quad (3.31)$$

Using (3.30), (3.31) can be written as

$$e = R_P - \left[ \frac{(1 - d_n - \Delta d)^2 T_{Sw}}{2C} + R(1 - d_n - \Delta d) \right]. \quad (3.32)$$

In (3.32), if  $d_n$  is chosen as the duty cycle to achieve impedance matching between  $R_P$  and  $R_{eq}$ ,  $\frac{(1 - d_n)^2 T_{Sw}}{2C} + R(1 - d_n)$  must be equal to  $R_P$ . Thus the controller error,  $e$  would be given by

$$e = \left[ \frac{(1 - d_n) \Delta d T_{Sw}}{C} + R \Delta d \right]. \quad (3.33)$$

Equation. 3.33 can be rearranged to

$$e = \left( \frac{(1 - d_n) T_{Sw}}{C} + R \right) \Delta d. \quad (3.34)$$

Let us define

$$K_C = \left( \frac{(1 - d_n) T_{Sw}}{C} + R \right). \quad (3.35)$$

which by substituting into (3.34) yields

$$e = K_C \Delta d. \quad (3.36)$$

where  $\Delta d$  is the output of the PI controller. Thus choosing

$$\Delta d = K_I \int e dt + K_P e. \quad (3.37)$$

and substituting  $\Delta d$  from (3.37), the error dynamics can be written as

$$e = K_C (K_I \int e dt + K_P e). \quad (3.38)$$

Equation (3.38) can be further simplified to

$$K_I \int e dt + \left( K_P - \frac{1}{K_C} \right) e = 0. \quad (3.39)$$

Which indicates the exponential convergence of  $e$  to zero when  $K_P - \frac{1}{K_C} > 0$ .

## 3.4 MOSFET Gate Drive Circuits

In this section, two different designs for MOSFET gate drive will be discussed. The first design utilizes positive feedback to speed PWM signal rise and fall times. In the second design, we made the MOSFET gate drive self powered, thus no external power supply is needed to drive the MOSFET.

### 3.4.1 MOSFET Gate Drive Circuit Using Positive Feedback

In this section, the first MOSFET gate drive circuit that was used in this project will be discussed. To turn on the MOSFET, the voltage that is applied to the gate-source must be greater than the threshold voltage of the MOSFET ( $V_{GS} > V_{threshold}$ ). To reduce the rise and fall times of the PWM signal and to have sharp pulses, a positive feedback configuration is used as shown in Fig. 3.12.

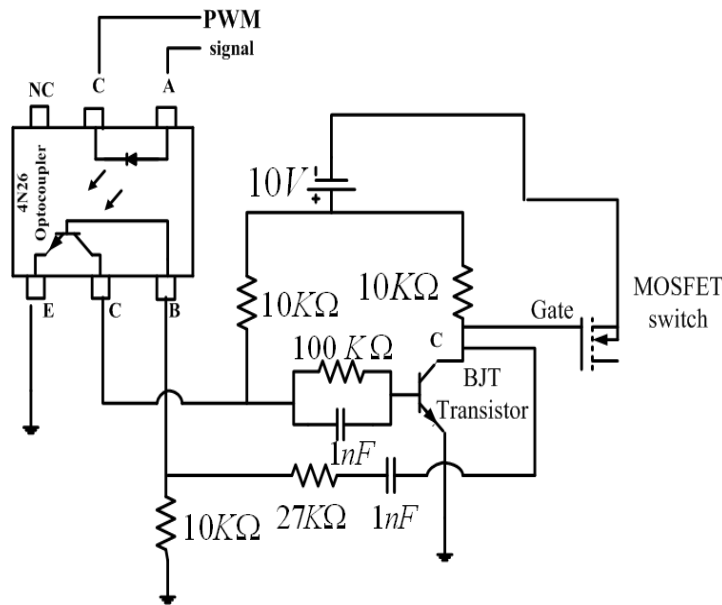


Figure 3.12: Positive feedback for MOSFET Driver.

As this figure shows, this positive feedback contains an optocoupler and a BJT transistor. The combination of these two elements results in reducing the rise and fall times of the PWM pulses. An optocoupler consists of two parts: an optical transmitter and an optical

receiver. The transmitter device is usually an LED (Light-Emitting-Diode) and the receiver device is typically a phototransistor, as it is shown in Fig. 3.13.

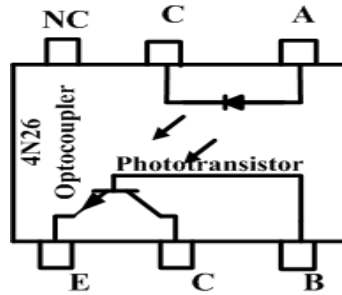


Figure 3.13: Optocoupler

By applying voltage to the optocoupler input, the LED is forward biased and the electrons are able to recombine with electron holes within the device, this results in releasing energy in the form of photons. These photons strike the base junction of the transistor and form the collector current.

Phototransistors can be used in two modes: active mode and switch mode. Operating in active mode means that the phototransistor responds proportionally to the light that is being received up to a certain level. When the amount of light surpasses that level, the phototransistor becomes saturated and the output will not increase even as the light level increases. Working in the switch mode means that the phototransistor will either be "off" or "on" in response to light. In our application, we need to generate a PWM signal which has two levels of on and off. Thus the optocoupler is used in the switch mode.

Referring to Fig. (3.12), the source terminal of the MOSFET switch is connected to the negative terminal of the DC power supply and the gate of the MOSFET is attached to the transistor's collector. More details about the operation of this circuit are provided in the following section.

When a PWM signal is applied to the optocoupler, the LED can turn on the phototransistor. The current flows from the collector to the emitter and the collector of the phototransistor will have the same voltage as its emitter (0V). Referring to Fig. (3.12), the collector terminal of the phototransistor is connected to the base terminal of the BJT. Therefore, the voltage across the base terminal will be 0V, which results in turning off the BJT. In this

case, the voltage of the collector of BJT that is connected to the positive terminal of the DC power supply will be 10V. As Fig. (3.12) shows, the collector of BJT is connected to the base of the phototransistor. This connection results in a faster turn on the phototransistor and a reduction of the rise time of the PWM signal. A similar story happens for the falling time of the MOSFET resulting in accelerating the falling time of the BJT. When PWM signal has a value of 0V, the optocoupler does not conduct and therefore, the voltage across the collector of the phototransistor will be the same as the power supply voltage of 10V. Referring to Fig. (3.12), the collector of the optocoupler is connected to the positive terminal of the DC power supply via a  $10K\Omega$  resistor. When the optocoupler is off, this terminal has the same voltage as the DC power supply (10V). The base of BJT is connected to the optocoupler's collector, so when the collector's voltage is 10V, the BJT conducts and its collector voltage will be 0V. The connection of the optocoupler base and collector of the BJT results in helping the phototransistor turn off faster and reduce the fall time of the PWM signal.

### 3.4.2 Self-Powered MOSFET Gate Drive Circuit

The main application of the proposed circuit in this work is harvesting energy. In most cases, the harvested energy is used to power a sensor. The sensors are usually located in remote locations thus, it would be ideal that the energy harvesting circuit to be self-powered and can work independent of the external power supply. In this section, a new design of the MOSFET gate drive will be introduced. This circuit does not need external power supply which in the sense that the power electronics circuit and MOSFET gate drive to obtain their power from the input source and thus do not need an external power source.

By adding a diode,  $D_S$  and a large capacitor,  $C_S$  to our circuit as shown in Fig. 3.14 we can track and store the peak of  $v_C$  and use this voltage to drive the switching MOSFET. In this design, if  $v_C$  is greater than  $3V_D$ ,  $D_S$  turns on and  $C_S$  charges up to  $|v_C| - 3V_D$ . At this point, the capacitor stores the current peak voltage and  $D_S$  keeps the capacitor from being discharged. This situation continues until the voltage across  $C$  reaches a higher peak. At a higher peak,  $D_S$  turns on and  $C_S$  continues charging up to the new peak. Fig. 3.15 shows the operation of the peak detector. As this figure shows,  $C_S$  keeps track of the highest peak

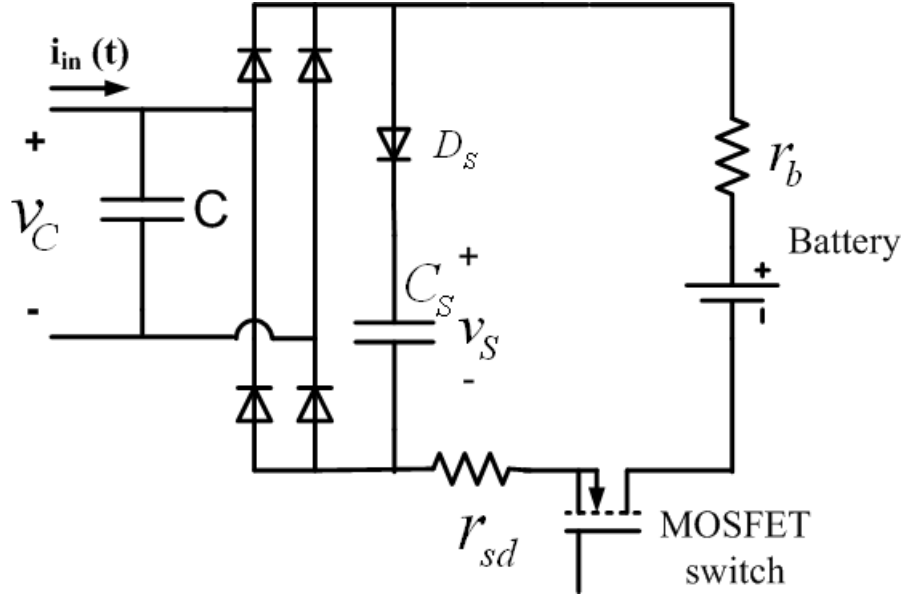


Figure 3.14: Energy harvesting circuit and peak detector

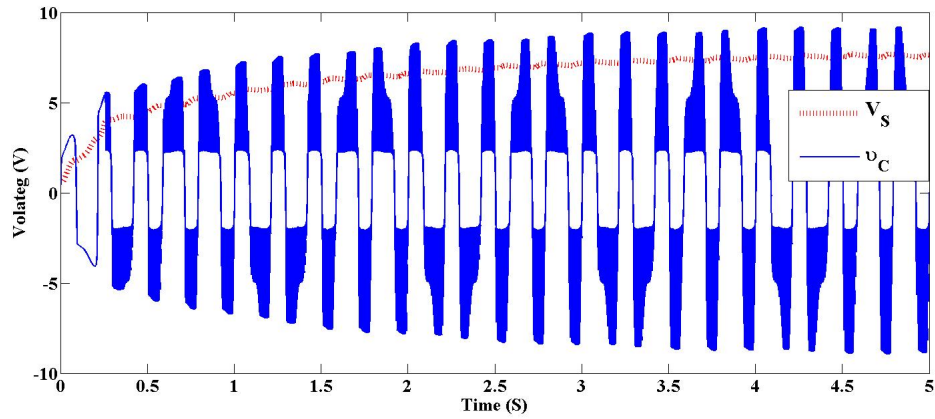


Figure 3.15:  $V_S$  and  $v_C$  in the peak detector

across the capacitor  $C$  which stores this value and charges up again when  $v_C$  reaches a higher peak.

Fig. 3.16 shows the low frequency oscillator circuit that is used to drive the switching MOSFET. As this figure shows, the voltage across the storing capacitor  $C_S$  is used as the power supply for the opamp as well as the non-inverting input terminal of the opamp. Fig. 3.17 illustrates the connection of the low frequency oscillator to the circuit. The main

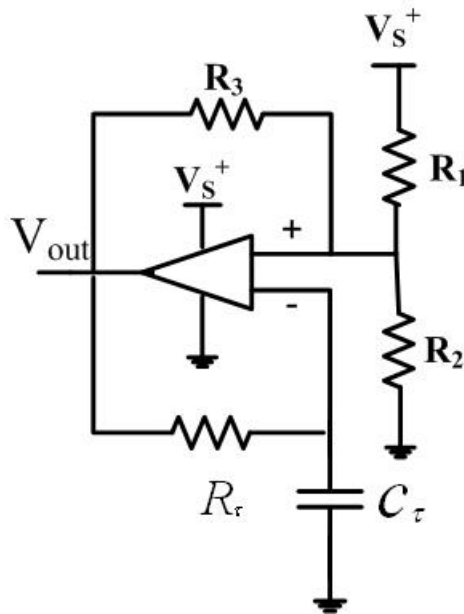


Figure 3.16: Low Frequency Oscillator Circuit.

operation of this LF oscillator is as follows when the voltage at the positive input terminal of the opamp is greater than the voltage at the negative input terminal of the opamp, a positive voltage develops between the reversing and non-reversing input terminals of the opamp. Model of an ideal opamp is shown in Fig. 3.18. This positive voltage between the input terminals is amplified by the open-loop gain of the opamp ( $A_V$ ) which drives the opamp to the positive-saturation mode. In this case, the opamp output equals the voltage that is applied to its positive power supply terminal which is equal to  $V_S$  Fig. (3.16) illustrates.

At this time, the output voltage of the opamp charges  $C_\tau$  until the voltage across  $C_\tau$  goes above the voltage of the non-inverting input terminal of the opamp after which the opamp is driven into the negative saturation mode. In this case, because the output of opamp is less



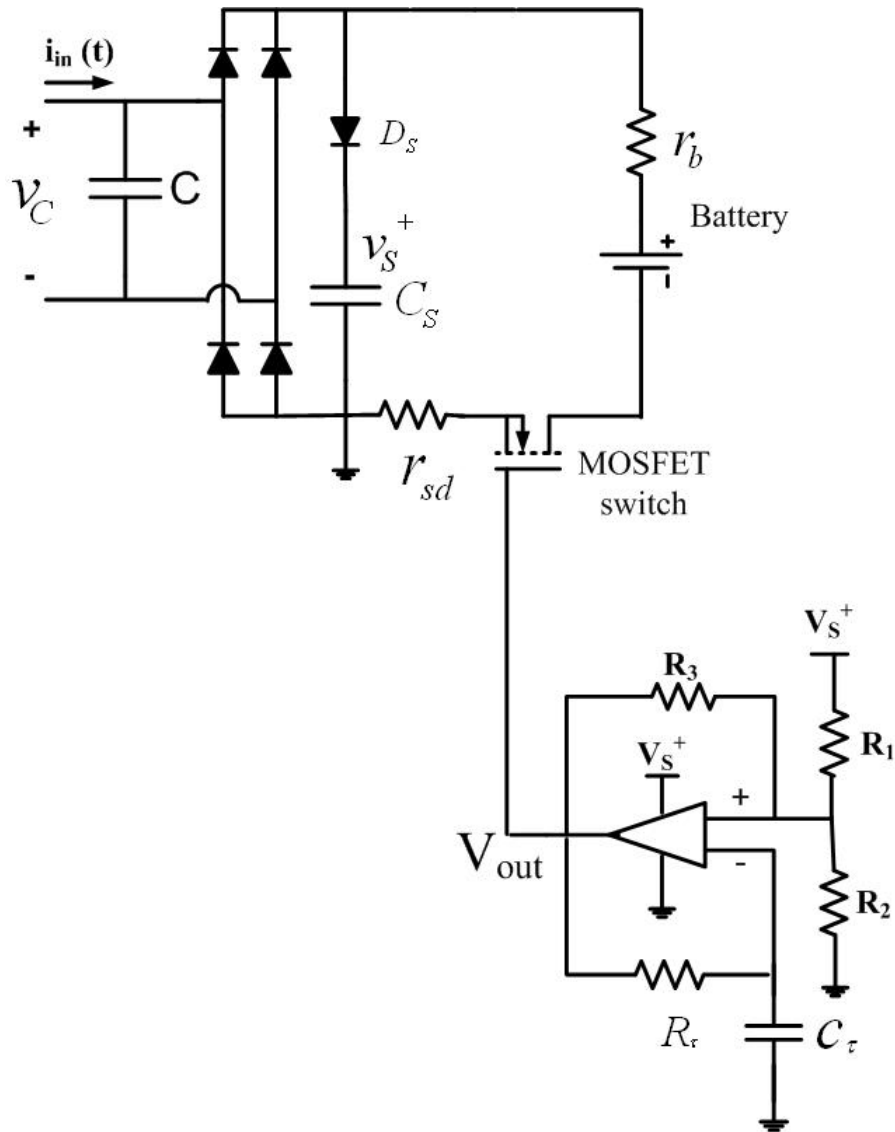


Figure 3.17: Connection of low frequency oscillator to the circuit [?].

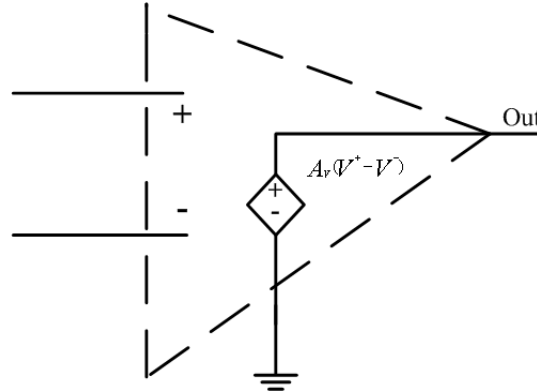


Figure 3.18: Internal circuit of a an ideal opamp.

than the voltage across  $C_\tau$ , the capacitor discharges to  $R_\tau$  until  $V^-$  becomes less than  $V^+$  after which the opamp goes into positive saturation state.

The waveforms of the opamp output and the reverting input terminal of the opamp are shown in Fig. 3.19. In this figure,  $t_1$  refers to the time that opamp is in positive saturation mode of operation,  $t_2$  refers to the time that opamp is in negative mode of operation, and  $T_{sw}$  is the period of the PWM signal that is generated as a result of switching the opamp between these two modes.

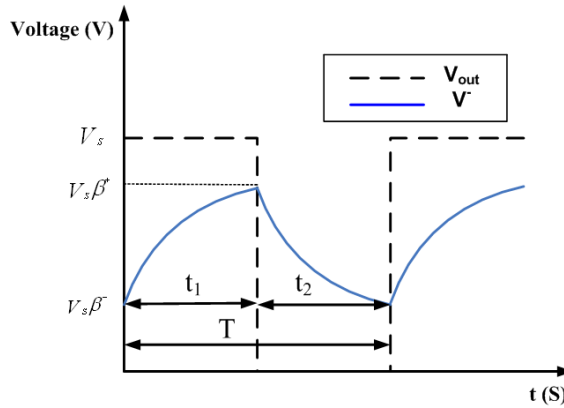


Figure 3.19: Waveforms of the opamp output and op amp inverting input terminal circuit shown on fig. 3.18.

By applying the *Kirchhoff's Current Law* at non-reverting input node of the opamp we have

$$\frac{V_S - V^+}{R_1} = \frac{V^+}{R_2} + \frac{V^+ - V_{out}}{R_3} \tag{3.40}$$

When the opamp goes into the positive saturation state, its output equals the positive power supply of the opamp  $V_S$ . Thus replacing  $V_{out}$  with  $V_S$  in (3.40) results in

$$\frac{V_S - V^+}{R_1} = \frac{V^+}{R_2} + \frac{V^+ - V_S}{R_3} \quad (3.41)$$

and the voltage across the positive input terminal of the opamp would be

$$V^+ = V_S \left( \frac{\frac{1}{R_1} + \frac{1}{R_3}}{\frac{1}{R_1} + \frac{1}{R_2} + \frac{1}{R_3}} \right) \quad (3.42)$$

Now,  $\beta^+$  can be defined as

$$\beta^+ = \frac{\frac{1}{R_1} + \frac{1}{R_3}}{\frac{1}{R_1} + \frac{1}{R_2} + \frac{1}{R_3}} \quad (3.43)$$

The voltage across the non-inverting input terminal of the opamp, while it is in positive saturation mode, can be written as

$$V^+ = V_S \beta^+ \quad (3.44)$$

When the opamp goes into negative saturation, because a negative voltage is generated between the input terminals of the opamp, the opamp output would be equal to the voltage that is applied to the negative power supply of the opamp. Applying *Kirchhoff's Current Law* at non-inverting input node of the opamp results in

$$\frac{V_S - V^+}{R_1} = \frac{V^+}{R_2} + \frac{V^+}{R_3} \quad (3.45)$$

Then the voltage across the positive input terminal of the opamp would be

$$V^+ = V_S \left( \frac{\frac{1}{R_1}}{\frac{1}{R_1} + \frac{1}{R_2} + \frac{1}{R_3}} \right) \quad (3.46)$$

Now, let us define

$$\beta^- = \frac{\frac{1}{R_1}}{\frac{1}{R_1} + \frac{1}{R_2} + \frac{1}{R_3}} \quad (3.47)$$

Thus,  $V^+$  for the negative saturation mode of the apamp can be written as

$$V^+ = V_S \beta^- \quad (3.48)$$

The next step is to calculate the period of the PWM signal generated by the opamp as a result of switching the opamp between the positive and negative saturation modes.

When the opamp is in the positive saturation mode and  $C_\tau$  is charging, the voltage across  $C_\tau$  is given by

$$V_{C_\tau} = V_S - R_\tau i \quad (3.49)$$

By using the current-voltage relation in a capacitor, we can rewrite (3.49) as

$$\int \frac{i(t)}{C_\tau} dt - V_{C_\tau}(0) = V_S - R_\tau i \quad (3.50)$$

and by calculating the derivative of (3.50) we have

$$R_\tau \frac{di}{dt} + \frac{1}{C_\tau} = 0 \quad (3.51)$$

Solving (3.51) for  $i$  results in

$$i = I(0)e^{\left(\frac{-t}{\tau}\right)} \quad (3.52)$$

Hence at  $t = 0$ , the current is given by

$$I(0) = \frac{V_S - V_{C_\tau}(0)}{R_\tau} \quad (3.53)$$

As Fig. 3.19 illustrates, in the beginning of the positive saturation that opamp output becomes  $V_S$ , the voltage across the inverting input terminal of the opamp,  $V_{C_\tau}(0)$  is given by

$$V_{C_\tau}(0) = V_S \beta^- \quad (3.54)$$

Substituting  $V_{C_\tau}(0)$  from (3.54) into (3.53) yields

$$I(0) = \frac{V_S - V_S \beta^-}{R_\tau} \quad (3.55)$$

This equation can be further simplified to

$$I(0) = \frac{V_S(1 - \beta^-)}{R_\tau} \quad (3.56)$$

Replacing  $I(0)$  from (3.56) into (3.52) results in

$$i(t) = \frac{V_S(1 - \beta^-)}{R_\tau} e^{-\frac{t}{\tau}} \quad (3.57)$$

Substituting  $i(t)$  from (3.57) into (3.49) yields

$$V_{C_\tau} = V_S - R_\tau \frac{V_S(1 - \beta^-)}{R_\tau} e^{-\frac{t}{\tau}} \quad (3.58)$$

This equation can be further simplified to

$$V_{C_\tau} = V_S[1 - (1 - \beta^-)e^{-\frac{t}{\tau}}] \quad (3.59)$$

Equation 3.59 describes the voltage across  $C_\tau$  while the opamp is in the positive saturation mode and the opamp output equals  $V_S$ . Using (3.59), we can now calculate  $t_1$  which is the charging time of  $C_\tau$ , or the time that the PWM signal generated by the opamp is high. Therefore,  $t_1$  can be easily calculated by equating (3.59) with  $V_S\beta^+$  and doing some simple algebra, we have

$$t_1 = -\tau \ln\left(\frac{1 - \beta^+}{1 - \beta^-}\right) \quad (3.60)$$

As Fig. (3.19) shows, the time that the generated PWM signal is high is equal to the time this signal is low ( $t_1 = t_2$ ). Thus the period of PWM signal is given by

$$T = -2\tau \ln\left(\frac{1 - \beta^+}{1 - \beta^-}\right) \quad (3.61)$$

As Fig. 3.19 illustrates, the low frequency oscillator circuit can only generate PWM signals with a 50 % duty cycle. The circuit that is shown in Fig.3.20 is used to change the duty cycle of the PWM signal. The main operation of this circuit is similar to the low frequency

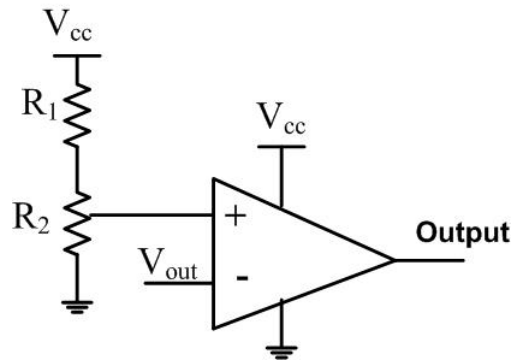


Figure 3.20: Circuit to change the duty cycle of the PWM signal.

oscillator that was described earlier. In the circuit shown in Fig. 3.20,  $V_{out}$  which is the

output of the low frequency oscillator as shown in Fig. 3.17, is applied to the negative input terminal of the opamp. We can change the voltage across the the positive input terminal of the opamp by using a potentiometer ( $R_2$ ). When the value of  $R_2$  changes, the voltage division between  $R_1$  and  $R_2$  changes which results in having different voltage values at the positive input terminal of the opamp. Therefore by connecting the PWM signal generated by the low frequency circuit to the inverting input terminal of the opamp ( $V_{out}$ ), we can change the duty cycle of the PWM signal. Fig. (3.21) illustrates the connection of the energy harvesting circuit and the self-powered MOSFET gate drive.

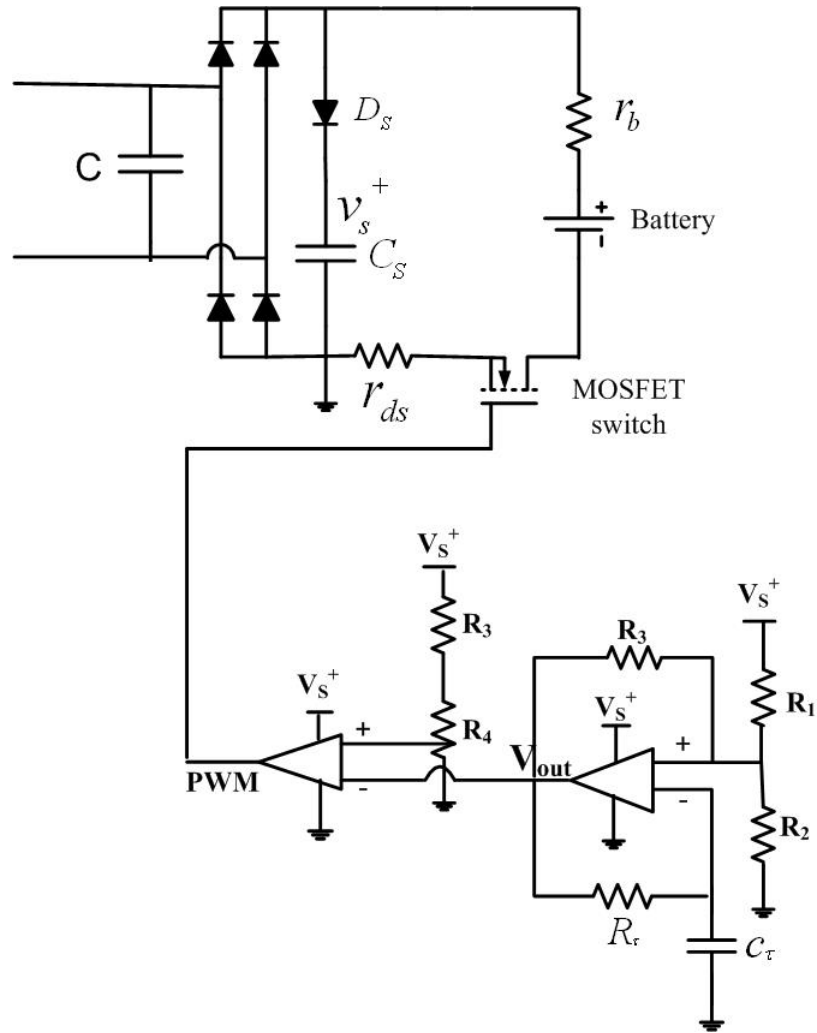


Figure 3.21: Energy harvesting circuit with self-powered MOSFET gate-drive.

### 3.5 Harvested Power and Efficiency of the Circuit

In this section, the average power that is harvested from the source and stored in the battery as well as the power that comes from the source are calculated in one period of MOSFET switching, represented by  $T_{Sw}$  and in one period of signal source, represented by  $T_{Source}$ . Hence, the efficiency of the circuit defined as the ratio of harvested power to the generated power from the harvestable source is obtained.

#### 3.5.1 Harvested Power in the Battery

The power that is stored in the battery in one period of the MOSFET switching can be expressed as the product of  $V_B$  and the average current that flows into the battery in one period of the PWM signal as follows

$$P_{Battery} = V_B \bar{i}_{Battery}. \quad (3.62)$$

Fig. 3.22 shows the current that flows into the battery in one period of switching. As this figure illustrates, when the MOSFET is off, no current flows into the battery. When the MOSFET turns on, two sources of current flow to the battery,  $i_{in}(t)$  and the current that generates as a result of discharging  $C$  into the battery. As this figure shows, when  $C$  is fully discharged to the battery, the only current that flows into the battery is  $i_{in}(t)$ .

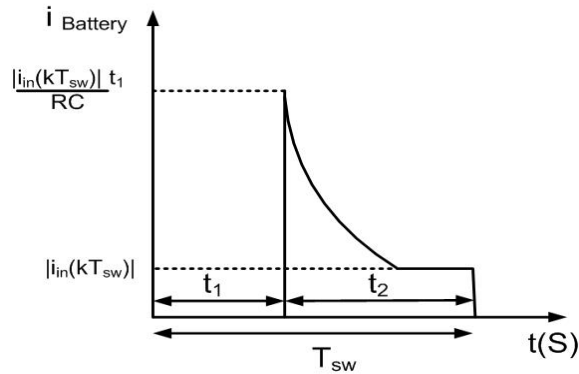


Figure 3.22: Battery current in one period of MOSFET switching.

During the on interval of the MOSFET, the current of the battery is given by

$$i_{Battery}(t) = |i_{in}(t)| + \left( \frac{t_1}{RC} |i_{in}(t)| - |i_{in}(t)| \right) e^{-\frac{t}{RC}}. \quad (kT_{Sw} + t_1 < t < (k+1)T_{Sw}) \quad (3.63)$$

As mentioned earlier, we assumed that  $i_{in}(t)$  is constant in one period of switching. Thus, (3.63) can be simplified to

$$i_{Battery}(t) = |i_{in}(kT_{Sw})| + \left(\frac{t_1}{RC}|i_{in}(kT_{Sw})| - |i_{in}(kT_{Sw})|\right)e^{-\frac{t}{RC}}. \quad (3.64)$$

We can now calculate the average of the current that flows into to the battery during  $T$  as follows

$$\begin{aligned} \bar{i}_{Battery}(kT_{Sw}) &= |i_{in}(kT_{Sw})| \frac{T_{Sw} - t_1}{T_{Sw}} + \\ &\quad \frac{1}{T_{Sw}} \int_0^{T_{Sw}-t_1} \left( \frac{|i_{in}(kT_{Sw})|t_1}{RC} - |i_{in}(kT_{Sw})| \right) e^{-\frac{t}{RC}} dt. \end{aligned} \quad (3.65)$$

Eq. (3.66) can be further simplified to

$$\bar{i}_{Battery}(kT_{Sw}) = |i_{in}(kT_{Sw})| \frac{T_{Sw} - t_1}{T_{Sw}} + \frac{|i_{in}(kT_{Sw})|}{T_{Sw}} (t_1 - RC) (1 - e^{-\frac{T_{Sw}-t_1}{RC}}). \quad (3.66)$$

In practice, the switching frequency of the MOSFET is in the range of 100 – 800Hz,  $R$  is small in the range of 1 – 10Ω, and  $C$  is small as well, in the range of nF. Thus we can make the assumption that  $t_1 \gg RC$  and  $1 \gg e^{-\frac{T_{Sw}-t_1}{RC}}$ . Therefore, (3.66) becomes

$$\bar{i}_{Battery}(kT_{Sw}) = |i_{in}(kT_{Sw})| \frac{T_{Sw} - t_1}{T_{Sw}} + |i_{in}(kT_{Sw})| \frac{t_1}{T_{Sw}}. \quad (3.67)$$

Eq. 3.67 can be further simplified to

$$\bar{i}_{Battery}(kT_{Sw}) = |i_{in}(kT_{Sw})|. \quad (3.68)$$

We can now calculate the average power that is stored in the battery during one period of the MOSFET switching by substituting (3.68) into (3.62), i.e.,

$$P_{Battery} = V_B |i_{in}(kT_{Sw})|. \quad (3.69)$$

After obtaining the average power of battery in one period of the MOSFET switching, the next step is to calculate  $P_{Battery}$  in one period of the source signal. By assuming that  $i_{in}(t) = A \sin(\frac{2\pi}{T_{Source}}t)$ , the average power stored in the battery in one period of the source signal is given by

$$\bar{P}_{Battery} = \frac{1}{T_{Source}} \sum_{k=0}^{\frac{T_{Source}}{T_{Sw}}} V_B |i_{in}(kT_{Sw})|. \quad (3.70)$$



Since the switching frequency is much higher than then source frequency ( $f_{Sw} \gg f_{Source}$ ), (3.70) can be further written as

$$\bar{P}_{Battery} = \frac{1}{T_{Source}} \int_0^{T_{Source}} V_B |i_{in}(\frac{2\pi}{T_{Source}}t)|. \quad (3.71)$$

By obtaining the integral term in (3.76) , the average power of battery during  $T_{Source}$  is given by

$$\bar{P}_{Battery} = V_B \times \frac{2A}{\pi} \quad (3.72)$$

### 3.5.2 Extracted Power

In this section, the average power extracted from the source in one  $T_{Sw}$  and in one  $T_{Source}$  are obtained. The power during one  $T_{Sw}$  is given by

$$P_{in} = \bar{v}_{in} \bar{i}_{in}(t). \quad (3.73)$$

As mentioned earlier, we assumed that  $i_{in}$  is constant during one period of PWM signal and  $\bar{v}_{in}$  is the voltage across  $C$  obtained from (3.19). Therefore, substituting  $\bar{v}_P$  from (3.19) into (3.73) results in

$$P_{in} = V_{DC} |i_{in}(kT_{Sw})| + R_{eq}(i_{in}(kT_{Sw}))^2. \quad (3.74)$$

Now, we can calculate  $P_{in}$  in one period of the source signal by assuming  $i_{in}(t) = A \sin(\frac{2\pi}{T_{Source}}t)$  given by

$$\bar{P}_{in} = \frac{1}{T_{Source}} \left[ \sum_{k=0}^{\frac{T_{Source}}{T_{Sw}}} V_{DC} |i_{in}(kT_{Sw})| + \sum_{k=0}^{\frac{T_{Source}}{T_{Sw}}} R_{eq}(i_{in}(kT))^2 \right]. \quad (3.75)$$

Assuming that the switching frequency is much higher than the source frequency, ( $f_{Sw} \gg f_{Source}$ ), (3.75) can be written as

$$\bar{P}_{in} = \frac{1}{T_{Source}} \left[ \int_0^{T_{Source}} V_{DC} |i_{in}(\frac{2\pi}{T_{Source}}t)| dt + \int_0^{T_{Source}} R_{eq}(i_{in}(\frac{2\pi}{T_{Source}}t))^2 dt \right] \quad (3.76)$$

By solving the above integrals, the source average power during  $T_{Source}$  is obtained as

$$\bar{P}_{in} = V_{DC} \frac{2A}{\pi} + R_{eq} \frac{A^2}{2}. \quad (3.77)$$

Substituting  $V_{DC}$  and  $R_{eq}$  with  $V_B + 2V_D$ , and  $\frac{(1-d)^2 T_{Sw}}{2C} + R(1-d)$  respectively, (3.77) becomes

$$\bar{P}_{in} = V_B \frac{2A}{\pi} + V_D \frac{2A}{\pi} + \left[ \frac{(1-d)^2 T_{Sw}}{2C} + R(1-d) \right] \frac{A^2}{2}. \quad (3.78)$$

### 3.5.3 Efficiency of the Low Power Electronics Circuit

In this section the efficiency of the proposed power electronics circuit is obtained in one period of MOSFET switching and also in one period of source signal. The efficiency of the circuit is given by

$$\eta = \frac{P_{Battery}}{P_{in}}. \quad (3.79)$$

Substituting  $P_{in}$  and  $P_{Battery}$  from (3.74) and (3.69) respectively, (3.79) becomes

$$\eta = \frac{V_B}{V_B + 2V_D + R_{eq} |i_{in}(kT_{Sw})|}. \quad (3.80)$$

This equation represents the efficiency of the proposed circuit in one period of PWM signal. This equation reveals that the efficiency of the proposed converter is not a function of the vibration or switching frequency. From (3.80), by reducing the forward voltage drop of the diodes used in the diode bridge, the efficiency of harvested power will increase. Furthermore, by decreasing the value of  $R_{eq}$  we can increase the efficiency. And the efficiency of the proposed energy harvesting circuit in one period of source signal by assuming  $i_{in}(t) = A \sin(\frac{2\pi}{T_{Source}})t$  is given by

$$\eta = \frac{V_B}{V_B + 2V_D + R_{eq} \frac{|A|\pi}{4}}. \quad (3.81)$$

## 3.6 Applications of the Proposed Low-Power Electronics Circuitry

In this section two applications of the proposed circuit are discussed. The first application is to use this circuit to harvest solar energy and the second application is to harvest vibrational energy.

### 3.6.1 Harvesting solar energy using solar cell

One of the main applications of this circuit is to harvest solar energy using a solar cell. Equation. (3.25) indicates that the equivalent resistance of the circuit  $R_{eq}$  is a factor of the frequency and duty cycle of the switching period, and also  $C$ . Thus by changing these three values, we can change the magnitude of the input resistance of the converter. As mentioned in the first chapter, in order to get the maximum power from a solar module, the operating point of the panel should be Maximum Power Point (MPP) as it is shown in Fig. 3.23. As indicated in chapter one, one of the methods to track MPP is called the Incremental- Conductance- Technique. In this technique, it is proved that to track MPP, the input impedance of the converter that is connected to the solar cell should be equal to  $\frac{\partial V}{\partial I}$ . Thus by using the proposed converter, the input impedance of the converter can be adjusted to be equal to  $\frac{\partial V}{\partial I}$ , so the solar panel can generate the maximum power which results in having the maximum efficiency.

Fig. 3.24 shows the flowchart of incremental conductance method using the proposed converter in this work. As mentioned earlier in ICT, the goal is to reach  $-\frac{dV}{dI} = \frac{V}{I}$ .  $\frac{V}{I}$  is in fact the input impedance of the converter that is connected to the solar cell which is a function of the duty cycle of the switching. Thus, as this flowchart shows, at each sample time, if  $-\frac{dV}{dI} > \frac{V}{I}$ , the duty cycle of the switching should decrease to increase the value of  $\frac{V}{I}$ . Else if  $-\frac{dV}{dI} < \frac{V}{I}$ , the duty cycle of the switching should increase to decrease the value of  $\frac{V}{I}$ .

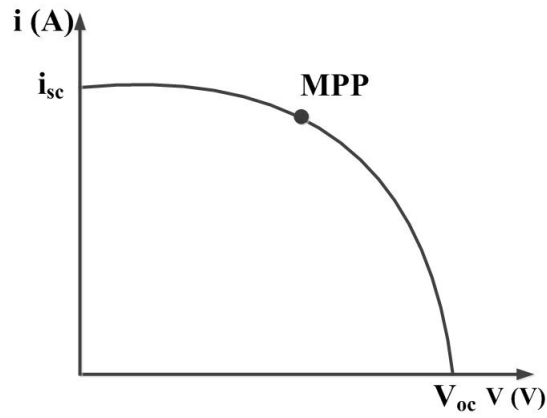


Figure 3.23: Current-Voltage curve of a solar cell.

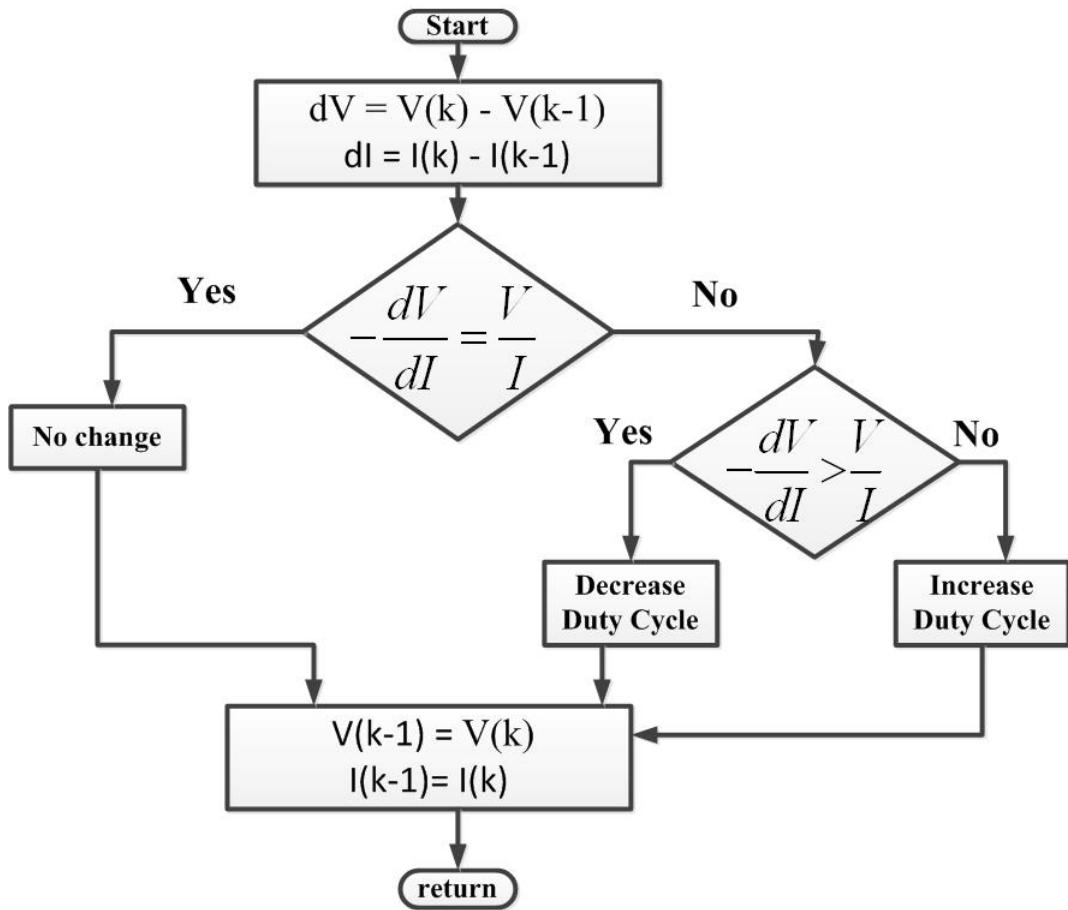


Figure 3.24: Flowchart of Incremental Conductance Method.

### 3.6.2 Harvesting Vibrational Energy using Piezoelectric Transducers

Equation (3.19) reveals that the proposed circuit has a resistive behavior between the input voltage and current of this circuit and this behavior works for any given frequency. In harvesting vibrational energy using piezoelectric transducer, the generated voltage is composed of multi-frequencies. Therefore, this circuit can be used in applications in which the energy source contains multiple frequencies or the frequency may change dynamically, such as harvesting mechanical vibration as a result of passing vehicles in the street or passing trains on a rail track.

# Chapter 4

## Simulation Studies of the Proposed Circuit

### 4.1 Introduction

In this chapter, simulation studies are conducted to validate the theoretical results of the circuit discussed in chapter 2. The circuit was implemented in the Matlab/Simulink environment using the SIMPowerElectronics toolbox and also LTspice. In both the simulation environments, vibrational piezoelectric model was used as the input source. In the first simulation study, a PWM block was used to generate PWM signal to drive the MOSFET switch in the circuit and in the second simulation, the second configuration of the driven circuit that is self-powered was used.

### 4.2 Simulation Studies of the Proposed Circuit Using Independent Voltage Source

Fig. 4.1 shows, the piezoelectric transducer model which is comprised of an AC current source in parallel with a resistor and a capacitor. Referring to Fig. 2.1, the circuit consists of a capacitor at the input of the circuit which can represent the piezo capacitor. The internal capacitor of the piezo was thus used as the input capacitor of our circuit as shown in Fig.

4.2. This figure illustrates the implementation of the vibrational piezoelectric transducer model and the converter in Maltlab Simulink environment. As this figure shows, an ac current source block, a capacitor and a resistor are used to model the piezo. To implement the ac/dc rectifier, the diode bridge block was used. In this block, the forward voltage drop of the diodes is adjustable. In this work, the forward voltage drop of each diode is 0.7V. To drive the MOSFET, a pulse generator block that generates PWM signals is used. The duty cycle and frequency of the signal can be determined in this block. Referring to (2.20), to

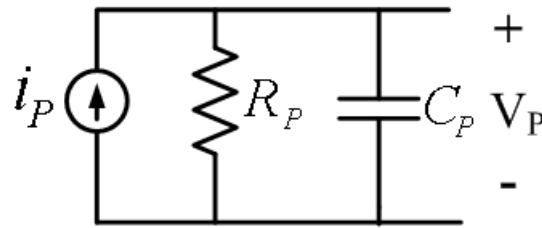


Figure 4.1: Piezoelectric model.

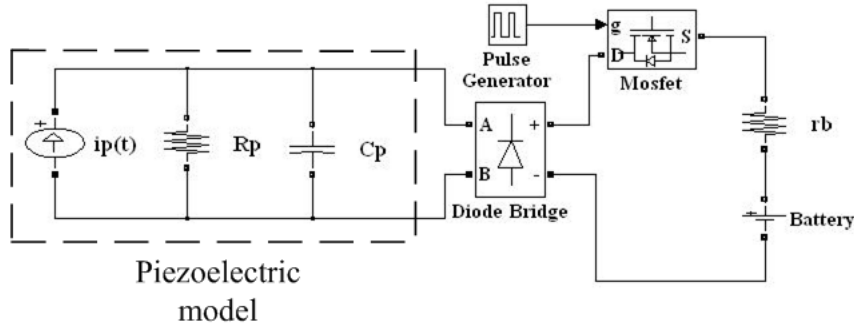


Figure 4.2: Implementation of the piezoelectric transducer and energy harvesting circuit in Maltlab/ Simulink environment.

verify the input resistance of the circuit,  $i_{in}$  should be measured. To measure this current, a small resistance  $r$  is added to the circuit, as shown in Fig. 4.3. Hence  $i_{in}$  can be obtained using the following equation

$$i_{in} = C_P \frac{dV_P}{dt} + \frac{V_r}{r} \tag{4.1}$$

In the first simulation, we validated the resistive behavior of the circuit. As Fig. (4.4)

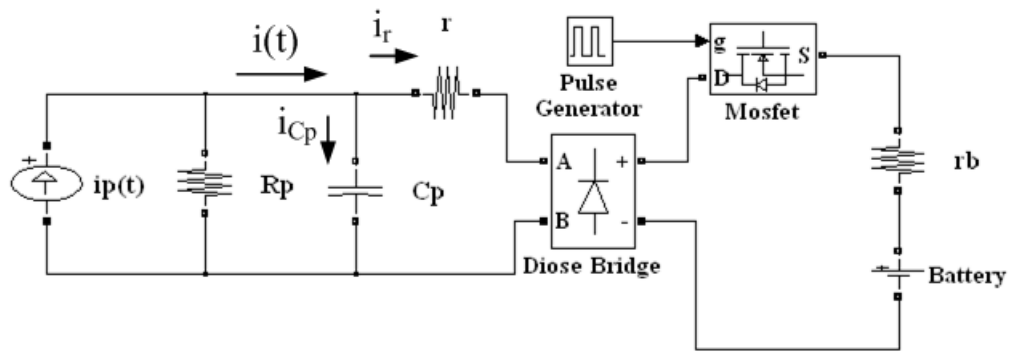


Figure 4.3: Circuit implementation in Maltlab/ Simulink environment.

shows, the input voltage of the converter  $v_p$  and the input current of the converter  $i_{in}(t)$  are in phase.

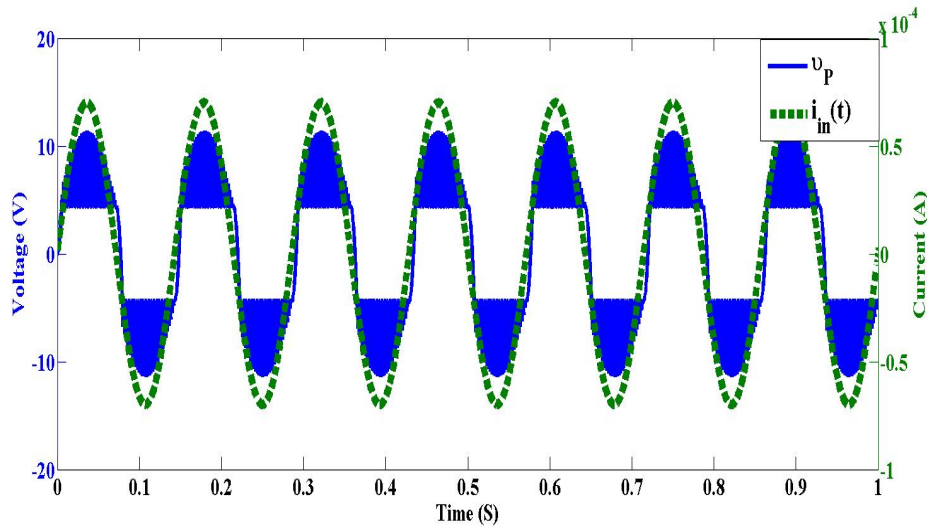


Figure 4.4: Input voltage and current of the circuit for a single frequency mechanical vibration.

Fig. 4.5 illustrates the input voltage and input current of the converter when the current input source  $i_p$  contains multi frequencies. As this figure shows, for a multi-frequency mechanical vibration,  $V_p$  and  $i_{in}$  are in phase. In other words, the circuit has resistive input behavior even if the harvestable source connected to the circuit contains multi frequencies.



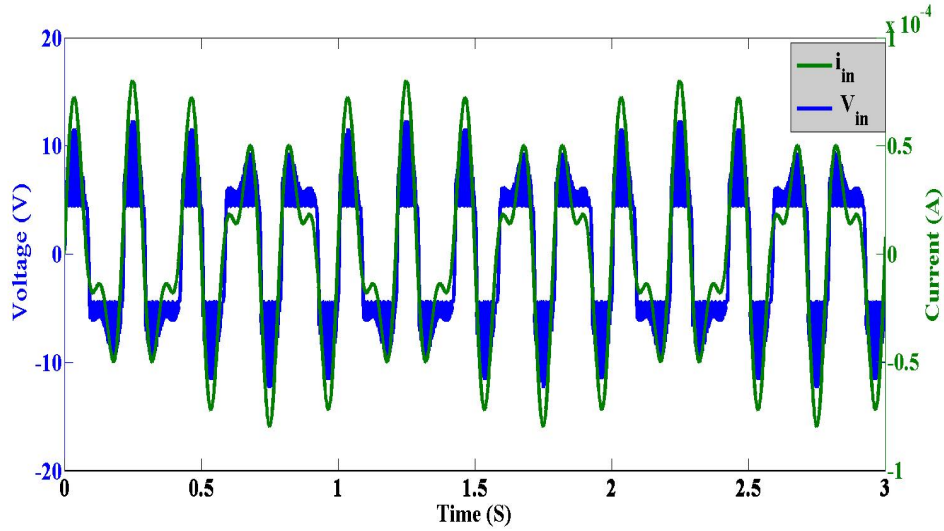


Figure 4.5: Input voltage and current of the circuit for a multi frequency mechanical vibration.

In the next simulation, we validated the expression for input resistance of the converter, given by (3.25). As this expression shows,  $R_{eq}$  is a function of frequency and duty cycle of the MOSFET switching. Fig. 4.6 shows the theoretical and simulation values for  $R_{eq}$  at two different frequencies and different values of duty cycle as well. As this figure illustrates, theoretical and simulation results are quite in agreement.

A low pass filter was used to apply the averaging technique. In simulink environment, a transfer function block was used to implement a low pass filter. The time constant of the transfer function equals 0.0025.

Fig. 4.7 illustrates the averaging method that is applied to the input voltage of the converter  $V_{in}$ . In this figure, the voltage across the piezoelectric, which is the the input voltage of the circuit, is shown before and after applying the signal to a low-pass filter. In this simulation,  $i_P(t) = 50\text{Sin}(2\pi t)\mu\text{A}$ ,  $C_P = 10\text{nF}$  and the switching frequency is  $500\text{Hz}$ . Fig. 4.8 shows the averaging method for a multi-frequency signal as the input. In this simulation,  $i_P(t) = 50\sin(10\pi t) + 30\sin(18\pi t)$ .

Fig. 4.9 illustrates the average power of the source and battery in period of source signal. In this simulation,  $i_{in}(t) = 50\sin(20\pi t)\mu\text{A}$  and  $V_B = 4\text{V}$ . As this figure shows,  $\bar{P}_{in} = 19 \times 10^{-5}\text{w}$  and  $\bar{P}_{battery} = 12.1 \times 10^{-5}\text{w}$ . Using 3.72 and 3.77,  $\bar{P}_{in}$  and  $P_{battery}$  are respectively

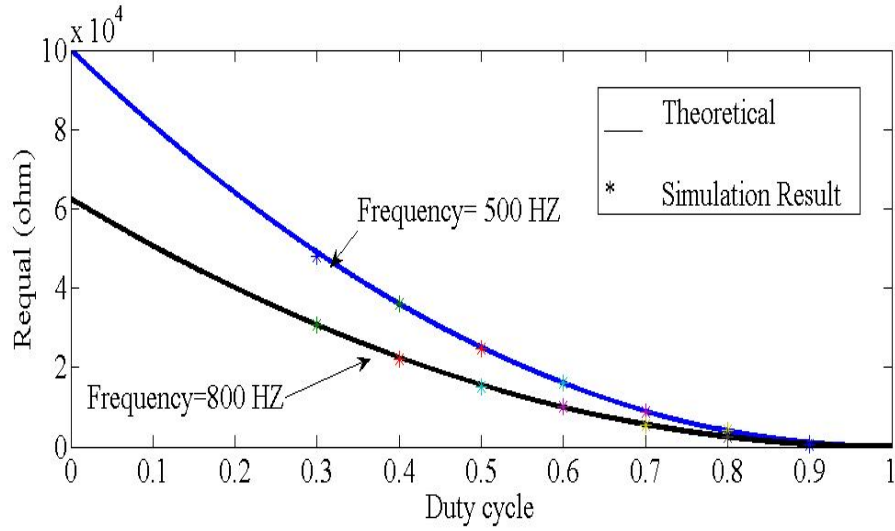


Figure 4.6: Input resistance of the converter as a function of switching frequency and duty cycle.

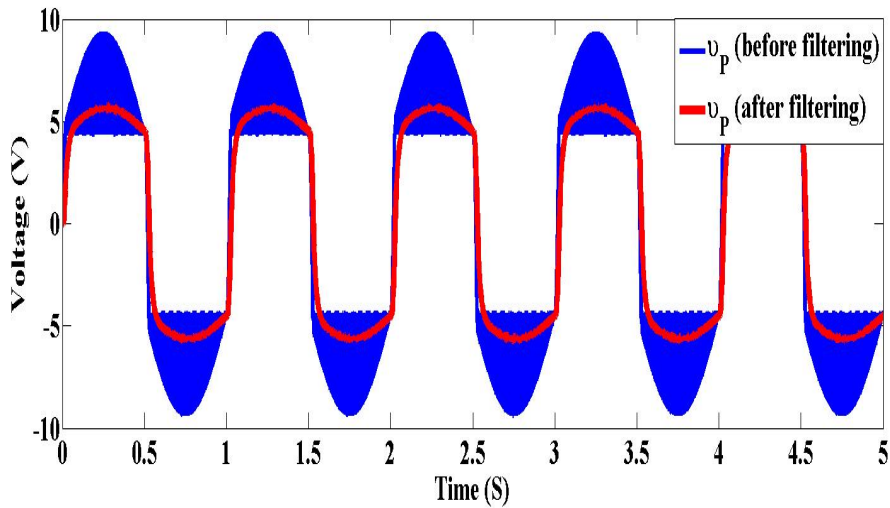


Figure 4.7: Piezoelectric voltage before and after applying the low-pass filter for a single frequency vibration.

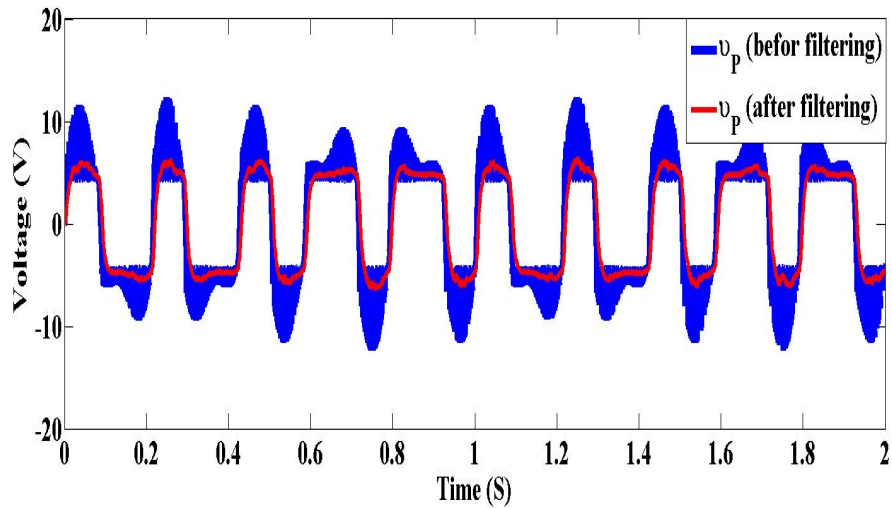


Figure 4.8: Piezoelectric voltage before and after applying the low-pass filter for a multi-frequency vibration.

$20.2 \times 10^{-5}W$  and  $12.7 \times 10^{-5}W$  which are quite in agreement with simulation results.

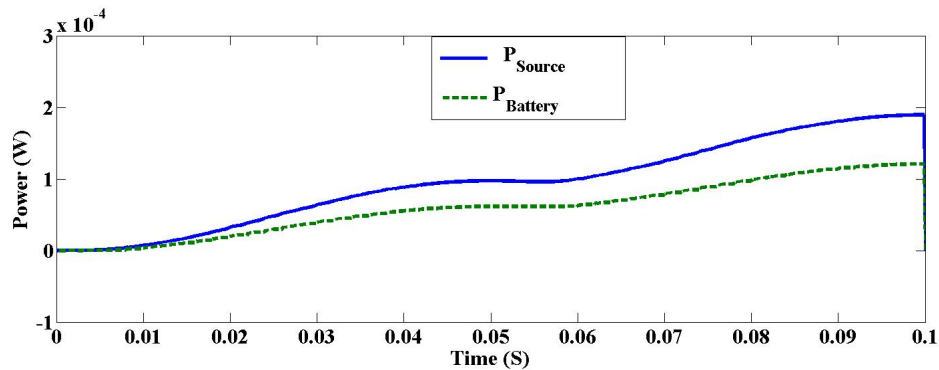


Figure 4.9: Average power of the source and battery in one period of source signal.

In the next simulation result shown in Fig. 4.10, the efficiency of the proposed circuit is considered as a factor of the switching duty cycle. In this simulation, the switching frequency is  $500Hz$ ,  $V_D = 0.7V$ ,  $V_B = 4V$ , and  $i_{in} = 50\sin(20\pi t)\mu A$ . As this figure shows, by increasing the duty cycle of the switching, the efficiency of the energy harvesting circuit increases.

Fig. 4.11 shows the efficiency of the converter as a factor of the forward voltage drop of

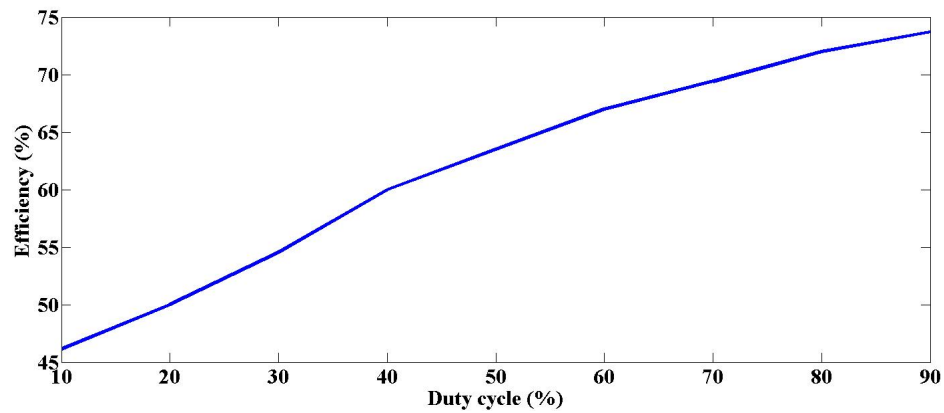


Figure 4.10: Efficiency of the proposed energy harvesting circuit as a function of the duty cycle of the MOSFET switching

diodes in the diode bridge. It can be observed that by reducing  $V_D$ , the efficiency of the circuit increases.

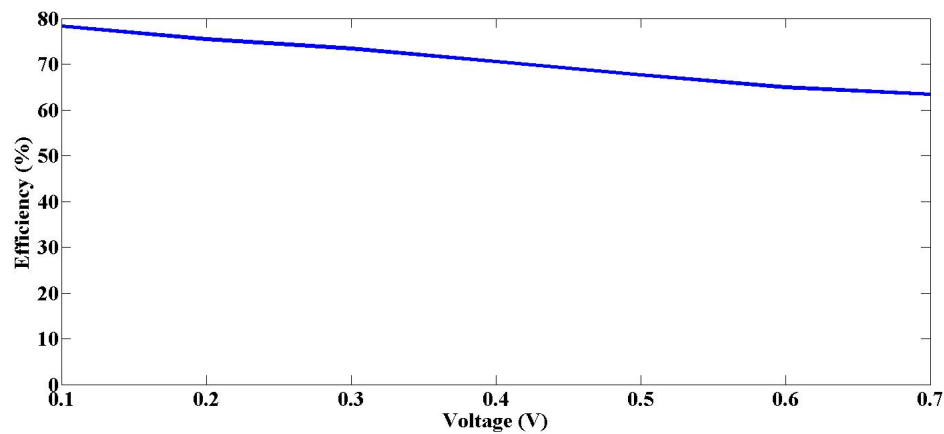


Figure 4.11: Efficiency of the proposed converter as a function of the forward voltage drop of diodes in the diode bridge.

### 4.3 Simulations Studies of the Proposed Circuit using Self-Powered Driven Circuit

In this simulation study, the piezoelectric model is connected to the proposed converter. The self-powered MOSFET gate drive circuit which described in chapter 2 was used to drive the MOSFET, as shown in Fig. 4.12. Referring to this figure, the peak detector which consists of a capacitor represented by  $C_S$  and a diode represented by  $D_S$  is used to power the driven circuit. In this simulation study, LTspice simulation environment was used. In this simulation  $C_S = 20\mu F$ ,  $R_1 = R_2 = 120K\Omega$ ,  $R_\tau = 50K\Omega$ , and  $C_\tau = 10nF$ .

In the first simulation, the resistive behavior of the converter is studied and the results are shown in Fig. 4.13. As this figure shows, the input voltage and current of the converter are in phase. In other words, the proposed energy harvesting circuit has input resistive behavior. In the next simulation, the resistive behavior of the converter is considered when the mechanical vibration is multi-frequency. The result of this simulation is shown in Fig. 4.14. As this figure illustrates, the input voltage and current of the converter remain in phase when the mechanical vibration is multi-frequency. Fig. 5.17 illustrates the charging and discharging of  $C_P$  as a function of the voltage across the MOSFET switch. Referring to this figure, when the voltage across the gate-source of the MOSFET is less than the threshold voltage of the MOSFET, then the MOSFET switch is off. In this case, no current flows into the battery and the current source charges the internal capacitor of the piezoelectric. Thus the voltage across the piezoelectric transducer increases in this time. When the voltage across the gate-source of the MOSFET is greater than the threshold voltage of the MOSFET, the MOSFET turns on and  $C_P$  discharges to the battery. In this case,  $V_P$  decreases as a result of discharging to the battery. In the next simulation study, the averaging method that is used in this work and described in chapter two, is considered. Fig. 4.16 illustrates the voltage across the piezoelectric transducer before and after applying the signal through a low pass filter.

The next simulation was conducted to validate the resistive expression of the converter given by (3.25). Fig. 4.17 shows the theoretical and simulation values of  $R_{eq}$  of the converter at PWM frequency of  $500Hz$ . In this simulation,  $C_P = 7nF$  and  $V_{DC} = 3.5V$ . In the last simulation, the behavior of the peak detector is considered. As Fig. 4.18 shows,  $C_P$

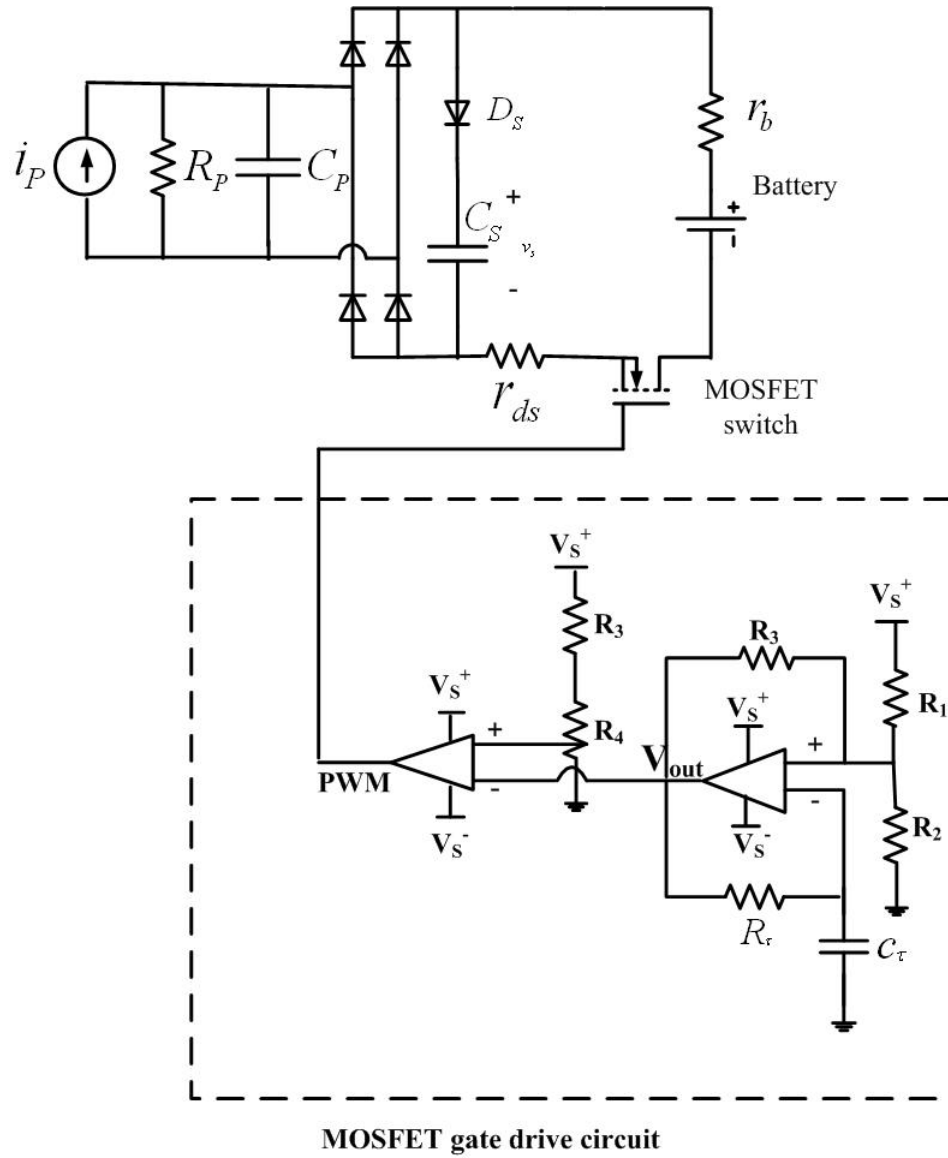


Figure 4.12: Implementing the piezoelectric transducer model and the converter in simulink environment.

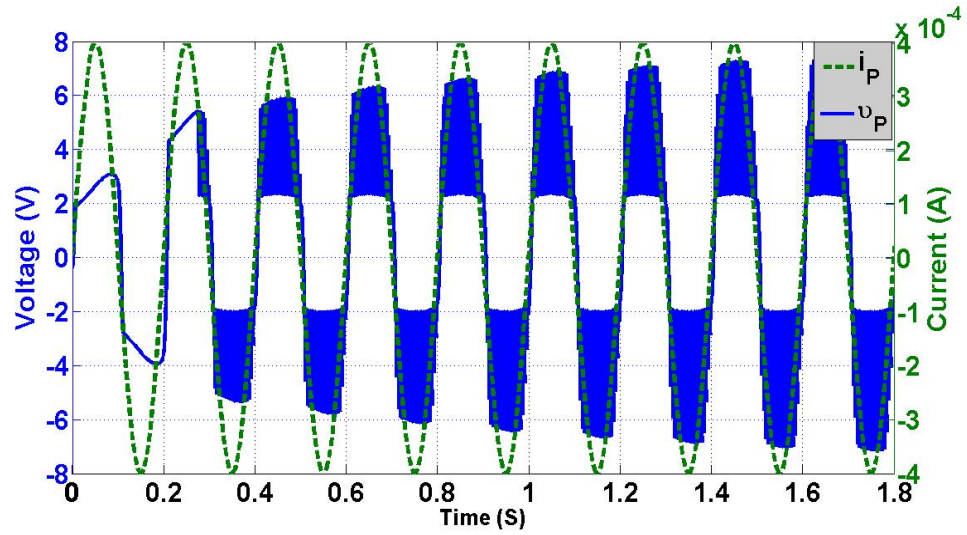


Figure 4.13: Input current and voltage of the converter for a single frequency vibration.

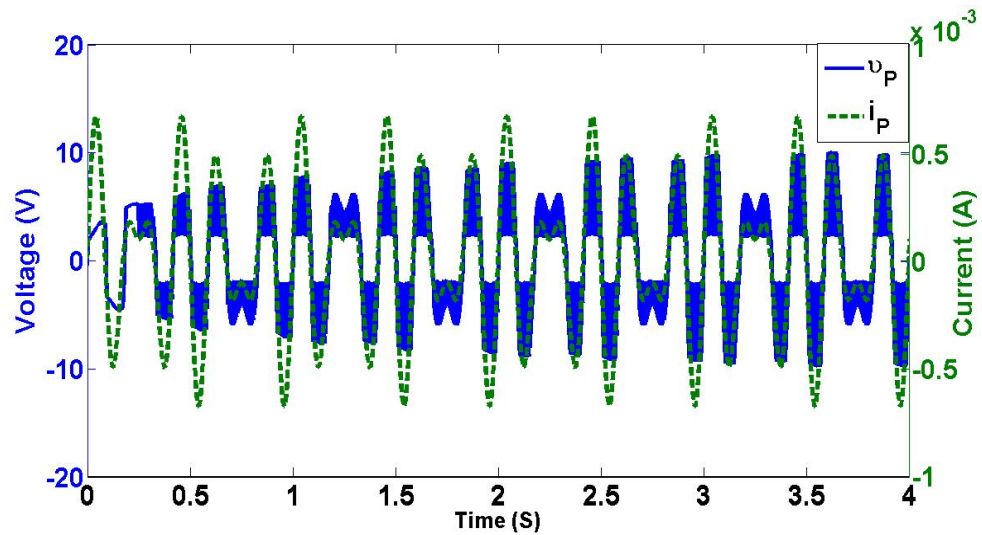


Figure 4.14: Input current and voltage of the converter for a multi frequency excitation.

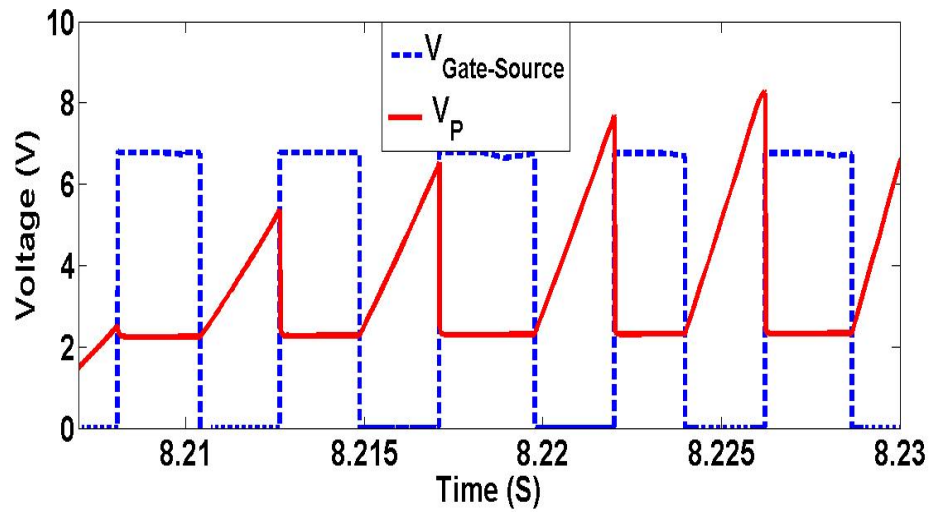


Figure 4.15: Charging of the capacitor when MOSFET is off ( $V_{gate-source} = 0V$ ) and discharging of the capacitor when MOSFET is on ( $V_{gate-source} = 10V$ ).

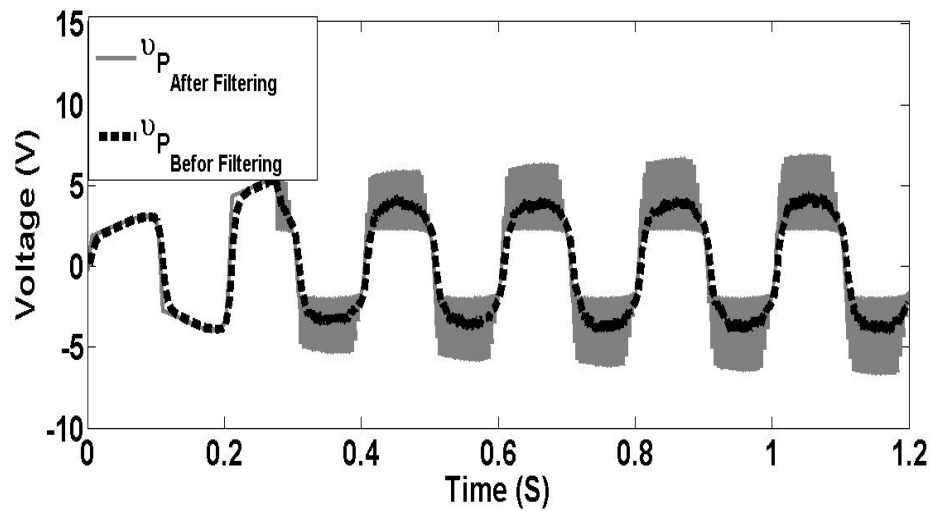


Figure 4.16: Voltage across the piezoelectric before and after applying the low pass filter.



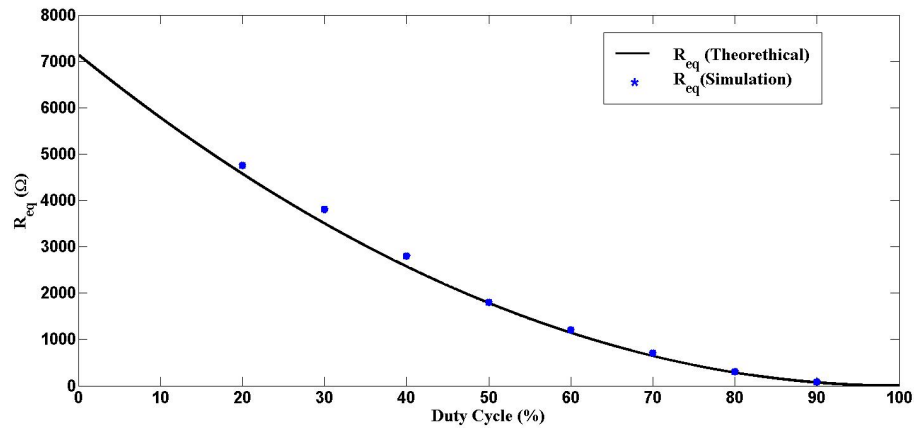


Figure 4.17: Theoretical and simulation results for the input resistance of the converter.

keeps track of the voltage across the piezoelectric transducer. Referring to Fig. 4.12,  $D_S$  does not let  $C_P$  to discharge in the circuit. Thus the voltage across  $C_S$  is trapped and is used to power the opamps in the MOSFET gate drive circuit.

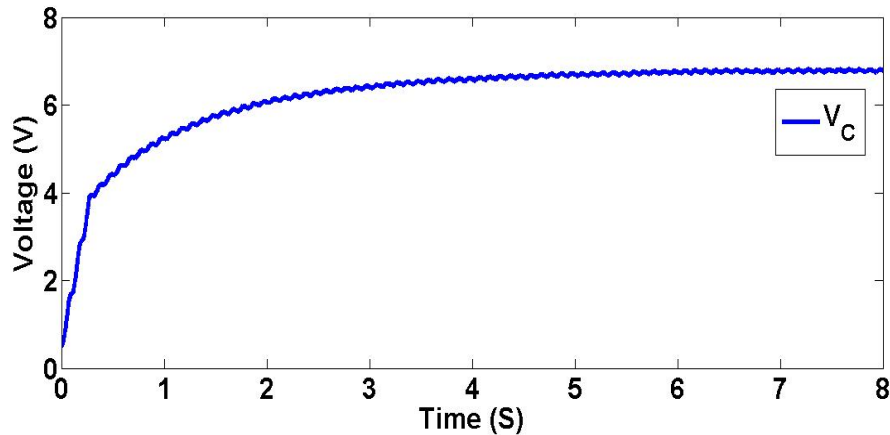


Figure 4.18: The voltage across the storing capacitor of the peak detector.

## 4.4 Conclusion

In this chapter, simulation studies were conducted to validate the theoretical analysis of the proposed circuit. In these simulations, a vibrational piezoelectric transducer model was

used as the source of energy. A vibrational piezoelectric transducer model consists of an ac current source in parallel with a capacitor and a resistor.

The results of the simulation studies reveal that the input voltage and current of the proposed circuit are in phase. Thus, the circuit has resistive behavior regardless of the frequency or amplitude of the input current signal. Besides, the expression for input resistance of the circuit given by (3.25) was verified. The expression for extracted power from the source and the harvested power in the battery were verified as well.

The efficiency of the circuit was studied as a function of the duty cycle of the switching and forward voltage drop of the diodes. The results of this study indicate that by increasing the duty cycle of the MOSFET switching and reducing the forward voltage drop of the diodes in the diode bridge, the efficiency of the harvested power will increase.

## Chapter 5

# Experimental Studies of the Proposed Circuit

In this chapter, the details of experimental studies are presented to validate performance of the proposed power electronics circuits and the controller discussed in chapter 2. In the first experiment, a time-varying voltage source in series with a resistor is connected to the input of the circuit. In this experiment, a resistive expression of the circuit given by (3.25) was validated. Furthermore, performance of the PI controller to achieve the desired resistance was studied. In the second experiment, a piezoelectric transducer was used as the source to provide current to the circuit. In this experiment, theoretical analysis of the circuit was validated and a PI controller is applied to the circuit to adjust the value of the input resistance of the circuit  $R_{eq}$  to a desired value by tuning the duty cycle of the MOSFET switching. In the last experiment discussed in Section 4.3, the self-powered MOSFET gate drive was implemented and the performance of the circuit was validated by using a vibrational piezoelectric transducer as the source connected to the input of the circuit.

## 5.1 Experimental Studies of the Proposed Converter using Independent Voltage Source

### 5.1.1 Circuit Implementation

In this experiment, a floating voltage source in series with a resistor was used as a source to provides current to the circuit. The system was implemented in the Matlab/Simulink environment using the *SIMPowerElectronics* and *Realtime Workshop* toolboxes and the DS1104 controller board from *dSpace, Inc* [59]. Two DAC channels of the DS1104 were used to implement the float voltage source as it is shown in Fig. (5.1).

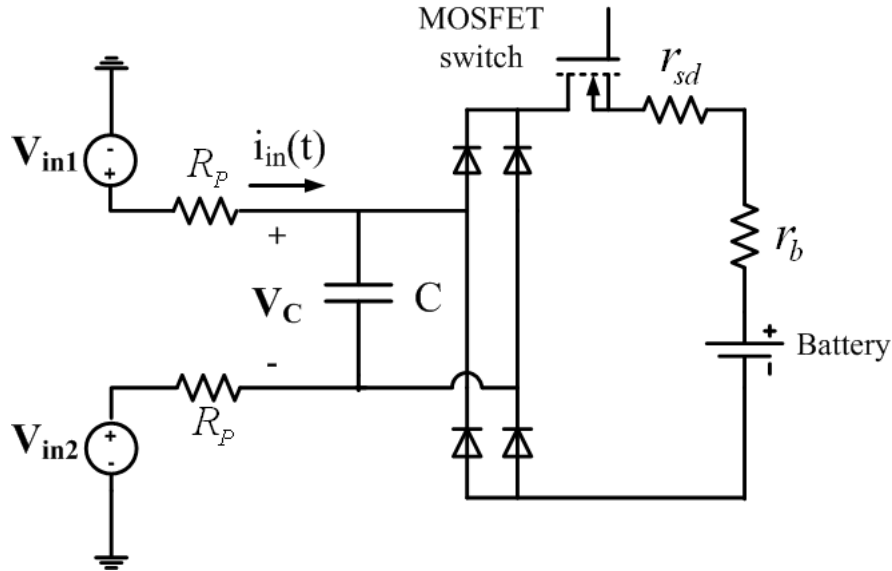


Figure 5.1: Connection of float voltage source to the circuit.

The power electronics circuit consists of an N-channel MOSFET switch (IRF540) [60] with low gate charge for high frequency converters, four diodes (1N4148) [61], and two NiCd rechargeable batteries with high charging capacity (2650 mA) [62]. The MOSFET operates at a PWM frequency of 500Hz generated using the Matlab/Simulink environment, real-time interface of the dSPACE system and the positive feedback that was used to drive the MOSFET gate. An optocoupler (4N26) [63] with low rising and falling times and an NPN switching transistor (PN2222A) [64] were used to implement the positive feedback.

Fig. 5.2 illustrates the connection of the circuit, controller, and the PC. The controller has eight DACs that two of them are used to implement the float voltage source. To measure the capacitor voltage  $v_C$ , two ADC channels of DS1104 were used and the capacitor voltage was measured by calculating the difference voltage between these two channels. By using a DAC channel of the dSPACE, the PWM signal that was generated by the controller and applied to the positive feedback circuit and then to the MOSFET gate.

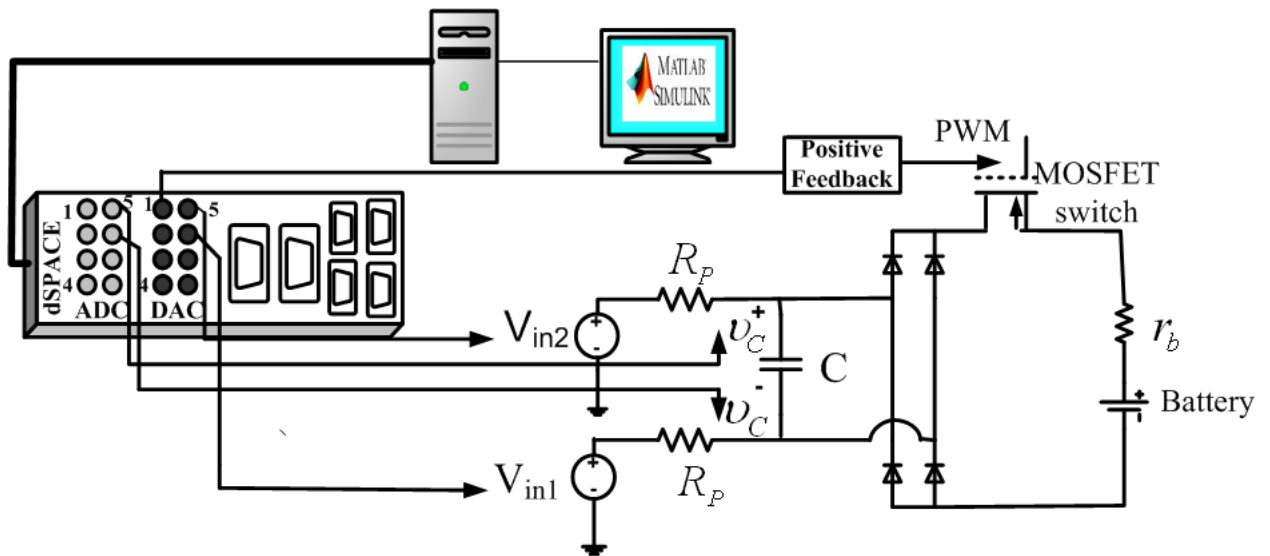


Figure 5.2: Connection of the power electronics circuit, dSPACE, and the PC.

The power electronics circuit is shown in Fig. (5.3) which consists of the converter, the positive feedback (MOSFET gate drive), and the rechargeable batteries.

The implementation of the controller is illustrated in Fig. 5.4. The inputs of the controller are  $v_{in}$  and  $v_C$ . The difference between these two inputs which is the error is the input to the PI controller. The Matlab/Simulink environment, *SIMPowerElectronics*, and *Realtime Workshop* toolboxes were used to implement the controller. As mentioned in chapter 2, a PI controller is used to tune the duty cycle of the PWM signal in order to adjust the Pseudo-resistive input of the energy harvesting circuit to the desired value. As (3.29) indicates, the PI controller determines the value of the duty cycle  $\Delta d$ , which is added to the nominal value of duty cycle  $d_n$ .

As Fig. 5.4 illustrates, to generate the 500Hz PWM signal, a relational operation and a

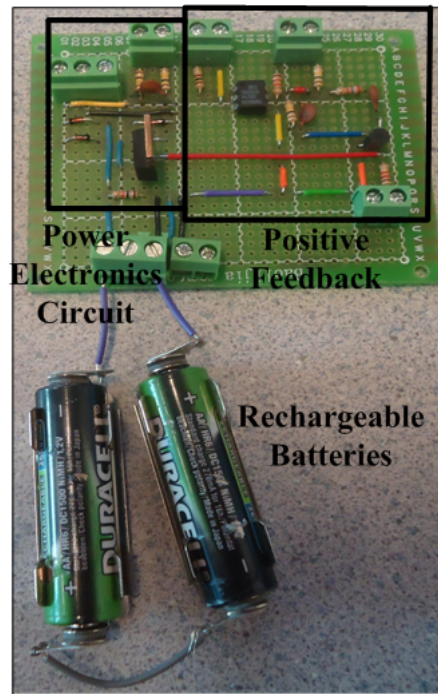


Figure 5.3: Power electronics circuit and the positive feedback

sawtooth block were used in the Matlab/Simulink environment and the PWM signal that is generated using this method is applied to the positive feedback. As Fig (5.4) shows the output of the positive feedback circuit is connected to the MOSFET gate to drive the MOSFET.

Fig. 5.5 shows the experimental setup which consists of a PC, controller dSPACE 1104, DC power supply, the power electronics circuitry, and the rechargeable batteries.

### 5.1.2 Experimental results

In this section, the experimental results of using a floating voltage source in series with a resistor that is connected to the circuit, shown in Fig. 5.1, are presented.

In the first experiment we evaluated the charging and discharging of the capacitor. Fig. 5.6 shows the capacitor voltage  $v_C$  and the voltage source  $v_{in}$ . Referring to this figure,  $v_C$  is equal to  $v_{in}$  until the capacitor voltage  $v_C$  exceeds  $V_B + 2V_D$ . At this voltage, the capacitor  $C_p$  is able to turn on the diode bridge. Thus, when the MOSFET switch is off,  $C$  continues

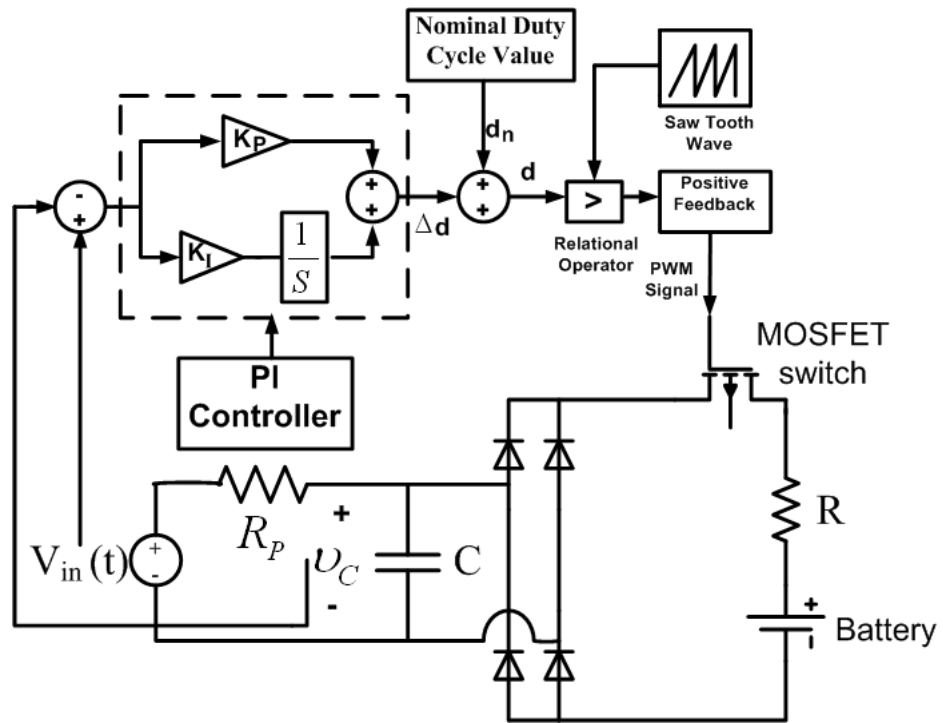


Figure 5.4: Implementation of PI controller.

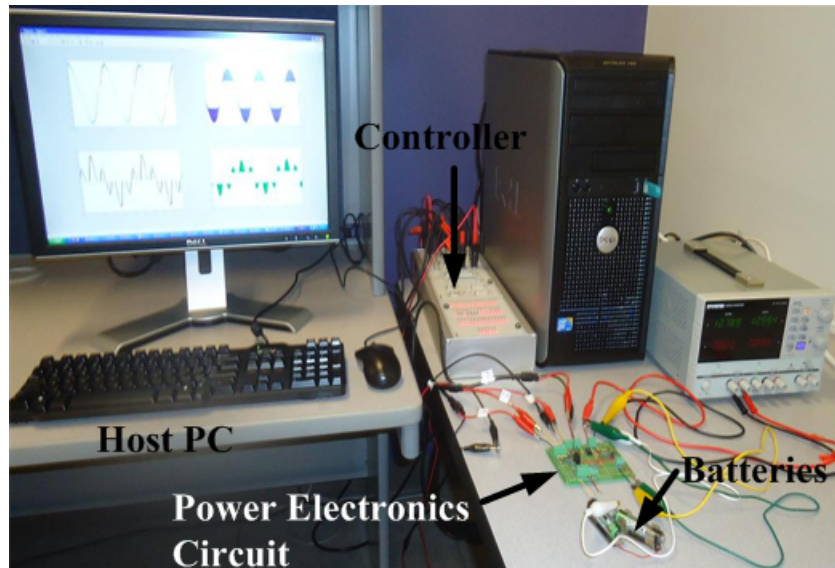


Figure 5.5: Experimental setup.

charging and when the MOSFET switch is on, the capacitor discharges to the battery until its voltage is equal to  $V_B + 2V_D$ , after which  $v_C$  remains constant until the MOSFET turns off and the voltage source  $v_{in}$  charges the capacitor.

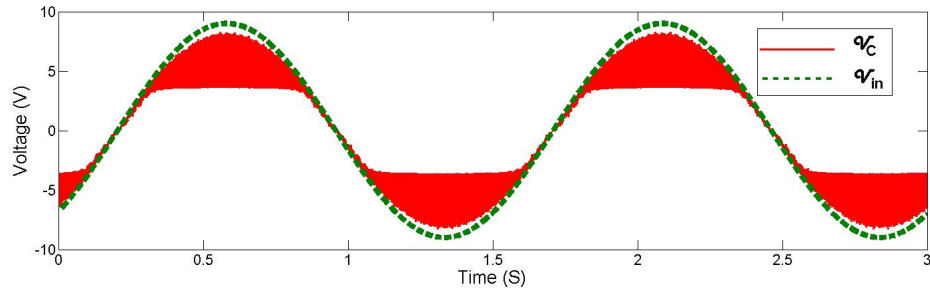


Figure 5.6: Capacitor Voltage  $v_C$  and Voltage source  $v_{in}$  waveforms.

Fig. 5.7 shows the charging and discharging of  $C$  as a function of the voltage across the gate-source of the MOSFET,  $V_{gate-source}$ . When  $V_{gate-source} < 10V$ , the MOSFET is off and  $v_C$  increases. Similarly, when  $V_{gate-source} = 10V$ , the MOSFET turns on and  $C$  discharges to the battery, which continues until its voltage is equal to  $V_B + 2V_D$ .

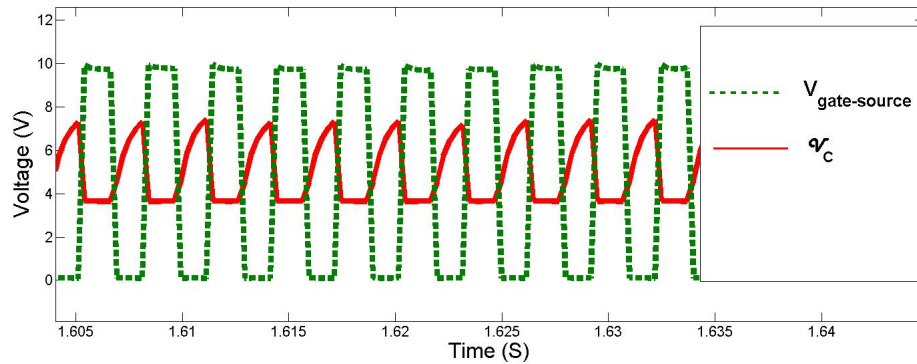


Figure 5.7: Charging of the  $C$  when MOSFET is off ( $V_{gate-source} = 0V$ ) and discharging of  $C$  when MOSFET is on ( $V_{gate-source} = 10V$ ).

Fig. 5.8 illustrates the capacitor voltage along with the averaged voltage obtained by applying the switched signal to a low-pass filter. As this figure shows, the low-pass filter does not result in phase shift in the signal. In other words, the switched signal is in phase with the signal after applying the low-pass filter.



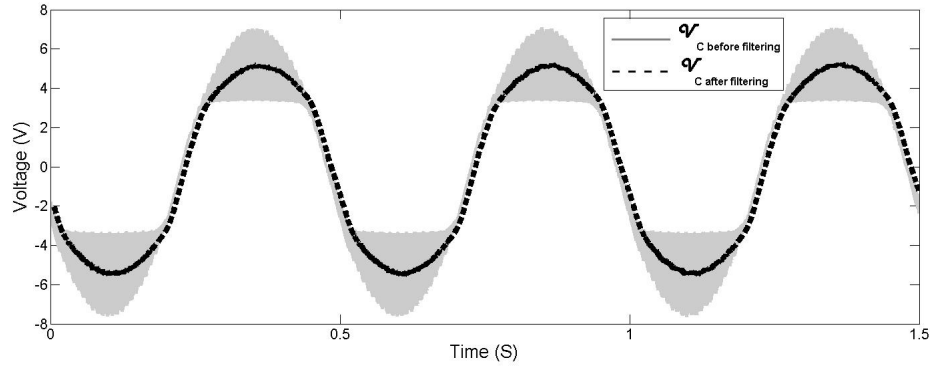


Figure 5.8:  $v_C$  before and after passing through a low-pass-filter.

Fig. 5.9 shows the results when a multi-frequency sinusoidal voltage is applied to the circuit which shows that  $v_C$  remains in phase with  $v_{in}$  regardless of frequency and amplitude of the input source. Thus the main concept of the circuit which is charging and discharging of  $C$  into the battery is validated for a multi-frequency voltage source. The voltage source used in this experiment is  $9.3\sin(2\pi)t + 7.3\sin(10\pi)t$ .

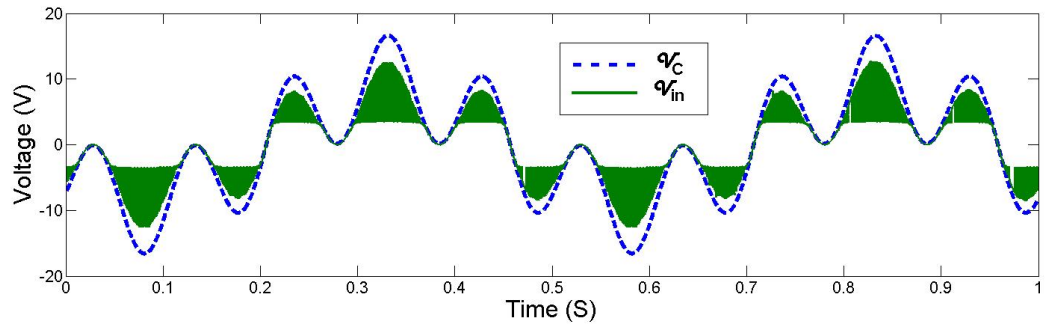


Figure 5.9: Capacitor voltage  $v_C$  and voltage source  $v_P$  for a multi-frequency excitation.

The next experiment was conducted to validate the resistive expression of the converter given by (3.25). Fig. 5.10 shows the theoretical and experimental values of  $R_{eq}$  of the converter at two different PWM frequencies. In this experiment,  $C_P = 7nF$  and  $V_{DC} = 3.5V$ . The goal of this circuit is to establish a resistive behavior at the input of the converter which can be used to match the resistance  $R_P$  with the input resistor of the converter  $R_{eq}$  for maximum power transfer and also achieve a unity power-factor battery charger.

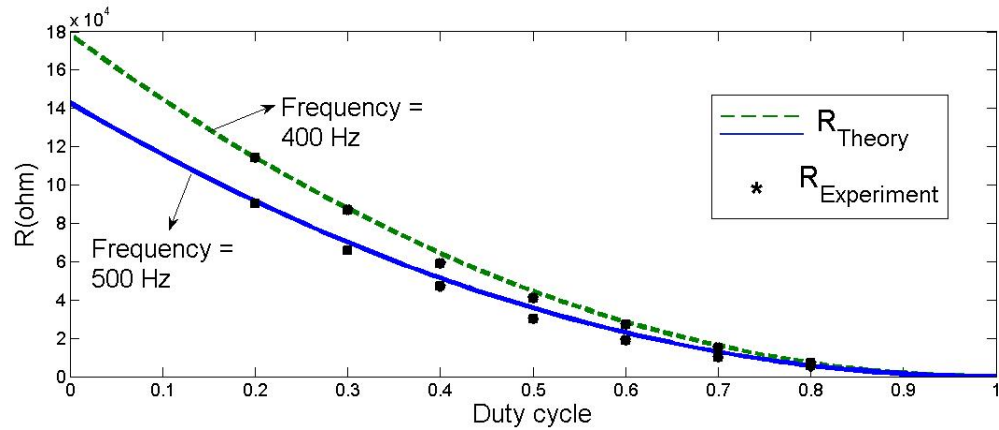


Figure 5.10: Input resistance of the buck converter circuit as a function of the duty cycle.

Fig. 5.11 illustrates performance of the PI feedback controller using the following numerical values  $R_P = 100k\Omega$ ,  $C = 1nF$ ,  $v_{in} = 8.5\sin(2\pi t)$ ,  $V_{DC} = 3.5V$ ,  $K_P = 9$ , and  $K_I = 18$ . As you can see in this figure, small parts of  $v_{R_{eq}}$  is equal to zero and at this point the two wave forms are not equal, the reason is that in these areas, the voltage across  $C$  is less than  $V_B + 2V_D$  and the diode bridge is off and this results in having zero volt across  $R_{eq}$ .

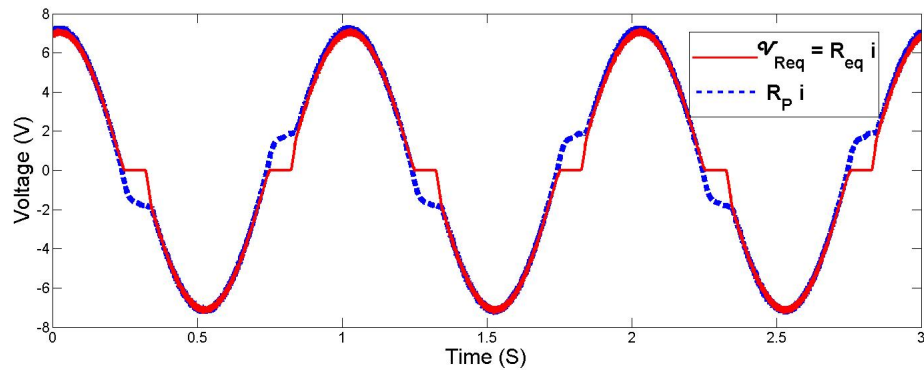


Figure 5.11:  $v_{R_{eq}}$  and  $R_P i$  for a single frequency voltage source.

Fig. 5.12 shows the waveforms  $v_{R_{eq}}$  and  $R_P i$  for a multi-frequency voltage source. In this experiment, the resistance between the input resistance of the circuit  $R_{eq}$  is matched with the source resistor  $R_P$  through feedback control. It should be noted that during the intervals when the diodes are off, the controller cannot achieve a resistive behavior due to the loss of

feedback loop. However, these intervals become small as the amplitude of the input waveform is increased, which is true for the case of a step down converter circuit used in this study.

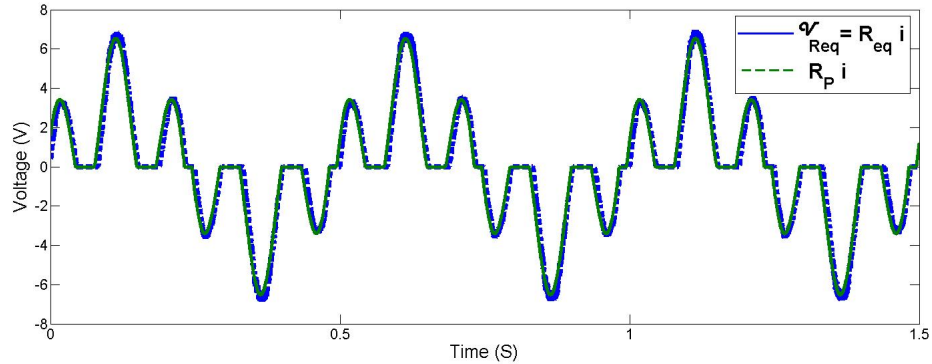


Figure 5.12:  $v_{Req}$  and  $R_p i$  for a multi-frequency voltage source.

## 5.2 Experimental Studies of the Proposed Converter using Feedback Controller

### 5.2.1 Circuit Implementation

In this experiment a vibrational piezoelectric transducer is used as the source to provide current to the circuit. The vibrational piezoelectric circuit model is shown in Fig 5.13. As this figure illustrates, a vibrational piezoelectric model consists of an ac current source in parallel with a capacitor and resistor. As Fig 5.14 shows, there is a capacitor at the input of this circuit. Thus in the case of using a vibrational piezoelectric transducer as the source for this circuit, we can replace  $C$  with the internal capacitor of the piezoelectric model represented by  $C_p$ . Fig. 5.15 shows the connection of piezoelectric transducer to the circuit by substituting  $C$  with  $C_p$ . In this experiment, the positive feedback driver circuit described in chapter 2 was used to drive the MOSFET gate.

The converter consists of an N-channel MOSFET switch (IRF540) [60] with low gate

charge for high frequency converters, four diodes (1N4148) [61], and two NiCd rechargeable batteries with high charging capacity (2650 mAH) [62]. The MOSFET operates at a PWM frequency of  $500Hz$  generated using the Matlab/Simulink environment, real-time interface of the dSPACE system and the positive feedback that was used to drive the MOSFET gate. An optocoupler (4N26) [63] with low rising and falling times and an NPN switching transistor (PN2222A) [64] were used to implement the positive feedback. As mentioned earlier, in this experiment a vibrational piezoelectric transducer is used as the harvestable source of energy and is connected to the converter.

A DC motor is used to generate vibrational excitation by using a signal generator and an amplifier. A flexible beam is attached to the DC motor at one side and clipped on the other side and a piezoelectric transducer is stucked on the flexible beam as shown in Fig. 5.16. The flexmorph piezoelectric has two layers of Lead Zirconate Titanate material bonded together [65]. The length of the piezoelectric is  $60mm$  and its width is  $25mm$ .

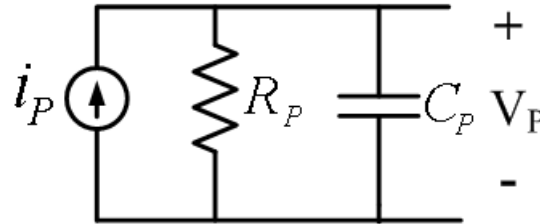


Figure 5.13: Piezoelectric transducer model.

Fig. 5.16 illustrates the experimental setup which consists of the DC motor, amplifier, signal generator, and the flexible beam to generate vibration, piezoelectric transducer that is stucked to the beam and the energy harvesting circuit.

## 5.2.2 Experimental Results

Fig. 5.17 shows the piezoelectric voltage and the voltage across the gate-source of the MOSFET  $V_{gate-source}$ . When the MOSFET is off, the voltage across the piezoelectric transducer increases because the internal capacitor of piezoelectric  $C_P$  is being charged. When  $V_{gate-source} > V_{Threshold}$ , the MOSFET turns on and the capacitor discharges to the battery, which continues until its voltage is equal to  $V_B + 2V_D + Ri(kT)$ . Fig. 5.18 illustrates

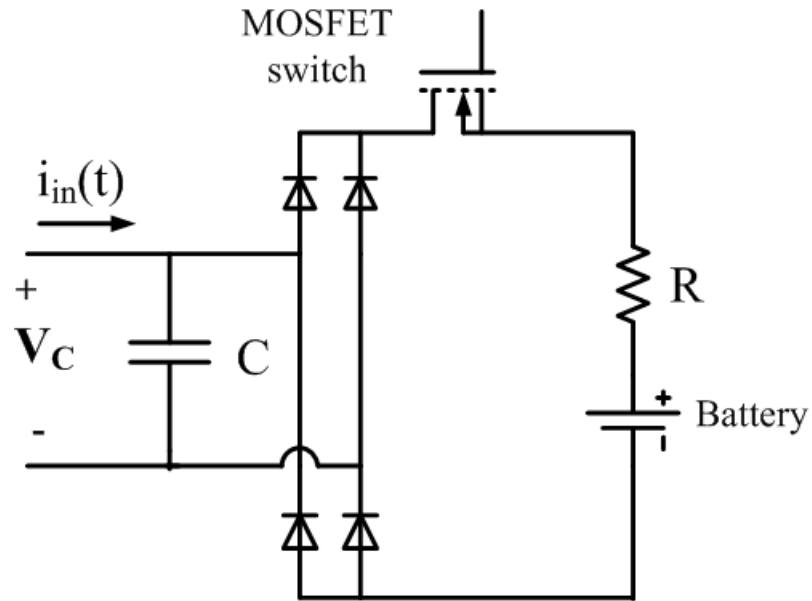


Figure 5.14: Power Electronics Circuit.

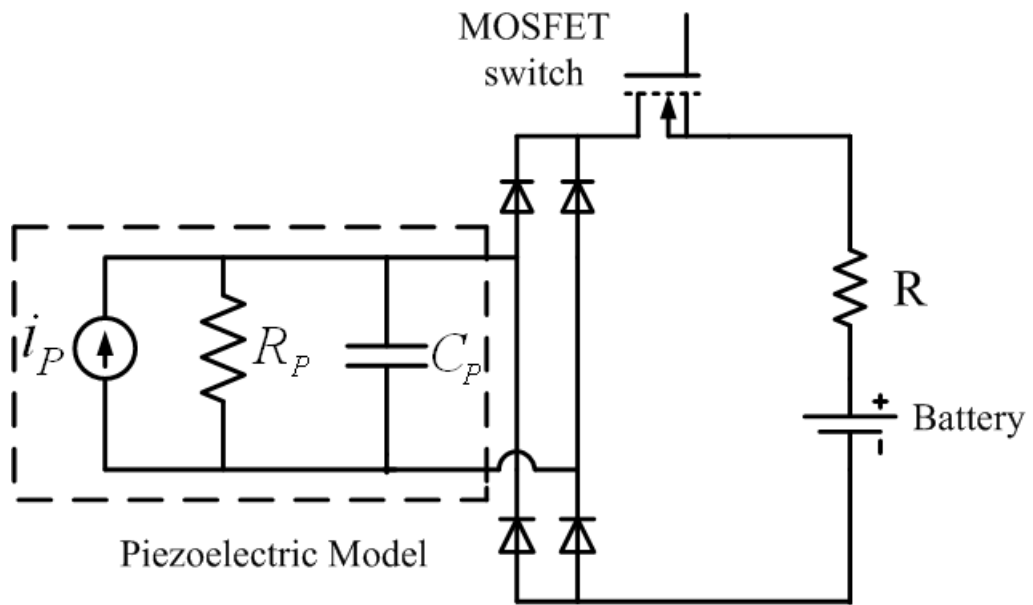


Figure 5.15: Connection of piezoelectric transducer model and the Power Electronics Circuit.

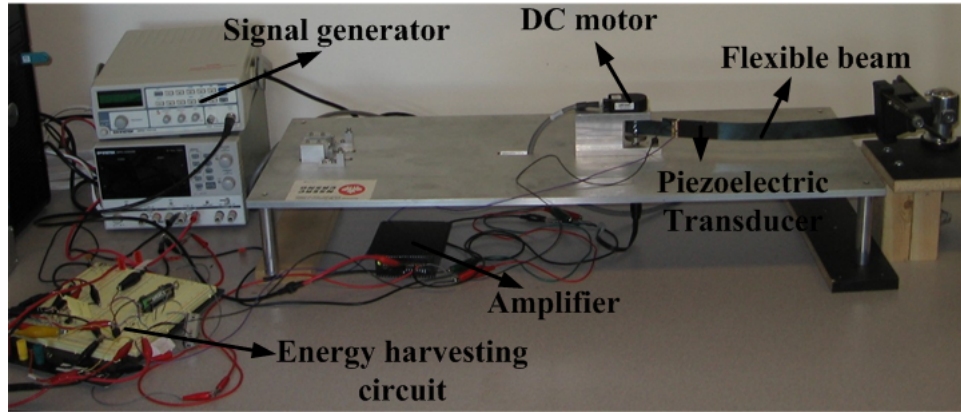


Figure 5.16: Experimental setup.

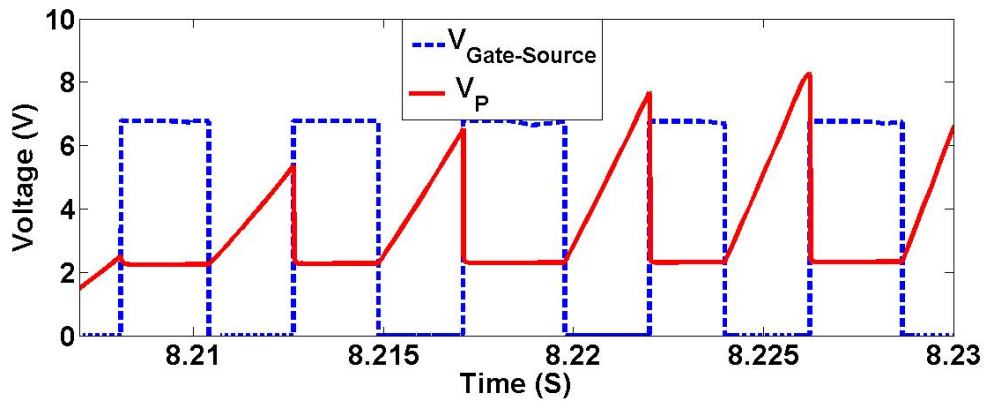


Figure 5.17: Charging of the piezoelectric capacitor  $C_P$  when MOSFET is off ( $V_{gate-source} < V_{Threshold}$ ) and discharging of the capacitor when MOSFET is on ( $V_{gate-source} > V_{Threshold}$ )

the piezoelectric voltage along with the averaged voltage shown by the dashed line and obtained by applying the switched signal to the low pass filter. In the next experiment,

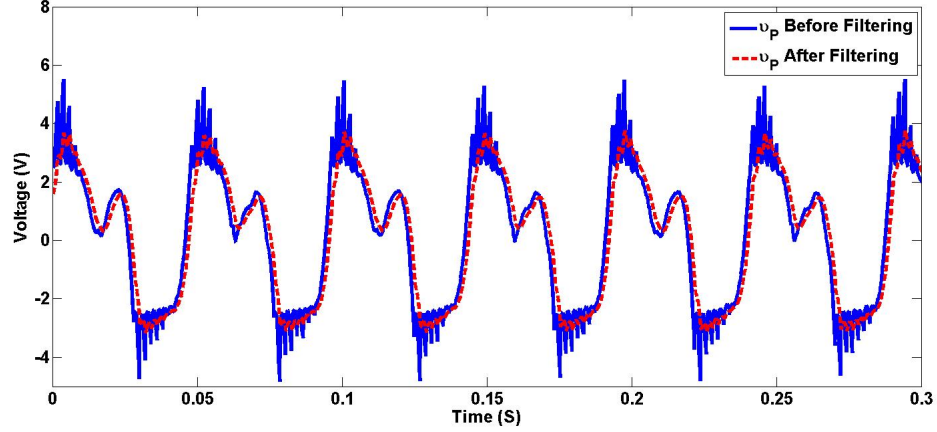


Figure 5.18: Piezoelectric voltage  $v_P$  before and after passing through a low-pass filter.

we validated the resistive expression at the input of the converter given (3.25). Fig. 5.19 shows the experimental values of  $R_{eq}$ . In this experiment the PWM frequency is  $500Hz$ . As mentioned earlier, the goal of this project is to achieve the resistive behavior at the input of the converter. Fig. 5.20 illustrates the voltage across the piezoelectric element  $v_P$  and piezoelectric current  $i_P(t)$ . As it can be seen from this figure, the piezoelectric voltage and current are in phase, which results in a unity power factor for multi-frequency vibrations. Thus we can get the best power conversion from the piezoelectric transducer due to the resistive input behavior of the converter. Identified by (3.25), the equivalent resistance of the energy harvesting circuit is a factor of the frequency and duty cycle of the PWM signal. In Chapter Two, it was shown that by applying a PI controller to the circuit, we can adjust the duty cycle of the switching to achieve the desired input resistance. In this experiment, we applied a PI controller to achieve the desired resistance of  $3000\Omega$  with the results are shown in Fig. (5.21). As mentioned earlier, to measure  $R_{eq}$ , we can use the following equation

$$R_{eq} = \frac{|v_P| - V_{DC}}{i_P(t)} \quad (5.1)$$

Fig. (5.21) indicates that the ratio of voltage divided by current as a result of applying the controller is equal to our desired resistance which is  $3000\Omega$ .

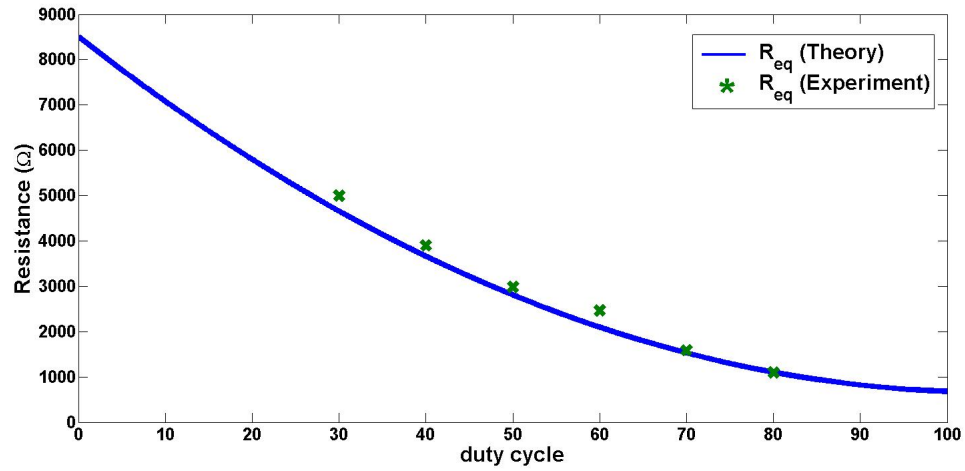


Figure 5.19: Input resistance of the buck converter circuit  $R_{eq}$  as a function of duty cycle of the PWM signal.

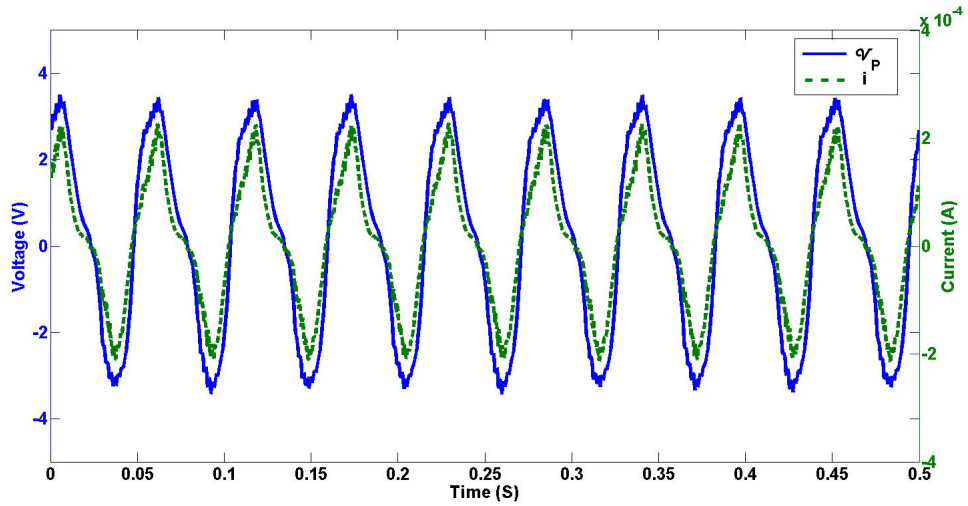


Figure 5.20: Voltage and current of the piezoelectric transducer.



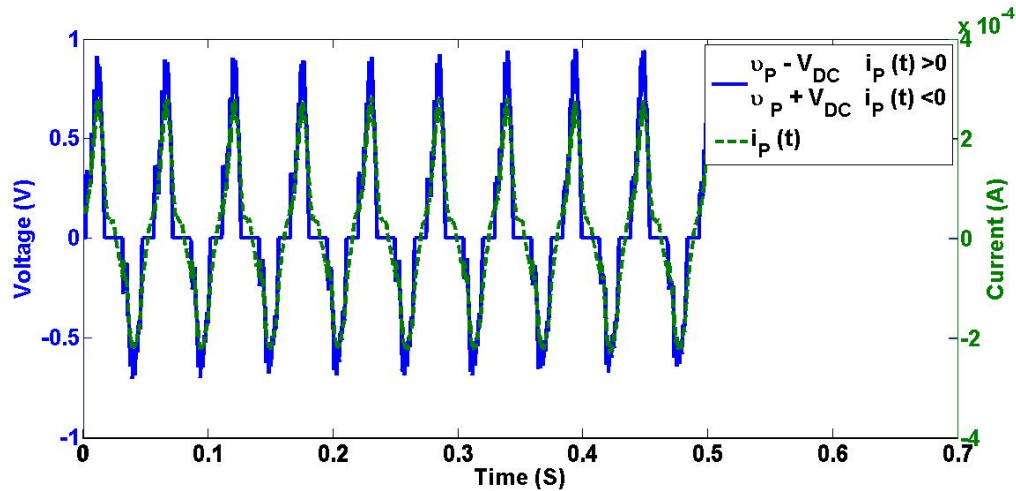


Figure 5.21: Converter wave-form in the feedback loop.

### 5.3 Experimental Studies of the Proposed Converter using Self-Powered Driven Circuit

The same setup used in previous section is utilized but different components are used to implement the circuit. Furthermore, the self-powered MOSFET gate drive circuit described in chapter 2 is used which is ultra low power consumption components.

#### 5.3.1 Circuit Implementation

In this experiment, four Schottky diodes with low forward voltage drop (*BAT43WS*) [66] were used to implement the diode bridge in the circuit. The circuit also consists of an N-channel MOSFET switch, a low threshold voltage MOSFET (*SI1563EDH*) [67] with low switching losses ( $r_{ds}$ ). In Fig. 3.21, the self-powered MOSFET gate drive consists of two opamps (*LT6004*) [68]. The opamp has a wide supply range 1.6V to 16V which is suitable for applications such as harvesting vibrational energy or solar energy in which the magnitude of input voltage source is not constant. Another advantage of this opamp is ultra low power consumption (Low Supply Current:  $1\mu\text{A}/\text{Amplifier Max}$ ).

### 5.3.2 Experimental Results

Several experiments were conducted to validate performance of the proposed converter. In the first experiment, we validated the operation of peak detector. As mentioned earlier, by adding peak detector to the circuit as shown in Fig. 5.22,  $C_S$  keeps track of the peak voltage of the source, store this value and use to drive the MOSFET. Fig. 5.23 shows the performance of the peak detector. As this figure indicates, the hold capacitor,  $C_S$  keeps the maximum amplitude of piezoelectric voltage, so that the voltage across the capacitor is almost entirely a DC voltage and this voltage can be used as the power supply for the opamp. Fig. 5.24 illustrates the voltage across the piezoelectric transducer along with the voltage across the gate-source of the MOSFET. When the voltage across the gate-source of the MOSFET is less than the threshold voltage of the MOSFET, the MOSFET is off and the current source in the piezoelectric model charges the internal capacitor of the piezoelectric, which results in increasing the voltage across the piezoelectric. On the other hand, when  $V_{Gate-Source} < V_{Threshold}$ , the MOSFET turns on and  $C_P$  discharges to the battery. In this experiment switching frequency is  $180Hz$  and the frequency of the signal generator that is connected to the DC motor to generate vibration is  $14Hz$ . The results of this experiment shows that, the peak detector keeps track of the peak voltage across the piezoelectric and this voltage can be used to power the opamps in the MOSFET gate drive circuit. Thus the proposed converter is self powered. Moreover, the generated PWM signal by the driven circuit can turn on and off the MOSFET switch. Therefore, the proposed energy harvesting and the driven circuit are self-powered and can be used to harvest vibrational energy using piezoelectric transducers. Further more, because of the resistive behavior of the circuit and the ultra low power consumption of the components, the efficiency of the circuit is good.

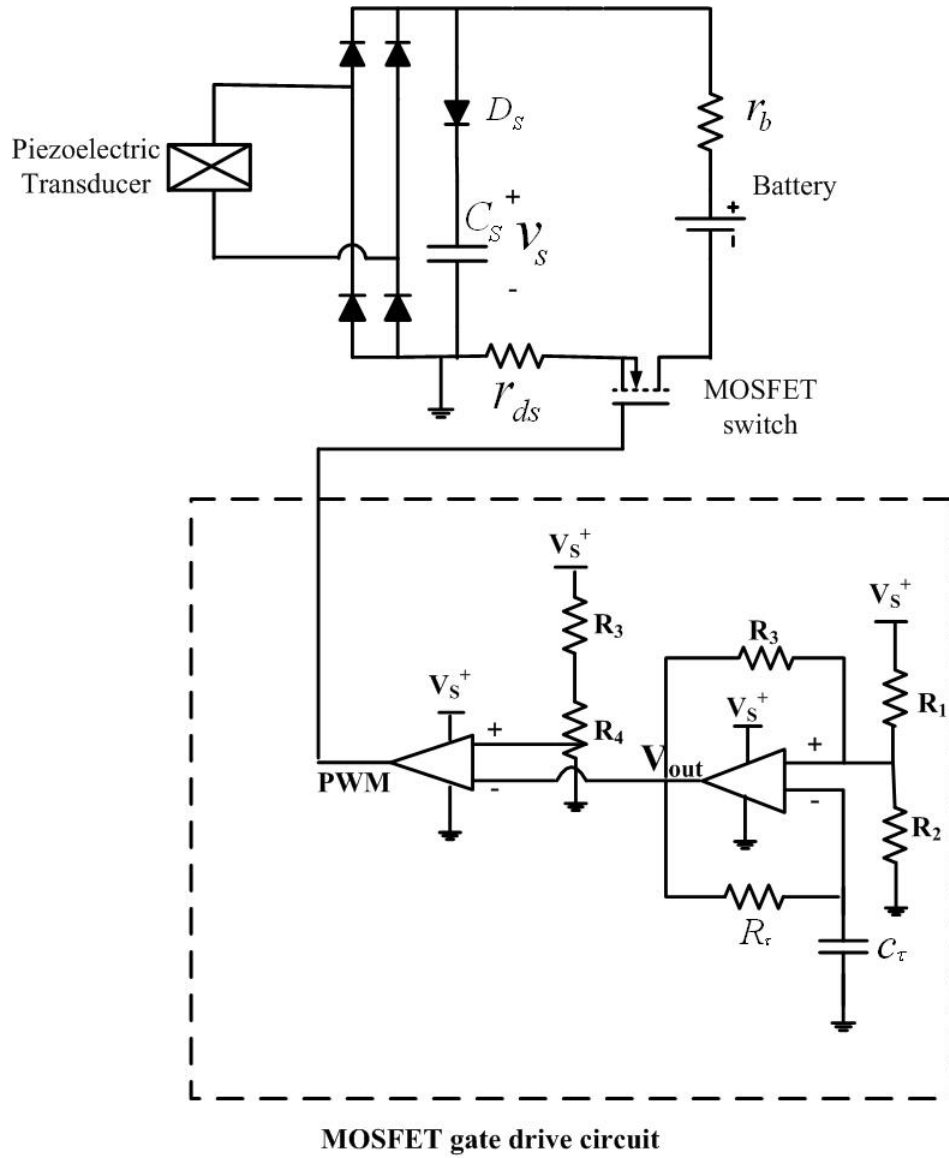


Figure 5.22: Piezoelectric transducer, the proposed converter, the peak detector and the MOSFET gate drive circuit.

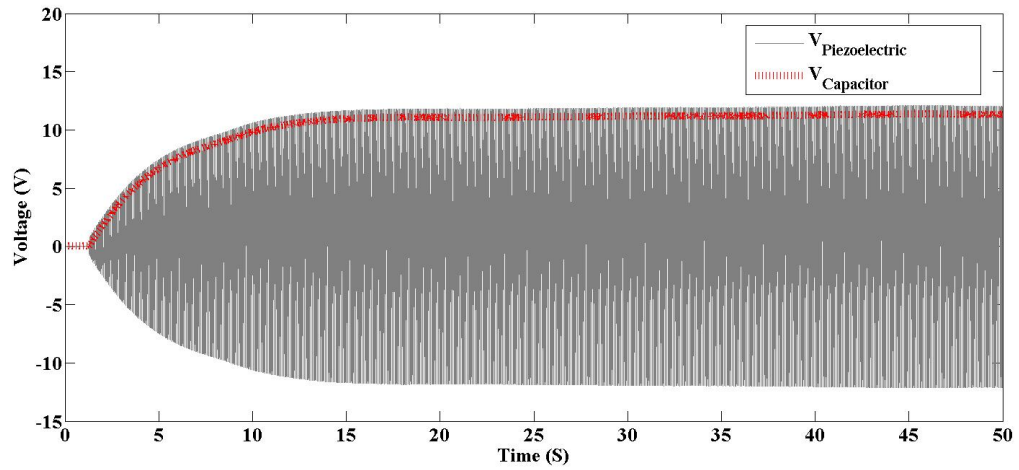


Figure 5.23: Voltage across the hold capacitor,  $C_S$  and the voltage across the piezoelectric transducer.

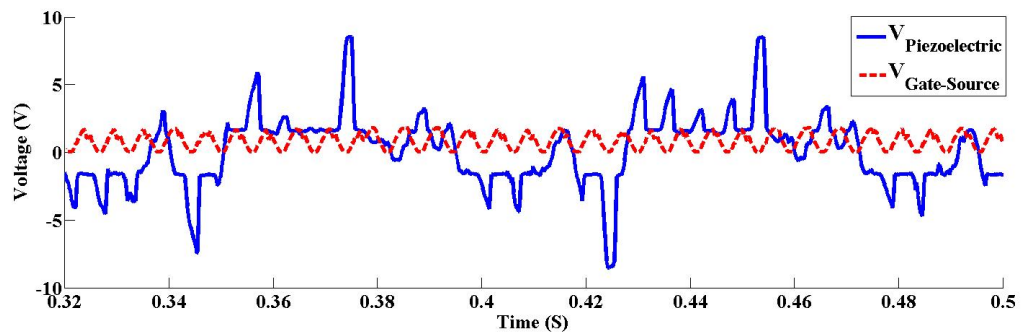


Figure 5.24: Voltage across the input of the buck converter  $v_{Req}$ , and voltage of piezoelectric resistor  $R_{pi}$  for a single frequency excitation.

## 5.4 Conclusion

In this chapter several experimental studies were conducted to verify the theoretical analysis of the circuit. In the first experiment, an independent voltage source was used as the source of energy. In the second and third experiments, a vibrational piezoelectric transducer was used as the source of energy. The experimental results reveals that, the input current and voltage of the converter are in phase, regardless of the amplitude or frequency off the input current to the converter that comes from the source.

The expression for input resistance of the converter given by (3.25) is validated as well in experiment.

To demonstrate the self-powered behavior of the converter and the ultra low power consumption of the elements in the circuit, a peak detector was added to the circuit. The results indicate that the circuit can work without any external power supply.

## Chapter 6

### Conclusions and Future Work

In this thesis, we propose a low-power electronics converter for energy harvesting applications. The proposed circuit consists of an ac/dc rectifier, a MOSFET switch, and a rechargeable battery as the storage element. It is shown that the converter in this work has resistive input behavior which is a function of frequency and duty cycle of the PWM switching. Thus, by applying a controller, the value of this resistance can be adjusted to a desired value. In addition, by adding a peak detector to the circuit, we could make the MOSFET gate drive circuit self-powered. Thus, the whole energy harvesting circuit would be self-powered and can work without any external power supply. To show an application of the proposed circuit in energy harvesting area and to prove the theoretical and simulation results, we used the mechanical vibration as the harvestable source of energy and a piezoelectric transducer for converting the applied strain into voltage. The vibrational piezoelectric transducer is then connected to the proposed converter. The behavior of the circuit was studied and the results were quite in agreement with the theoretical analysis.

We utilized a PI controller to control the input resistance of the circuit. To demonstrate the self-powered characteristic of the converter, a MOSFET gate driver circuit is implemented and tested. The achieved results confirm the correct behavior of the proposed circuit in terms of input resistive behavior and the self-powered characteristic.

From the experience gained during work, the following activities may be pursued as future work:

- Testing the proposed circuit using different types of piezoelectric transducers such as

PVDF, evaluating the behavior of the converter in each case and obtaining the amount of harvested power using different materials.

- Controlling the input resistance of the converter using a low power consumption micro controller and verifying the performance of the controller in real-time.
- Using the harvested power in the battery to run a low power consumption sensor and evaluate the operation of the energy harvesting circuit in an actual application.
- Using a natural source of vibrational energy such as a rail track or wooden stairs to demonstrate the performance of the converter in real applications.

## **Appendix A**

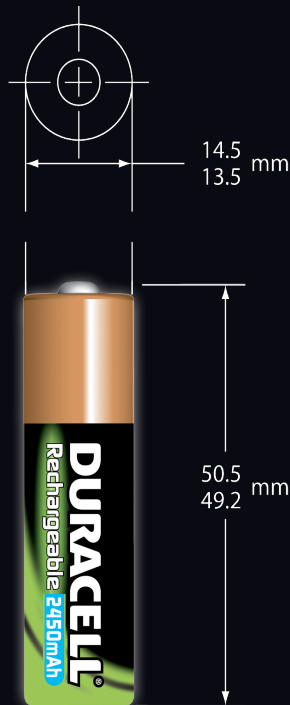
### **Duracell Rechargeable Battery**



# DURACELL® Rechargeable



## Rechargeable Supreme AA



Dimensions shown are IEC standards

Product can be charged on most NiMH or NiCd chargers utilizing standard dV, dV/dt, time and temperature dynamic charge termination methods. Duracell brand NiMH chargers are recommended for best results.

Delivered capacity is dependent on the applied load, operating temperature, and cut-off voltage. Please refer to the charts and discharge data shown for example of the energy/service life that the battery will provide for various local conditions.

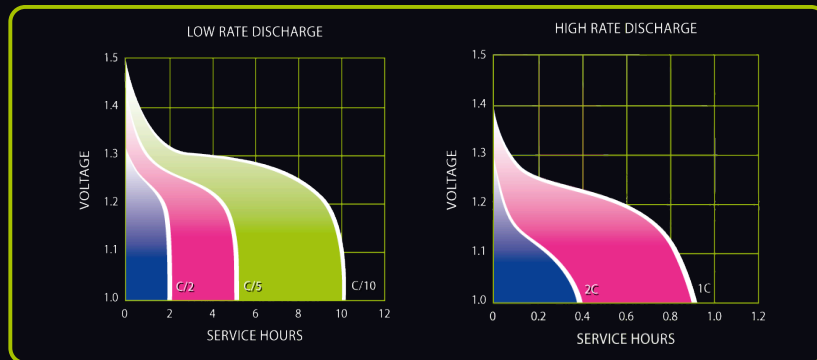
This data is subject to change. Performance information is typical. Contact Duracell for latest information.

### BENEFITS

- Recharge 100s of Times to Capture 1000s of Pictures
- Ideal for Digital and High Drain Devices

### TECHNICAL

Type:	NiMH AA 2450 mAh
Nominal Voltage	1.2V
Nominal Internal Impedance:	25 m-ohm @ 1kHz
Average Weight:	30.2 grams (1.07 ounces)
Volume	8.3 cm <sup>3</sup> (0.50 in <sup>3</sup> )
Operating Temperature Range:	-20° C to 50° C (-4° F to 122° F)
ANSI:	1.2H1
IEC:	HR6
Product Codes:	Blister x2 – EU/UK SAP Code: 75070715 EU/UK EAN Code: 5000394203679 Blister x4 – EU/UK SAP Code : 75070716 EU/UK EAN Code : 5000394203686

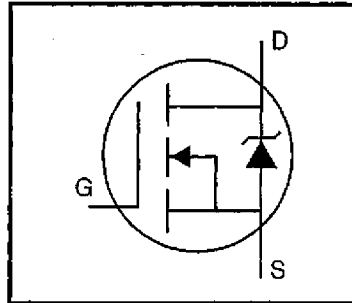


## **Appendix B**

### **Power MOSFET, (IRF540)**

## HEXFET® Power MOSFET

- Dynamic  $dv/dt$  Rating
- Repetitive Avalanche Rated
- 175°C Operating Temperature
- Fast Switching
- Ease of Paralleling
- Simple Drive Requirements



$$V_{DSS} = 100V$$

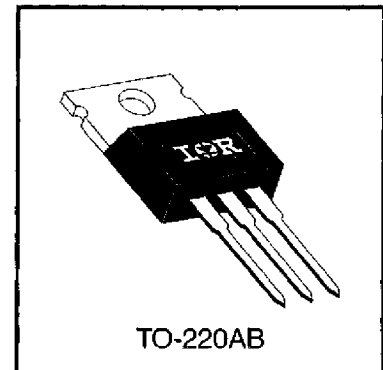
$$R_{DS(on)} = 0.077\Omega$$

$$I_D = 28A$$

### Description

Third Generation HEXFETs from International Rectifier provide the designer with the best combination of fast switching, ruggedized device design, low on-resistance and cost-effectiveness.

The TO-220 package is universally preferred for all commercial-industrial applications at power dissipation levels to approximately 50 watts. The low thermal resistance and low package cost of the TO-220 contribute to its wide acceptance throughout the industry.



DATA SHEETS

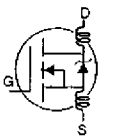
### Absolute Maximum Ratings

	Parameter	Max.	Units
$I_D @ T_C = 25^\circ C$	Continuous Drain Current, $V_{GS} @ 10 V$	28	A
$I_D @ T_C = 100^\circ C$	Continuous Drain Current, $V_{GS} @ 10 V$	20	
$I_{DM}$	Pulsed Drain Current ①	110	
$P_D @ T_C = 25^\circ C$	Power Dissipation	150	W
	Linear Derating Factor	1.0	W/°C
$V_{GS}$	Gate-to-Source Voltage	$\pm 20$	V
$E_{AS}$	Single Pulse Avalanche Energy ②	230	mJ
$I_{AR}$	Avalanche Current ①	28	A
$E_{AR}$	Repetitive Avalanche Energy ①	15	mJ
$dv/dt$	Peak Diode Recovery $dv/dt$ ③	5.5	V/ns
$T_J$ $T_{STG}$	Operating Junction and Storage Temperature Range	-55 to +175	°C
	Soldering Temperature, for 10 seconds	300 (1.6mm from case)	
	Mounting Torque, 6-32 or M3 screw	10 lbf•in (1.1 N•m)	

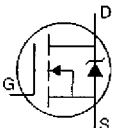
### Thermal Resistance

	Parameter	Min.	Typ.	Max.	Units
$R_{\theta JC}$	Junction-to-Case	—	—	1.0	°C/W
$R_{\theta CS}$	Case-to-Sink, Flat, Greased Surface	—	0.50	—	
$R_{\theta JA}$	Junction-to-Ambient	—	—	62	

## Electrical Characteristics @ $T_J = 25^\circ\text{C}$ (unless otherwise specified)

	Parameter	Min.	Typ.	Max.	Units	Test Conditions
$V_{(BR)DSS}$	Drain-to-Source Breakdown Voltage	100	—	—	V	$V_{GS}=0V, I_D=250\mu A$
$\Delta V_{(BR)DSS}/\Delta T_J$	Breakdown Voltage Temp. Coefficient	—	0.13	—	V/ $^\circ\text{C}$	Reference to $25^\circ\text{C}$ , $I_D=1\text{mA}$
$R_{DS(on)}$	Static Drain-to-Source On-Resistance	—	—	0.077	$\Omega$	$V_{GS}=10V, I_D=17A$ ④
$V_{GS(th)}$	Gate Threshold Voltage	2.0	—	4.0	V	$V_{DS}=V_{GS}, I_D=250\mu A$
$g_{fs}$	Forward Transconductance	8.7	—	—	S	$V_{DS}=50V, I_D=17A$ ④
$I_{DSS}$	Drain-to-Source Leakage Current	—	—	25	$\mu A$	$V_{DS}=100V, V_{GS}=0V$
		—	—	250		$V_{DS}=80V, V_{GS}=0V, T_J=150^\circ\text{C}$
$I_{GSS}$	Gate-to-Source Forward Leakage	—	—	100	nA	$V_{GS}=20V$
	Gate-to-Source Reverse Leakage	—	—	-100		$V_{GS}=-20V$
$Q_g$	Total Gate Charge	—	—	72	nC	$I_D=17A$
$Q_{gs}$	Gate-to-Source Charge	—	—	11		$V_{DS}=80V$
$Q_{gd}$	Gate-to-Drain ("Miller") Charge	—	—	32		$V_{GS}=10V$ See Fig. 6 and 13 ④
$t_{d(on)}$	Turn-On Delay Time	—	11	—	ns	$V_{DD}=50V$
$t_r$	Rise Time	—	44	—		$I_D=17A$
$t_{d(off)}$	Turn-Off Delay Time	—	53	—		$R_G=9.1\Omega$
$t_f$	Fall Time	—	43	—		$R_D=2.9\Omega$ See Figure 10 ④
$L_D$	Internal Drain Inductance	—	4.5	—	nH	Between lead, 6 mm (0.25in.) from package and center of die contact 
$L_S$	Internal Source Inductance	—	7.5	—		
$C_{iss}$	Input Capacitance	—	1700	—	pF	$V_{GS}=0V$
$C_{oss}$	Output Capacitance	—	560	—		$V_{DS}=25V$
$C_{rss}$	Reverse Transfer Capacitance	—	120	—		$f=1.0\text{MHz}$ See Figure 5

## Source-Drain Ratings and Characteristics

	Parameter	Min.	Typ.	Max.	Units	Test Conditions
$I_S$	Continuous Source Current (Body Diode)	—	—	28	A	MOSFET symbol showing the integral reverse p-n junction diode. 
$I_{SM}$	Pulsed Source Current (Body Diode) ①	—	—	110		
$V_{SD}$	Diode Forward Voltage	—	—	2.5	V	$T_J=25^\circ\text{C}, I_S=28A, V_{GS}=0V$ ④
$t_{rr}$	Reverse Recovery Time	—	180	360	ns	$T_J=25^\circ\text{C}, I_F=17A$
$Q_{rr}$	Reverse Recovery Charge	—	1.3	2.8	$\mu\text{C}$	$di/dt=100A/\mu\text{s}$ ④
$t_{on}$	Forward Turn-On Time	Intrinsic turn-on time is negligible (turn-on is dominated by $L_S+L_D$ )				

### Notes:

- ① Repetitive rating; pulse width limited by max. junction temperature (See Figure 11)
- ②  $V_{DD}=25V$ , starting  $T_J=25^\circ\text{C}$ ,  $L=440\mu\text{H}$ ,  $R_G=25\Omega$ ,  $I_{AS}=28A$  (See Figure 12)
- ③  $I_{SD}\leq 28A$ ,  $di/dt\leq 170A/\mu\text{s}$ ,  $V_{DD}\leq V_{(BR)DSS}$ ,  $T_J\leq 175^\circ\text{C}$
- ④ Pulse width  $\leq 300\mu\text{s}$ ; duty cycle  $\leq 2\%$ .

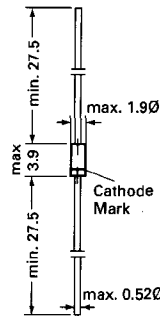
## **Appendix C**

### **Switching Diode (IN4148),**

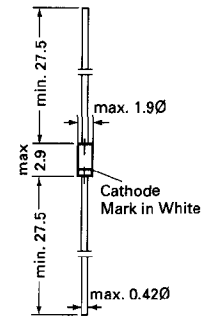
# 1N 4148 SILICON EPITAXIAL PLANAR DIODE

**Silicon Epitaxial Planar Diode**  
fast switching diode.

This diode is also available in MiniMELF case with the type designation LL4148.



Glass case JEDEC DO-35



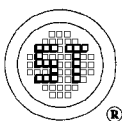
Glass case JEDEC DO-34

Dimensions in mm

## Absolute Maximum Ratings ( $T_a = 25\text{ }^\circ\text{C}$ )

	Symbol	Value	Unit
Reverse Voltage	$V_R$	75	V
Peak Reverse Voltage	$V_{RM}$	100	V
Rectified Current (Average) Half Wave Rectification with Resist. Load at $T_{amb} = 25\text{ }^\circ\text{C}$ and $f \geq 50\text{ Hz}$	$I_o$	150 <sup>1)</sup>	mA
Surge Forward Current at $t < 1\text{ s}$ and $T_j = 25\text{ }^\circ\text{C}$	$I_{FSM}$	500	mA
Power Dissipation at $T_{amb} = 25\text{ }^\circ\text{C}$	$P_{tot}$	500 <sup>1)</sup>	mW
Junction Temperature	$T_j$	200	$^\circ\text{C}$
Storage Temperature Range	$T_s$	-65 to + 200	$^\circ\text{C}$

<sup>1)</sup> Valid provided that leads at a distance of 8 mm from case are kept at ambient temperature



**SEMTECH ELECTRONICS LTD.**  
( wholly owned subsidiary of HONEY TECHNOLOGY LTD. )

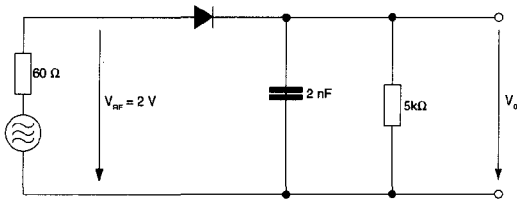


# 1N 4148 SILICON EPITAXIAL PLANAR DIODE

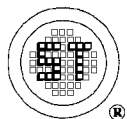
Characteristics at  $T_j = 25\text{ }^\circ\text{C}$

	Symbol	Min.	Typ.	Max.	Unit
Forward Voltage at $I_F = 10\text{ mA}$	$V_F$	-	-	1	V
Leakage Current at $V_R = 20\text{ V}$ at $V_R = 75\text{ V}$ at $V_R = 20\text{ V}, T_j = 150\text{ }^\circ\text{C}$	$I_R$ $I_R$ $I_R$	- - -	- - -	25 5 50	nA $\mu\text{A}$ $\mu\text{A}$
Reverse Breakdown Voltage tested with $100\text{ }\mu\text{A}$ Pulses	$V_{(BR)R}$	100	-	-	V
Capacitance at $V_F = V_R = 0$	$C_{tot}$	-	-	4	pF
Voltage Rise when Switching ON tested with $50\text{ mA}$ Forward Pulses $t_p = 0.1\text{ s}$ , Rise Time $< 30\text{ ns}$ , $f_p = 5$ to $100\text{ kHz}$	$V_{fr}$	-	-	2.5	V
Reverse Recovery Time from $I_F = 10\text{ mA}$ to $I_R = 1\text{ mA}$ , $V_R = 6\text{ V}$ , $R_L = 100\text{ }\Omega$ ,	$t_{rr}$	-	-	4	ns
Thermal Resistance Junction to Ambient Air	$R_{thA}$	-	-	0.35 <sup>1)</sup>	K/mW
Rectification Efficiency at $f = 100\text{ MHz}$ , $V_{RF} = 2\text{ V}$	$\eta_V$	0.45	-	-	-

<sup>1)</sup> Valid provided that leads at a distance of 8 mm from case are kept at ambient temperature



Rectification Efficiency Measurement Circuit



**SEMTECH ELECTRONICS LTD.**  
( wholly owned subsidiary of HONEY TECHNOLOGY LTD. )

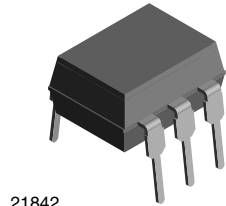


## **Appendix D**

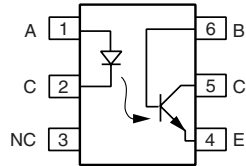
### **Optocoupler (4N26),**



## Optocoupler, Phototransistor Output, with Base Connection



21842



i179004-5

### DESCRIPTION

The 4N25 family is an industry standard single channel phototransistor coupler. This family includes the 4N25, 4N26, 4N27, 4N28. Each optocoupler consists of gallium arsenide infrared LED and a silicon NPN phototransistor.

### FEATURES

- Isolation test voltage 5000 V<sub>RMS</sub>
- Interfaces with common logic families
- Input-output coupling capacitance < 0.5 pF
- Industry standard dual-in-line 6 pin package
- Compliant to RoHS directive 2002/95/EC and in accordance to WEEE 2002/96/EC



RoHS COMPLIANT

### APPLICATIONS

- AC mains detection
- Reed relay driving
- Switch mode power supply feedback
- Telephone ring detection
- Logic ground isolation
- Logic coupling with high frequency noise rejection

### AGENCY APPROVALS

- UL1577, file no. E52744
- BSI: EN 60065:2002, EN 60950:2000
- FIMKO: EN 60950, EN 60065, EN 60335

ORDER INFORMATION	
PART	REMARKS
4N25	CTR > 20 %, DIP-6
4N26	CTR > 20 %, DIP-6
4N27	CTR > 10 %, DIP-6
4N28	CTR > 10 %, DIP-6

ABSOLUTE MAXIMUM RATINGS (1)				
PARAMETER	TEST CONDITION	SYMBOL	VALUE	UNIT
<b>INPUT</b>				
Reverse voltage		V <sub>R</sub>	5	V
Forward current		I <sub>F</sub>	60	mA
Surge current	t ≤ 10 μs	I <sub>FSM</sub>	3	A
Power dissipation		P <sub>diss</sub>	100	mW
<b>OUTPUT</b>				
Collector emitter breakdown voltage		V <sub>CEO</sub>	70	V
Emitter base breakdown voltage		V <sub>EBO</sub>	7	V
Collector current		I <sub>C</sub>	50	mA
	t ≤ 1 ms	I <sub>C</sub>	100	mA
Power dissipation		P <sub>diss</sub>	150	mW



<b>ABSOLUTE MAXIMUM RATINGS (1)</b>				
PARAMETER	TEST CONDITION	SYMBOL	VALUE	UNIT
<b>COUPLER</b>				
Isolation test voltage		$V_{ISO}$	5000	$V_{RMS}$
Creepage distance			$\geq 7$	mm
Clearance distance			$\geq 7$	mm
Isolation thickness between emitter and detector			$\geq 0.4$	mm
Comparative tracking index	DIN IEC 112/VDE 0303, part 1		175	
Isolation resistance	$V_{IO} = 500\text{ V}, T_{amb} = 25\text{ }^\circ\text{C}$	$R_{IO}$	$10^{12}$	$\Omega$
	$V_{IO} = 500\text{ V}, T_{amb} = 100\text{ }^\circ\text{C}$	$R_{IO}$	$10^{11}$	$\Omega$
Storage temperature		$T_{stg}$	- 55 to + 125	$^\circ\text{C}$
Operating temperature		$T_{amb}$	- 55 to + 100	$^\circ\text{C}$
Junction temperature		$T_j$	125	$^\circ\text{C}$
Soldering temperature (2)	max. 10 s dip soldering: distance to seating plane $\geq 1.5\text{ mm}$	$T_{slid}$	260	$^\circ\text{C}$

**Notes**(1)  $T_{amb} = 25\text{ }^\circ\text{C}$ , unless otherwise specified.

Stresses in excess of the absolute maximum ratings can cause permanent damage to the device. Functional operation of the device is not implied at these or any other conditions in excess of those given in the operational sections of this document. Exposure to absolute maximum ratings for extended periods of the time can adversely affect reliability.

(2) Refer to reflow profile for soldering conditions for surface mounted devices (SMD). Refer to wave profile for soldering conditions for through hole devices (DIP).

<b>ELECTRICAL CHARACTERISTICS (1)</b>							
PARAMETER	TEST CONDITION	PART	SYMBOL	MIN.	TYP.	MAX.	UNIT
<b>INPUT</b>							
Forward voltage (2)	$I_F = 50\text{ mA}$		$V_F$		1.3	1.5	V
Reverse current (2)	$V_R = 3\text{ V}$		$I_R$		0.1	100	$\mu\text{A}$
Capacitance	$V_R = 0\text{ V}$		$C_O$		25		pF
<b>OUTPUT</b>							
Collector base breakdown voltage (2)	$I_C = 100\text{ }\mu\text{A}$		$BV_{CBO}$	70			V
Collector emitter breakdown voltage (2)	$I_C = 1\text{ mA}$		$BV_{CEO}$	30			V
Emitter collector breakdown voltage (2)	$I_E = 100\text{ }\mu\text{A}$		$BV_{ECO}$	7			V
$I_{CEO}(\text{dark})$ (2)	$V_{CE} = 10\text{ V}, (\text{base open})$	4N25			5	50	nA
		4N26			5	50	nA
		4N27			5	50	nA
		4N28			10	100	nA
$I_{CBO}(\text{dark})$ (2)	$V_{CB} = 10\text{ V}, (\text{emitter open})$				2	20	nA
Collector emitter capacitance	$V_{CE} = 0$		$C_{CE}$		6		pF
<b>COUPLER</b>							
Isolation test voltage (2)	Peak, 60 Hz		$V_{IO}$	5000			V
Saturation voltage, collector emitter	$I_{CE} = 2\text{ mA}, I_F = 50\text{ mA}$		$V_{CE(\text{sat})}$			0.5	V
Resistance, input output (2)	$V_{IO} = 500\text{ V}$		$R_{IO}$	100			$G\Omega$
Capacitance, input output	$f = 1\text{ MHz}$		$C_{IO}$		0.6		pF

**Notes**(1)  $T_{amb} = 25\text{ }^\circ\text{C}$ , unless otherwise specified.

Minimum and maximum values are testing requirements. Typical values are characteristics of the device and are the result of engineering evaluation. Typical values are for information only and are not part of the testing requirements.

(2) JEDEC registered values are 2500 V, 1500 V, 1500 V, and 500 V for the 4N25, 4N26, 4N27, and 4N28 respectively.

## **Appendix E**

### **NPN Switching Transistor (PN2222A)**

# NPN switching transistor

# PN2222A

### FEATURES

- High current (max. 600 mA)
- Low voltage (max. 40 V).

### APPLICATIONS

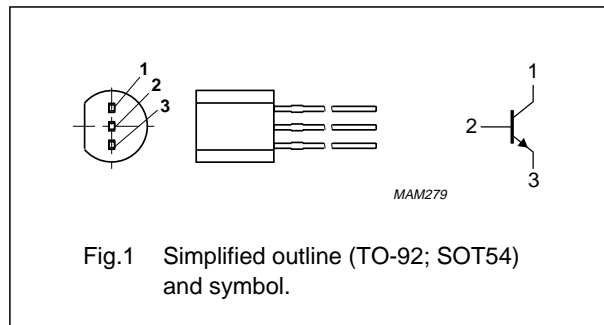
- General purpose switching and linear amplification.

### DESCRIPTION

NPN switching transistor in a TO-92; SOT54 plastic package. PNP complement: PN2907A.

### PINNING

PIN	DESCRIPTION
1	collector
2	base
3	emitter



### LIMITING VALUES

In accordance with the Absolute Maximum Rating System (IEC 134).

SYMBOL	PARAMETER	CONDITIONS	MIN.	MAX.	UNIT
$V_{CBO}$	collector-base voltage	open emitter	–	75	V
$V_{CEO}$	collector-emitter voltage	open base	–	40	V
$V_{EBO}$	emitter-base voltage	open collector	–	6	V
$I_C$	collector current (DC)		–	600	mA
$I_{CM}$	peak collector current		–	800	mA
$I_{BM}$	peak base current		–	200	mA
$P_{tot}$	total power dissipation	$T_{amb} \leq 25\text{ }^\circ\text{C}$	–	500	mW
$T_{stg}$	storage temperature		–65	+150	$^\circ\text{C}$
$T_j$	junction temperature		–	150	$^\circ\text{C}$
$T_{amb}$	operating ambient temperature		–65	+150	$^\circ\text{C}$

## NPN switching transistor

PN2222A

## THERMAL CHARACTERISTICS

SYMBOL	PARAMETER	CONDITIONS	VALUE	UNIT
$R_{th\ j-a}$	thermal resistance from junction to ambient	note 1	250	K/W

## Note

1. Transistor mounted on an FR4 printed-circuit board.

## CHARACTERISTICS

$T_j = 25\text{ °C}$  unless otherwise specified.

SYMBOL	PARAMETER	CONDITIONS	MIN.	MAX.	UNIT
$I_{CBO}$	collector cut-off current	$I_E = 0; V_{CB} = 60\text{ V}$	–	10	nA
		$I_E = 0; V_{CB} = 60\text{ V}; T_{amb} = 125\text{ °C}$	–	10	$\mu\text{A}$
$I_{EBO}$	emitter cut-off current	$I_C = 0; V_{EB} = 3\text{ V}$	–	10	nA
$h_{FE}$	DC current gain	$I_C = 0.1\text{ mA}; V_{CE} = 10\text{ V}$	35	–	
		$I_C = 1\text{ mA}; V_{CE} = 10\text{ V}$	50	–	
		$I_C = 10\text{ mA}; V_{CE} = 10\text{ V}$	75	–	
		$I_C = 10\text{ mA}; V_{CE} = 10\text{ V}; T_{amb} = -55\text{ °C}$	35	–	
		$I_C = 150\text{ mA}; V_{CE} = 1\text{ V}$	50	–	
		$I_C = 150\text{ mA}; V_{CE} = 10\text{ V}$	100	300	
$V_{CEsat}$	collector-emitter saturation voltage	$I_C = 150\text{ mA}; I_B = 15\text{ mA}$	–	300	mV
		$I_C = 500\text{ mA}; I_B = 50\text{ mA}$	1	–	V
$V_{BEsat}$	base-emitter saturation voltage	$I_C = 150\text{ mA}; I_B = 15\text{ mA}$	0.6	1.2	V
		$I_C = 500\text{ mA}; I_B = 50\text{ mA}$	–	2	V
$C_c$	collector capacitance	$I_E = i_e = 0; V_{CB} = 10\text{ V}; f = 1\text{ MHz}$	–	8	pF
$C_e$	emitter capacitance	$I_C = i_c = 0; V_{EB} = 500\text{ mV}; f = 1\text{ MHz}$	–	25	pF
$f_T$	transition frequency	$I_C = 20\text{ mA}; V_{CE} = 20\text{ V}; f = 100\text{ MHz}$	300	–	MHz
F	noise figure	$I_C = 100\text{ }\mu\text{A}; V_{CE} = 5\text{ V}; R_S = 1\text{ k}\Omega;$ $f = 1\text{ kHz}$	–	4	dB

## Switching times (between 10% and 90% levels); see Fig.2

$t_{on}$	turn-on time	$I_{Con} = 150\text{ mA}; I_{Bon} = 15\text{ mA};$ $I_{Boff} = -15\text{ mA}; T_{amb} = 25\text{ °C}$	–	35	ns
$t_d$	delay time		–	15	ns
$t_r$	rise time		–	20	ns
$t_{off}$	turn-off time		–	250	ns
$t_s$	storage time		–	200	ns
$t_f$	fall time		–	60	ns

## **Appendix F**

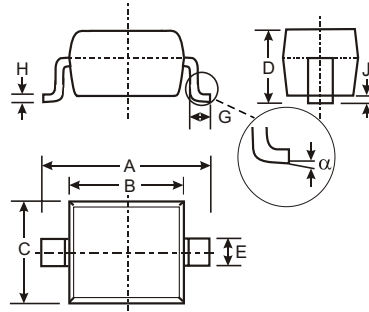
### **Surface Mount Schottkey Barrier Diode (BAT43WS)**

### Features

- Low Forward Voltage Drop
- Fast Switching
- Ultra-Small Surface Mount Package
- Also Available in Lead Free Version

### Mechanical Data

- Case: SOD-323, Plastic
- Case material - UL Flammability Rating Classification 94V-0
- Moisture sensitivity: Level 1 per J-STD-020A
- Leads: Solderable per MIL-STD-202, Method 208
- Also Available in Lead Free Plating (Matte Tin Finish). Please see Ordering Information, Note 4, on Page 2
- BAT42WS Marking: S7
- BAT43WS Marking: S8
- Polarity: Cathode Band
- Weight: 0.004 grams (approx.)



SOD-323		
Dim	Min	Max
A	2.30	2.70
B	1.60	1.80
C	1.20	1.40
D	1.05 Typical	
E	0.25	0.35
G	0.20	0.40
H	0.10	0.15
J	0.05 Typical	
$\alpha$	0°	8°
All Dimensions in mm		

### Maximum Ratings @ $T_A = 25^\circ\text{C}$ unless otherwise specified

Characteristic	Symbol	BAT42WS / BAT43WS	Unit
Peak Repetitive Reverse Voltage Working Peak Reverse Voltage DC Blocking Voltage	$V_{RRM}$ $V_{RWM}$ $V_R$	30	V
RMS Reverse Voltage	$V_{R(RMS)}$	21	V
Forward Continuous Current (Note 1)	$I_{FM}$	200	mA
Repetitive Peak Forward Current (Note 1) @ $t < 1.0\text{s}$	$I_{FRM}$	500	mA
Non-Repetitive Peak Forward Surge Current @ $t < 10\text{ms}$	$I_{FSM}$	4.0	A
Power Dissipation (Note 1)	$P_d$	200	mW
Thermal Resistance Junction to Ambient Air (Note 1)	$R_{\theta JA}$	625	$^\circ\text{C/W}$
Operating and Storage Temperature Range	$T_j, T_{STG}$	-55 to +125	$^\circ\text{C}$

### Electrical Characteristics @ $T_A = 25^\circ\text{C}$ unless otherwise specified

Characteristic	Symbol	Min	Max	Unit	Test Condition
Reverse Breakdown Voltage (Note 2)	$V_{(BR)R}$	30	—	V	$I_R = 100\mu\text{A}$
Forward Voltage Drop (Note 2)	$V_F$	—	1.0 0.40 0.65 0.33 0.45	V	$I_F = 200\text{mA}$ $I_F = 10\text{mA}$ $I_F = 50\text{mA}$ $I_F = 2.0\text{mA}$ $I_F = 15\text{mA}$
Reverse Current (Note 2)	$I_R$	—	500 100	nA $\mu\text{A}$	$V_R = 25\text{V}$ $V_R = 25\text{V}, T_j = 100^\circ\text{C}$
Total Capacitance	$C_T$	—	10	pF	$V_R = 1.0, f = 1.0\text{MHz}$
Reverse Recovery Time	$t_{rr}$	—	5.0	ns	$I_F = I_R = 10\text{mA}$ , $I_{rr} = 0.1 \times I_R, R_L = 100\Omega$

- Notes:
1. Part mounted on FR4 PC Board with recommended pad layout, which can be found on our website at <http://www.diodes.com/datasheets/ap02001.pdf>.
  2. Short duration test pulse used to minimize self-heating effect.

## **Appendix G**

### **Low Threshold Voltage (SI1563EDH)**





# Complementary 20-V (D-S) Low-Threshold MOSFET

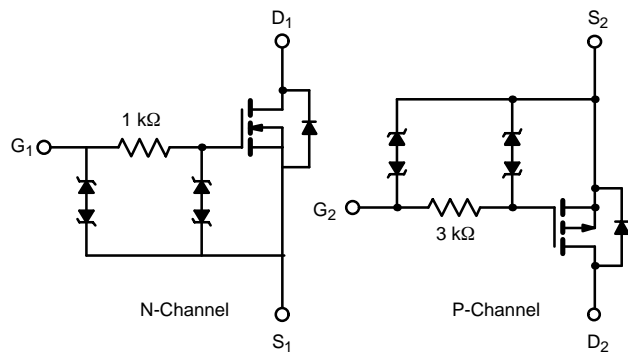
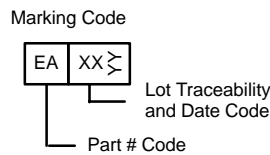
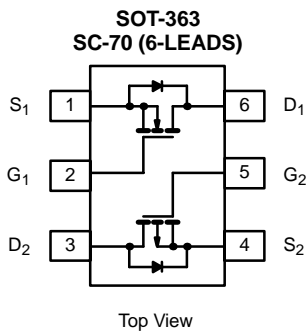
PRODUCT SUMMARY			
	V <sub>DS</sub> (V)	r <sub>DS(on)</sub> (Ω)	I <sub>D</sub> (A)
N-Channel	20	0.280 @ V <sub>GS</sub> = 4.5 V	1.28
		0.360 @ V <sub>GS</sub> = 2.5 V	1.13
		0.450 @ V <sub>GS</sub> = 1.8 V	1.00
P-Channel	-20	0.490 @ V <sub>GS</sub> = -4.5 V	-1.00
		0.750 @ V <sub>GS</sub> = -2.5 V	-0.81
		1.10 @ V <sub>GS</sub> = -1.8 V	-0.67

## FEATURES

- TrenchFET® Power MOSFETS: 1.8-V Rated
- ESD Protected: 2000 V
- Thermally Enhanced SC-70 Package

## APPLICATIONS

- Load Switching
- PA Switch
- Level Switch



ABSOLUTE MAXIMUM RATINGS (T <sub>A</sub> = 25 °C UNLESS OTHERWISE NOTED)							
Parameter	Symbol	N-Channel		P-Channel		Unit	
		5 secs	Steady State	5 secs	Steady State		
Drain-Source Voltage	V <sub>DS</sub>	20		-20		V	
Gate-Source Voltage	V <sub>GS</sub>	±12		±12		V	
Continuous Drain Current (T <sub>J</sub> = 150 °C) <sup>a</sup>	I <sub>D</sub>	T <sub>A</sub> = 25 °C	1.28	1.13	-1.00	-0.88	A
		T <sub>A</sub> = 85 °C	0.92	0.81	-0.72	-0.63	
Pulsed Drain Current	I <sub>DM</sub>	4.0		-3.0		A	
Continuous Source Current (Diode Conduction) <sup>a</sup>	I <sub>S</sub>	0.61	0.48	-0.61	-0.48	A	
Maximum Power Dissipation <sup>a</sup>	P <sub>D</sub>	T <sub>A</sub> = 25 °C	0.74	0.57	0.30	0.57	W
		T <sub>A</sub> = 85 °C	0.38	0.30	0.16	0.3	
Operating Junction and Storage Temperature Range	T <sub>J</sub> , T <sub>stg</sub>	-55 to 150				°C	

THERMAL RESISTANCE RATINGS					
Parameter		Symbol	Typical	Maximum	Unit
Maximum Junction-to-Ambient <sup>a</sup>	t ≤ 5 sec	R <sub>thJA</sub>	130	170	°C/W
	Steady State		170	220	
Maximum Junction-to-Foot (Drain)	Steady State	R <sub>thJF</sub>	80	100	

Notes

a. Surface Mounted on 1" x 1" FR4 Board.

SPECIFICATIONS (T <sub>J</sub> = 25 °C UNLESS OTHERWISE NOTED)							
Parameter	Symbol	Test Condition		Min	Typ	Max	Unit
<b>Static</b>							
Gate Threshold Voltage	V <sub>GS(th)</sub>	V <sub>DS</sub> = V <sub>GS</sub> , I <sub>D</sub> = 100 μA	N-Ch	0.45			V
		V <sub>DS</sub> = V <sub>GS</sub> , I <sub>D</sub> = -100 μA	P-Ch	-0.45			
Gate-Body Leakage	I <sub>GSS</sub>	V <sub>DS</sub> = 0 V, V <sub>GS</sub> = ±4.5 V	N-Ch			±1	μA
			P-Ch			±1	
		V <sub>DS</sub> = 0 V, V <sub>GS</sub> = ±12 V	N-Ch			±10	mA
			P-Ch			±10	
Zero Gate Voltage Drain Current	I <sub>DSS</sub>	V <sub>DS</sub> = 16 V, V <sub>GS</sub> = 0 V	N-Ch			1	μA
		V <sub>DS</sub> = -16 V, V <sub>GS</sub> = 0 V	P-Ch			-1	
		V <sub>DS</sub> = 16 V, V <sub>GS</sub> = 0 V, T <sub>J</sub> = 85 °C	N-Ch			5	
		V <sub>DS</sub> = -16 V, V <sub>GS</sub> = 0 V, T <sub>J</sub> = 85 °C	P-Ch			-5	
On-State Drain Current <sup>a</sup>	I <sub>D(on)</sub>	V <sub>DS</sub> ≥ 5 V, V <sub>GS</sub> = 4.5 V	N-Ch	2			A
		V <sub>DS</sub> ≤ -5 V, V <sub>GS</sub> = -4.5 V	P-Ch	-2			
Drain-Source On-State Resistance <sup>a</sup>	r <sub>DS(on)</sub>	V <sub>GS</sub> = 4.5 V, I <sub>D</sub> = 1.13 A	N-Ch		0.220	0.280	Ω
		V <sub>GS</sub> = -4.5 V, I <sub>D</sub> = -0.88 A	P-Ch		0.400	0.490	
		V <sub>GS</sub> = 2.5 V, I <sub>D</sub> = 0.99 A	N-Ch		0.281	0.360	
		V <sub>GS</sub> = -2.5 V, I <sub>D</sub> = -0.71 A	P-Ch		0.610	0.750	
		V <sub>GS</sub> = 1.8 V, I <sub>D</sub> = 0.20 A	N-Ch		0.344	0.450	
		V <sub>GS</sub> = -1.8 V, I <sub>D</sub> = -0.20 A	P-Ch		0.850	1.10	
Forward Transconductance <sup>a</sup>	g <sub>fs</sub>	V <sub>DS</sub> = 10 V, I <sub>D</sub> = 1.13 A	N-Ch		2.6		S
		V <sub>DS</sub> = -10 V, I <sub>D</sub> = -0.88 A	P-Ch		1.5		
Diode Forward Voltage <sup>a</sup>	V <sub>SD</sub>	I <sub>S</sub> = 0.48 A, V <sub>GS</sub> = 0 V	N-Ch		0.8	1.2	V
		I <sub>S</sub> = -0.48 A, V <sub>GS</sub> = 0 V	P-Ch		-0.8	-1.2	
<b>Dynamic<sup>b</sup></b>							
Total Gate Charge	Q <sub>g</sub>	<b>N-Channel</b> V <sub>DS</sub> = 10 V, V <sub>GS</sub> = 4.5 V, I <sub>D</sub> = 1.13 A <b>P-Channel</b> V <sub>DS</sub> = -10 V, V <sub>GS</sub> = -4.5 V, I <sub>D</sub> = -0.88 A	N-Ch		0.65	1.0	nC
Gate-Source Charge	Q <sub>gs</sub>		N-Ch		0.2		
			P-Ch		0.3		
Gate-Drain Charge	Q <sub>gd</sub>	N-Ch		0.23			
		P-Ch		0.3			
Turn-On Delay Time	t <sub>d(on)</sub>	<b>N-Channel</b> V <sub>DD</sub> = 10 V, R <sub>L</sub> = 20 Ω I <sub>D</sub> ≅ 0.5 A, V <sub>GEN</sub> = 4.5 V, R <sub>G</sub> = 6 Ω <b>P-Channel</b> V <sub>DD</sub> = -10 V, R <sub>L</sub> = 20 Ω I <sub>D</sub> ≅ -0.5 A, V <sub>GEN</sub> = -4.5 V, R <sub>G</sub> = 6 Ω	N-Ch		45	70	ns
			P-Ch		150	230	
Rise Time	t <sub>r</sub>		N-Ch		85	130	
			P-Ch		480	720	
Turn-Off Delay Time	t <sub>d(off)</sub>		N-Ch		350	530	
			P-Ch		840	1200	
Fall Time	t <sub>f</sub>	N-Ch		210	320		
		P-Ch		850	1200		

## Notes

- a. Pulse test; pulse width ≤ 300 μs, duty cycle ≤ 2%.  
b. Guaranteed by design, not subject to production testing.

# **Appendix H**

## **Op-amp (LT6004)**

## FEATURES

- **Wide Supply Range: 1.6V to 16V**
- **Low Supply Current: 1 $\mu$ A/Amplifier Max**
- **Low Input Bias Current: 90pA Max**
- Low Input Offset Voltage: 500 $\mu$ V Max
- Low Input Offset Voltage Drift: 2 $\mu$ V/ $^{\circ}$ C
- CMRR: 100dB
- PSRR: 95dB
- $A_{VOL}$  Driving 20k $\Omega$  Load: 100,000 Min
- Capacitive Load Handling: 500pF
- Specified from  $-40^{\circ}$ C to 125 $^{\circ}$ C
- Available in Tiny 2mm  $\times$  2mm DFN and Low Profile (1mm) ThinSOT<sup>™</sup> Packages

## APPLICATIONS

- Portable Gas Monitors
- Battery- or Solar-Powered Systems
- Low Voltage Signal Processing
- Micropower Active Filters

## DESCRIPTION

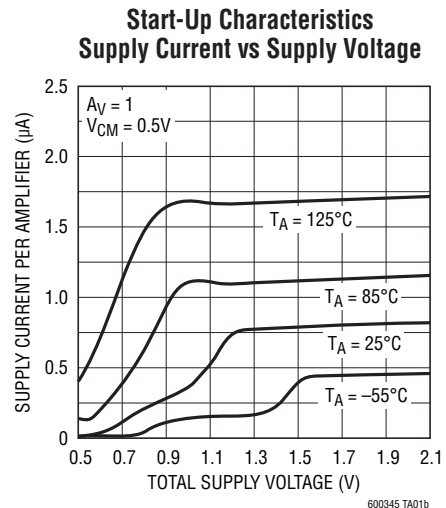
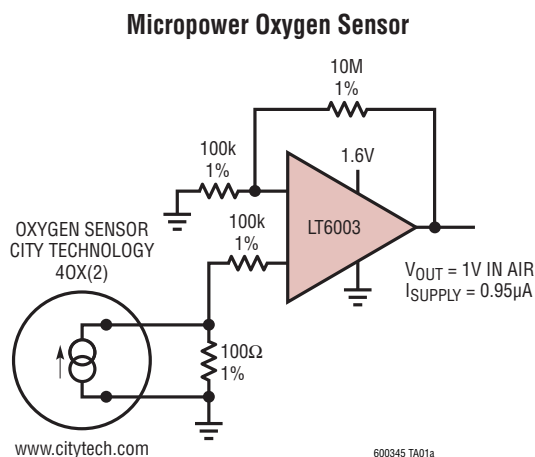
The LT<sup>®</sup>6003/LT6004/LT6005 are single/dual/quad op amps designed to maximize battery life and performance for portable applications. These amplifiers operate on supplies as low as 1.6V and are fully specified and guaranteed over temperature on 1.8V, 5V and  $\pm$ 8V supplies while only drawing 1 $\mu$ A maximum quiescent current.

The ultralow supply current and low operating voltage are combined with excellent amplifier specifications; input offset voltage of 500 $\mu$ V maximum with a typical drift of only 2 $\mu$ V/ $^{\circ}$ C, input bias current of 90pA maximum, open loop gain of 100,000 and the ability to drive 500pF capacitive loads, making the LT6003/LT6004/LT6005 amplifiers ideal when excellent performance is required in battery powered applications.

The single LT6003 is available in the 5-pin TSOT-23 and tiny 2mm  $\times$  2mm DFN packages. The dual LT6004 is available in the 8-pin MSOP and 3mm  $\times$  3mm DFN packages. The quad LT6005 is available in the 16-pin SSOP and 5mm  $\times$  3mm DFN packages. These devices are specified over the commercial, industrial and automotive temperature ranges.

LT, LT, LTC, LTM, Linear Technology and the Linear logo are registered trademarks of Linear Technology Corporation. ThinSOT is a trademark of Linear Technology Corporation. All other trademarks are the property of their respective owners.

## TYPICAL APPLICATION



600345fd

# LT6003/LT6004/LT6005

## ABSOLUTE MAXIMUM RATINGS (Note 1)

Total Supply Voltage ( $V^+$ to $V^-$ ).....	18V	Specified Temperature Range (Note 4)	
Differential Input Voltage.....	18V	LT6003C, LT6004C, LT6005C .....	0°C to 70°C
Input Voltage Below $V^-$ .....	9V	LT6003I, LT6004I, LT6005I.....	-40°C to 85°C
Input Current.....	10mA	LT6003H, LT6004H, LT6005H.....	-40°C to 125°C
Output Short Circuit Duration (Note 2).....	Indefinite	Junction Temperature	
Operating Temperature Range (Note 3)		DFN Packages.....	125°C
LT6003C, LT6004C, LT6005C .....	-40°C to 85°C	All Other Packages.....	150°C
LT6003I, LT6004I, LT6005I.....	-40°C to 85°C	Storage Temperature Range	
LT6003H, LT6004H, LT6005H.....	-40°C to 125°C	DFN Packages.....	-65°C to 125°C
		All Other Packages.....	-65°C to 150°C
		Lead Temperature (Soldering, 10 sec)	
		TSOT, MSOP, SSOP Packages .....	300°C

## PIN CONFIGURATION

<p>LT6003</p> <p>TOP VIEW</p> <p>DC PACKAGE 4-LEAD (2mm × 2mm) PLASTIC DFN</p> <p><math>T_{JMAX} = 125^{\circ}\text{C}</math>, <math>\theta_{JA} = 102^{\circ}\text{C/W}</math> (NOTE 2) EXPOSED PAD (PIN 5) IS <math>V^-</math>. MUST BE SOLDERED TO PCB</p>	<p>LT6003</p> <p>TOP VIEW</p> <p>S5 PACKAGE 5-LEAD PLASTIC TSOT-23</p> <p><math>T_{JMAX} = 150^{\circ}\text{C}</math>, <math>\theta_{JA} = 250^{\circ}\text{C/W}</math></p>	<p>LT6004</p> <p>TOP VIEW</p> <p>DD PACKAGE 8-LEAD (3mm × 3mm) PLASTIC DFN</p> <p><math>T_{JMAX} = 125^{\circ}\text{C}</math>, <math>\theta_{JA} = 160^{\circ}\text{C/W}</math> (NOTE 2) EXPOSED PAD (PIN 9) CONNECTED TO <math>V^-</math> (PCB CONNECTION OPTIONAL)</p>
<p>LT6004</p> <p>TOP VIEW</p> <p>MS8 PACKAGE 8-LEAD PLASTIC MSOP</p> <p><math>T_{JMAX} = 150^{\circ}\text{C}</math>, <math>\theta_{JA} = 250^{\circ}\text{C/W}</math></p>	<p>LT6005</p> <p>TOP VIEW</p> <p>DHC PACKAGE 16-LEAD (5mm × 3mm) PLASTIC DFN</p> <p><math>T_{JMAX} = 125^{\circ}\text{C}</math>, <math>\theta_{JA} = 160^{\circ}\text{C/W}</math> (NOTE 2) EXPOSED PAD (PIN 17) CONNECTED TO <math>V^-</math>. (PCB CONNECTION OPTIONAL)</p>	<p>LT6005</p> <p>TOP VIEW</p> <p>GN PACKAGE 16-LEAD PLASTIC SSOP</p> <p><math>T_{JMAX} = 150^{\circ}\text{C}</math>, <math>\theta_{JA} = 135^{\circ}\text{C/W}</math></p>

## ORDER INFORMATION

LEAD FREE FINISH	TAPE AND REEL	PART MARKING*	PACKAGE DESCRIPTION	SPECIFIED TEMPERATURE RANGE
LT6003CDC#PBF	LT6003CDC#TRPBF	LCKF	4-Lead (2mm × 2mm) Plastic DFN	0°C to 70°C
LT6003IDC#PBF	LT6003IDC#TRPBF	LCKF	4-Lead (2mm × 2mm) Plastic DFN	-40°C to 85°C
LT6003HDC#PBF	LT6003HDC#TRPBF	LCKF	4-Lead (2mm × 2mm) Plastic DFN	-40°C to 125°C
LT6003CS5#PBF	LT6003CS5#TRPBF	LTCKG	5-Lead Plastic TSOT-23	0°C to 70°C
LT6003IS5#PBF	LT6003IS5#TRPBF	LTCKG	5-Lead Plastic TSOT-23	-40°C to 85°C
LT6003HS5#PBF	LT6003HS5#TRPBF	LTCKG	5-Lead Plastic TSOT-23	-40°C to 125°C
LT6004CDD#PBF	LT6004CDD#TRPBF	LCCB	8-Lead (3mm × 3mm) Plastic DFN	0°C to 70°C
LT6004IDD#PBF	LT6004IDD#TRPBF	LCCB	8-Lead (3mm × 3mm) Plastic DFN	-40°C to 85°C
LT6004HDD#PBF	LT6004HDD#TRPBF	LCCB	8-Lead (3mm × 3mm) Plastic DFN	-40°C to 125°C
LT6004CMS8#PBF	LT6004CMS8#TRPBF	LTCBZ	8-Lead Plastic MSOP	0°C to 70°C
LT6004IMS8#PBF	LT6004IMS8#TRPBF	LTCBZ	8-Lead Plastic MSOP	-40°C to 85°C
LT6004HMS8#PBF	LT6004HMS8#TRPBF	LTCBZ	8-Lead Plastic MSOP	-40°C to 125°C
LT6005CDHC#PBF	LT6005CDHC#TRPBF	6005	16-Lead (5mm × 3mm) Plastic DFN	0°C to 70°C
LT6005IDHC#PBF	LT6005IDHC#TRPBF	6005	16-Lead (5mm × 3mm) Plastic DFN	-40°C to 85°C
LT6005HDHC#PBF	LT6005HDHC#TRPBF	6005	16-Lead (5mm × 3mm) Plastic DFN	-40°C to 125°C
LT6005CGN#PBF	LT6005CGN#TRPBF	6005	16-Lead Plastic SSOP	0°C to 70°C
LT6005IGN#PBF	LT6005IGN#TRPBF	6005I	16-Lead Plastic SSOP	-40°C to 85°C
LT6005HGN#PBF	LT6005HGN#TRPBF	6005H	16-Lead Plastic SSOP	-40°C to 125°C

Consult LTC Marketing for parts specified with wider operating temperature ranges. \*The temperature grade is identified by a label on the shipping container. Consult LTC Marketing for information on non-standard lead based finish parts.

For more information on lead free part marking, go to: <http://www.linear.com/leadfree/>

For more information on tape and reel specifications, go to: <http://www.linear.com/tapeandreeel/>

## ELECTRICAL CHARACTERISTICS (LT6003C/I, LT6004C/I, LT6005C/I) The ● denotes the specifications which apply over the full operating temperature range, otherwise specifications are at $T_A = 25^\circ\text{C}$ . $V_S = 1.8\text{V}, 0\text{V}$ , $V_{CM} = 0.5\text{V}$ ; $V_S = 5\text{V}, 0\text{V}$ , $V_{CM} = 2.5\text{V}$ , $V_{OUT} = \text{half supply}$ , $R_L$ to ground, unless otherwise noted.

SYMBOL	PARAMETER	CONDITIONS	MIN	TYP	MAX	UNITS
$V_{OS}$	Input Offset Voltage	LT6003S5, LT6004MS8 $0^\circ\text{C} \leq T_A \leq 70^\circ\text{C}$ $-40^\circ\text{C} \leq T_A \leq 85^\circ\text{C}$	●	175	500	$\mu\text{V}$
			●		725	$\mu\text{V}$
					950	$\mu\text{V}$
		LT6005GN $0^\circ\text{C} \leq T_A \leq 70^\circ\text{C}$ $-40^\circ\text{C} \leq T_A \leq 85^\circ\text{C}$	●	190	650	$\mu\text{V}$
		●		925	$\mu\text{V}$	
		●		1.15	mV	
$\Delta V_{OS}/\Delta T$	Input Offset Voltage Drift (Note 5)	LT6004DD, LT6005DHC $0^\circ\text{C} \leq T_A \leq 70^\circ\text{C}$ $-40^\circ\text{C} \leq T_A \leq 85^\circ\text{C}$	●	290	850	$\mu\text{V}$
			●		1.15	mV
			●		1.4	mV
		LT6003DC $0^\circ\text{C} \leq T_A \leq 70^\circ\text{C}$ $-40^\circ\text{C} \leq T_A \leq 85^\circ\text{C}$	●	290	950	$\mu\text{V}$
		●		1.3	mV	
		●		1.6	mV	
		S5, MS8, GN DC, DD, DHC	●	2	5	$\mu\text{V}/^\circ\text{C}$
			●	2	7	$\mu\text{V}/^\circ\text{C}$

# LT6003/LT6004/LT6005

**ELECTRICAL CHARACTERISTICS** (LT6003C/I, LT6004C/I, LT6005C/I) The ● denotes the specifications which apply over the full operating temperature range, otherwise specifications are at  $T_A = 25^\circ\text{C}$ .  $V_S = 1.8\text{V}, 0\text{V}$ ,  $V_{CM} = 0.5\text{V}$ ;  $V_S = 5\text{V}, 0\text{V}$ ,  $V_{CM} = 2.5\text{V}$ ,  $V_{OUT} = \text{half supply}$ ,  $R_L$  to ground, unless otherwise noted.

SYMBOL	PARAMETER	CONDITIONS	MIN	TYP	MAX	UNITS
$I_B$	Input Bias Current (Note 7)	$V_{CM} = 0.3\text{V}, 0^\circ\text{C} \leq T_A \leq 70^\circ\text{C}$	●	5	90	$\mu\text{A}$
		$V_{CM} = V^+ - 0.3\text{V}, 0^\circ\text{C} \leq T_A \leq 70^\circ\text{C}$	●	40	140	$\mu\text{A}$
		$V_{CM} = 0.3\text{V}, -40^\circ\text{C} \leq T_A \leq 85^\circ\text{C}$	●	5	120	$\mu\text{A}$
		$V_{CM} = V^+ - 0.3\text{V}, -40^\circ\text{C} \leq T_A \leq 85^\circ\text{C}$	●	40	170	$\mu\text{A}$
		$V_{CM} = 0\text{V}$	●	0.13	1.4	$\text{nA}$
$I_{OS}$	Input Offset Current (Note 7)	$V_{CM} = 0.3\text{V}$	●	5	80	$\mu\text{A}$
		$V_{CM} = V^+ - 0.3\text{V}$	●	7	80	$\mu\text{A}$
		$V_{CM} = 0\text{V}$	●	5	100	$\mu\text{A}$
	Input Noise Voltage	0.1Hz to 10Hz		3		$\mu\text{V}_{P-P}$
$e_n$	Input Noise Voltage Density	$f = 100\text{Hz}$		325		$\text{nV}/\sqrt{\text{Hz}}$
$i_n$	Input Noise Current Density	$f = 100\text{Hz}$		12		$\text{fA}/\sqrt{\text{Hz}}$
$R_{IN}$	Input Resistance	Differential		10		$\text{G}\Omega$
		Common Mode		2000		$\text{G}\Omega$
$C_{IN}$	Input Capacitance			6		$\text{pF}$
CMRR	Common Mode Rejection Ratio (Note 7)	$V_S = 1.8\text{V}$	●	73	100	$\text{dB}$
		$V_{CM} = 0\text{V to } 0.7\text{V}$	●	63	80	$\text{dB}$
		$V_{CM} = 0\text{V to } 1.8\text{V}, \text{S5, MS8, GN}$	●	60	78	$\text{dB}$
		$V_{CM} = 0\text{V to } 1.8\text{V}, \text{DC, DD, DHC}$	●			
		$V_S = 5\text{V}$	●	88	115	$\text{dB}$
		$V_{CM} = 0\text{V to } 3.9\text{V}$	●	72	90	$\text{dB}$
		$V_{CM} = 0\text{V to } 5\text{V}, \text{S5, MS8, GN}$	●	69	86	$\text{dB}$
	Input Offset Voltage Shift (Note 7)	$V_{CM} = 0\text{V to } V^+ - 1.1\text{V}$	●	7	155	$\mu\text{V}$
		$V_{CM} = 0\text{V to } V^+, \text{S5, MS8, GN}$	●	0.16	1.3	$\text{mV}$
		$V_{CM} = 0\text{V to } V^+, \text{DC, DD, DHC}$	●	0.23	1.8	$\text{mV}$
	Input Voltage Range	Guaranteed by CMRR	●	0	$V^+$	$V$
PSRR	Power Supply Rejection Ratio	$V_S = 1.6\text{V to } 6\text{V}, V_{CM} = 0.5\text{V}, 0^\circ\text{C} \leq T_A \leq 70^\circ\text{C}$	●	80	95	$\text{dB}$
		$V_S = 1.7\text{V to } 6\text{V}, V_{CM} = 0.5\text{V}, -40^\circ\text{C} \leq T_A \leq 85^\circ\text{C}$	●	78	95	$\text{dB}$
	Minimum Supply Voltage	Guaranteed by PSRR, $0^\circ\text{C} \leq T_A \leq 70^\circ\text{C}$	●	1.6		$V$
		$-40^\circ\text{C} \leq T_A \leq 85^\circ\text{C}$	●	1.7		$V$
$A_{VOL}$	Large Signal Voltage Gain (Note 7)	$V_S = 1.8\text{V}$ $R_L = 20\text{k}\Omega, V_{OUT} = 0.25\text{V to } 1.25\text{V}$	●	25	150	$\text{V}/\text{mV}$
		$V_S = 5\text{V}$ $R_L = 20\text{k}\Omega, V_{OUT} = 0.25\text{V to } 4.25\text{V}$	●	100	500	$\text{V}/\text{mV}$
$V_{OL}$	Output Swing Low (Notes 6, 8)	No Load	●	15	50	$\text{mV}$
		$I_{SINK} = 100\mu\text{A}$	●	110	240	$\text{mV}$
$V_{OH}$	Output Swing High (Notes 6, 9)	No Load	●	45	100	$\text{mV}$
		$I_{SOURCE} = 100\mu\text{A}$	●	200	350	$\text{mV}$
$I_{SC}$	Short Circuit Current (Note 8)	Short to GND	●	2	5	$\text{mA}$
		$0^\circ\text{C} \leq T_A \leq 70^\circ\text{C}$	●	1.5		$\text{mA}$
		$-40^\circ\text{C} \leq T_A \leq 85^\circ\text{C}$	●	0.5		$\text{mA}$
		Short to $V^+$	●	2	7	$\text{mA}$
		$0^\circ\text{C} \leq T_A \leq 70^\circ\text{C}$	●	1.5		$\text{mA}$
		$-40^\circ\text{C} \leq T_A \leq 85^\circ\text{C}$	●	0.5		$\text{mA}$
$I_S$	Supply Current per Amplifier	$V_S = 1.8\text{V}$	●	0.85	1	$\mu\text{A}$
		$0^\circ\text{C} \leq T_A \leq 70^\circ\text{C}$	●		1.4	$\mu\text{A}$
		$-40^\circ\text{C} \leq T_A \leq 85^\circ\text{C}$	●		1.6	$\mu\text{A}$
		$V_S = 5\text{V}$	●	1	1.2	$\mu\text{A}$
		$0^\circ\text{C} \leq T_A \leq 70^\circ\text{C}$	●		1.6	$\mu\text{A}$
		$-40^\circ\text{C} \leq T_A \leq 85^\circ\text{C}$	●		1.9	$\mu\text{A}$

600345fd

**ELECTRICAL CHARACTERISTICS** (LT6003C/I, LT6004C/I, LT6005C/I) The ● denotes the specifications which apply over the full operating temperature range, otherwise specifications are at  $T_A = 25^\circ\text{C}$ .  $V_S = 1.8\text{V}$ ,  $0\text{V}$ ,  $V_{CM} = 0.5\text{V}$ ;  $V_S = 5\text{V}$ ,  $0\text{V}$ ,  $V_{CM} = 2.5\text{V}$ ,  $V_{OUT} = \text{half supply}$ ,  $R_L$  to ground, unless otherwise noted.

SYMBOL	PARAMETER	CONDITIONS	MIN	TYP	MAX	UNITS
GBW	Gain Bandwidth Product	$f = 100\text{Hz}$		2		kHz
SR	Slew Rate (Note 11)	$A_V = -1$ , $R_F = R_G = 1\text{M}\Omega$ $0^\circ\text{C} \leq T_A \leq 70^\circ\text{C}$ $-40^\circ\text{C} \leq T_A \leq 85^\circ\text{C}$	0.55 ● 0.4 ● 0.2	0.8		V/ms V/ms V/ms
FPBW	Full Power Bandwidth	$V_{OUT} = 1.5V_{P-P}$ (Note 10)		170		Hz

(LT6003H, LT6004H, LT6005H) The ● denotes the specifications which apply over the full specified temperature range of  $-40^\circ\text{C} \leq T_A \leq 125^\circ\text{C}$ .  $V_S = 1.8\text{V}$ ,  $0\text{V}$ ,  $V_{CM} = 0.5\text{V}$ ;  $V_S = 5\text{V}$ ,  $0\text{V}$ ,  $V_{CM} = 2.5\text{V}$ ,  $V_{OUT} = \text{half supply}$ ,  $R_L$  to ground, unless otherwise noted.

SYMBOL	PARAMETER	CONDITIONS	MIN	TYP	MAX	UNITS
$V_{OS}$	Input Offset Voltage	LT6003S5, LT6004MS8 LT6005GN LT6004DD, LT6005DHC LT6003DC	● ● ●		1.5 1.7 1.9 2.1	mV mV mV mV
$\Delta V_{OS}/\Delta T$	Input Offset Voltage Drift (Note 5)	S5, MS8, GN DC, DD, DHC	● ●	2 3	6 8	$\mu\text{V}/^\circ\text{C}$ $\mu\text{V}/^\circ\text{C}$
$I_B$	Input Bias Current (Note 7)	LT6003, $V_{CM} = 0.3\text{V}$ , $V^+ - 0.3\text{V}$ LT6004, LT6005, $V_{CM} = 0.3\text{V}$ , $V^+ - 0.3\text{V}$	● ●		6 12	nA nA
$I_{OS}$	Input Offset Current (Note 7)	LT6003, $V_{CM} = 0.3\text{V}$ , $V^+ - 0.3\text{V}$ LT6004, LT6005, $V_{CM} = 0.3\text{V}$ , $V^+ - 0.3\text{V}$	● ●		2 4	nA nA
CMRR	Common Mode Rejection Ratio (Note 7)	$V_S = 1.8\text{V}$ $V_{CM} = 0.3\text{V}$ to $0.7\text{V}$ $V_{CM} = 0.3\text{V}$ to $1.5\text{V}$ , S5, MS8, GN $V_{CM} = 0.3\text{V}$ to $1.5\text{V}$ , DC, DD, DHC	● ● ●	67 57 55		dB dB dB
		$V_S = 5\text{V}$ $V_{CM} = 0.3\text{V}$ to $3.9\text{V}$ $V_{CM} = 0.3\text{V}$ to $4.7\text{V}$ , S5, MS8, GN $V_{CM} = 0.3\text{V}$ to $4.7\text{V}$ , DC, DD, DHC	● ● ●	86 68 66		dB dB dB
	Input Offset Voltage Shift (Note 7)	$V_{CM} = 0.3\text{V}$ to $V^+ - 1.1\text{V}$ $V_{CM} = 0.3\text{V}$ to $V^+ - 0.3\text{V}$ , S5, MS8, GN $V_{CM} = 0.3\text{V}$ to $V^+ - 0.3\text{V}$ , DC, DD, DHC	● ● ●		180 1.7 2.2	$\mu\text{V}$ mV mV
	Input Voltage Range	Guaranteed by CMRR	●	0.3	$V^+ - 0.3\text{V}$	V
PSRR	Power Supply Rejection Ratio	$V_S = 1.7\text{V}$ to $6\text{V}$ , $V_{CM} = 0.5\text{V}$	●	76		dB
	Minimum Supply	Guaranteed by PSRR	●	1.7		V
$A_{VOL}$	Large Signal Voltage Gain (Note 7)	$V_S = 1.8\text{V}$ , $R_L = 20\text{k}\Omega$ , $V_{OUT} = 0.4\text{V}$ to $1.25\text{V}$ $V_S = 5\text{V}$ , $R_L = 20\text{k}\Omega$ , $V_{OUT} = 0.4\text{V}$ to $4.25\text{V}$	● ●	4 20		V/mV V/mV
$V_{OL}$	Output Swing Low (Notes 6, 8)	No Load $I_{SINK} = 100\mu\text{A}$	● ●		60 275	mV mV
$V_{OH}$	Output Swing High (Notes 6, 9)	No Load $I_{SOURCE} = 100\mu\text{A}$	● ●		120 400	mV mV
$I_{SC}$	Short Circuit Current (Note 8)	Short to GND Short to $V^+$	● ●	0.5 0.5		mA mA
$I_S$	Supply Current per Amplifier	$V_S = 1.8\text{V}$ $V_S = 5\text{V}$	● ●		2.2 2.5	$\mu\text{A}$ $\mu\text{A}$
SR	Slew Rate (Note 11)	$A_V = -1$ , $R_F = R_G = 1\text{M}\Omega$	●	0.2		V/ms



# LT6003/LT6004/LT6005

**ELECTRICAL CHARACTERISTICS** (LT6003C/I, LT6004C/I, LT6005C/I) The ● denotes the specifications which apply over the full operating temperature range, otherwise specifications are at  $T_A = 25^\circ\text{C}$ .  $V_S = \pm 8\text{V}$ ,  $V_{CM} = V_{OUT} = \text{half supply}$ ,  $R_L$  to ground, unless otherwise noted.

SYMBOL	PARAMETER	CONDITIONS	MIN	TYP	MAX	UNITS
$V_{OS}$	Input Offset Voltage	LT6003S5, LT6004MS8 $0^\circ\text{C} \leq T_A \leq 70^\circ\text{C}$ $-40^\circ\text{C} \leq T_A \leq 85^\circ\text{C}$	●	185	600	$\mu\text{V}$
			●		825	$\mu\text{V}$
					1.05	mV
		LT6005GN $0^\circ\text{C} \leq T_A \leq 70^\circ\text{C}$ $-40^\circ\text{C} \leq T_A \leq 85^\circ\text{C}$	●	200	750	$\mu\text{V}$
		●		1.05	mV	
		●		1.25	mV	
		LT6004DD, LT6005DHC $0^\circ\text{C} \leq T_A \leq 70^\circ\text{C}$ $-40^\circ\text{C} \leq T_A \leq 85^\circ\text{C}$	●	300	950	$\mu\text{V}$
			●		1.25	mV
					1.5	mV
		LT6003DC $0^\circ\text{C} \leq T_A \leq 70^\circ\text{C}$ $-40^\circ\text{C} \leq T_A \leq 85^\circ\text{C}$	●	0.3	1.05	mV
		●		1.4	mV	
		●		1.65	mV	
$\Delta V_{OS}/\Delta T$	Input Offset Voltage Drift (Note 5)	S5, MS8, GN DC, DD, DHC	●	2	5	$\mu\text{V}/^\circ\text{C}$
			●	2	7	$\mu\text{V}/^\circ\text{C}$
$I_B$	Input Bias Current	$0^\circ\text{C} \leq T_A \leq 70^\circ\text{C}$ $-40^\circ\text{C} \leq T_A \leq 85^\circ\text{C}$	●	7	100	$\mu\text{A}$
			●	7	150	$\mu\text{A}$
$I_{OS}$	Input Offset Current		●	7	90	$\mu\text{A}$
	Input Noise Voltage	0.1Hz to 10Hz		3		$\mu\text{V}_{P-P}$
$e_n$	Input Noise Voltage Density	$f = 100\text{Hz}$		325		$\text{nV}/\sqrt{\text{Hz}}$
$i_n$	Input Noise Current Density	$f = 100\text{Hz}$		12		$\text{fA}/\sqrt{\text{Hz}}$
$R_{IN}$	Input Resistance	Differential		10		$\text{G}\Omega$
		Common Mode		2000		$\text{G}\Omega$
$C_{IN}$	Input Capacitance			6		$\text{pF}$
CMRR	Common Mode Rejection Ratio	$V_{CM} = -8\text{V}$ to 6.9V	●	92	120	dB
		$V_{CM} = -8\text{V}$ to 8V, S5, MS8, GN	●	82	100	dB
		$V_{CM} = -8\text{V}$ to 8V, DC, DD, DHC	●	78	96	dB
	Input Offset Voltage Shift	$V_{CM} = -8\text{V}$ to 6.9V	●	15	375	$\mu\text{V}$
		$V_{CM} = -8\text{V}$ to 8V, S5, MS8, GN	●	0.16	1.3	mV
		$V_{CM} = -8\text{V}$ to 8V, DC, DD, DHC	●	0.25	2	mV
	Input Voltage Range	Guaranteed by CMRR	●	-8	8	V
PSRR	Power Supply Rejection Ratio	$V_S = \pm 1.1\text{V}$ to $\pm 8\text{V}$	●	86	105	dB
$A_{VOL}$	Large Signal Voltage Gain	$R_L = 100\text{k}\Omega$ , $V_{OUT} = -7.3\text{V}$ to 7.3V		350		V/mV
$V_{OL}$	Output Swing Low (Notes 6, 8)	No Load	●	10	50	mV
		$I_{SINK} = 100\mu\text{A}$	●	105	240	mV
$V_{OH}$	Output Swing High (Notes 6, 9)	No Load	●	50	120	mV
		$I_{SOURCE} = 100\mu\text{A}$	●	195	350	mV
$I_{SC}$	Short Circuit Current	Short to GND	●	4	9	mA
		$0^\circ\text{C} \leq T_A \leq 70^\circ\text{C}$	●	3		mA
		$-40^\circ\text{C} \leq T_A \leq 85^\circ\text{C}$	●	1		mA
$I_S$	Supply Current per Amplifier	$0^\circ\text{C} \leq T_A \leq 70^\circ\text{C}$	●	1.25	1.5	$\mu\text{A}$
		$-40^\circ\text{C} \leq T_A \leq 85^\circ\text{C}$	●		1.9	$\mu\text{A}$
			●		2.2	$\mu\text{A}$
GBW	Gain Bandwidth Product	$f = 100\text{Hz}$		3		kHz
SR	Slew Rate (Note 11)	$A_V = -1$ , $R_F = R_G = 1\text{M}\Omega$	●	0.55	1.3	V/ms
		$0^\circ\text{C} \leq T_A \leq 70^\circ\text{C}$	●	0.4		V/ms
		$-40^\circ\text{C} \leq T_A \leq 85^\circ\text{C}$	●	0.2		V/ms
FPBW	Full Power Bandwidth	$V_{OUT} = 14\text{V}_{P-P}$ (Note 10)		30		Hz

**ELECTRICAL CHARACTERISTICS** (LT6003H, LT6004H, LT6005H) The ● denotes the specifications which apply over the full specified temperature range of  $-40^{\circ}\text{C} \leq T_A \leq 125^{\circ}\text{C}$ .  $V_S = \pm 8\text{V}$ ,  $V_{\text{CM}} = V_{\text{OUT}} = \text{half supply}$ ,  $R_L$  to ground, unless otherwise noted.

SYMBOL	PARAMETER	CONDITIONS	MIN	TYP	MAX	UNITS
$V_{\text{OS}}$	Input Offset Voltage	LT6003S5, LT6004MS8	●		1.6	mV
		LT6005GN	●		1.8	mV
		LT6004DD, LT6005DHC	●		2	mV
		LT6003DC	●		2.2	mV
$\Delta V_{\text{OS}}/\Delta T$	Input Offset Voltage Drift (Note 5)	S5, MS8, GN DC, DD, DHC	● ●	2 3	6 8	$\mu\text{V}/^{\circ}\text{C}$ $\mu\text{V}/^{\circ}\text{C}$
$I_B$	Input Bias Current	LT6003	●		6	nA
		LT6004, LT6005	●		12	nA
$I_{\text{OS}}$	Input Offset Current	LT6003	●		2	nA
		LT6004, LT6005	●		4	nA
CMRR	Common Mode Rejection Ratio	$V_{\text{CM}} = -7.7\text{V}$ to $6.9\text{V}$	●	90		dB
		$V_{\text{CM}} = -7.7\text{V}$ to $7.7\text{V}$ , S5, MS8, GN	●	78		dB
		$V_{\text{CM}} = -7.7\text{V}$ to $7.7\text{V}$ , DC, DD, DHC	●	76		dB
	Input Offset Voltage Shift	$V_{\text{CM}} = -7.7\text{V}$ to $6.9\text{V}$	●		460	$\mu\text{V}$
		$V_{\text{CM}} = -7.7\text{V}$ to $7.7\text{V}$ , S5, MS8, GN	●		1.9	mV
		$V_{\text{CM}} = -7.7\text{V}$ to $7.7\text{V}$ , DC, DD, DHC	●		2.5	mV
	Input Voltage Range	Guaranteed by CMRR	●	-7.7	7.7	V
PSRR	Power Supply Rejection Ratio	$V_S = \pm 1.1\text{V}$ to $\pm 8\text{V}$	●	84		dB
$V_{\text{OL}}$	Output Swing Low (Notes 6, 8)	No Load	●		60	mV
		$I_{\text{SINK}} = 100\mu\text{A}$	●		275	mV
$V_{\text{OH}}$	Output Swing High (Note 6)	No Load	●		140	mV
		$I_{\text{SOURCE}} = 100\mu\text{A}$	●		400	mV
$I_{\text{SC}}$	Short Circuit Current	Short to GND	●	1		mA
$I_S$	Supply Current per Amplifier		●		3	$\mu\text{A}$
SR	Slew Rate (Note 11)	$A_V = -1$ , $R_F = R_G = 1\text{M}\Omega$	●	0.2		V/ms

**Note 1:** Stresses beyond those listed under Absolute Maximum Ratings may cause permanent damage to the device. Exposure to any Absolute Maximum Rating condition for extended periods may affect device reliability and lifetime.

**Note 2:** A heat sink may be required to keep the junction temperature below absolute maximum. This depends on the power supply voltage and how many amplifiers are shorted. The  $\theta_{\text{JA}}$  specified for the DC, DD and DHC packages is with minimal PCB heat spreading metal. Using expanded metal area on all layers of a board reduces this value.

**Note 3:** The LT6003C/LT6004C/LT6005C and LT6003I/LT6004I/LT6005I are guaranteed functional over the temperature range of  $-40^{\circ}\text{C}$  to  $85^{\circ}\text{C}$ . The LT6003H/LT6004H/LT6005H are guaranteed functional over the operating temperature range of  $-40^{\circ}\text{C}$  to  $125^{\circ}\text{C}$ .

**Note 4:** The LT6003C/LT6004C/LT6005C are guaranteed to meet specified performance from  $0^{\circ}\text{C}$  to  $70^{\circ}\text{C}$ . The LT6003I/LT6004I/LT6005I are designed, characterized and expected to meet specified performance from

$-40^{\circ}\text{C}$  to  $85^{\circ}\text{C}$  but are not tested or QA sampled at these temperatures. The LT6003I/LT6004I/LT6005I are guaranteed to meet specified performance from  $-40^{\circ}\text{C}$  to  $85^{\circ}\text{C}$ . The LT6003H/LT6004H/LT6005H are guaranteed to meet specified performance from  $-40^{\circ}\text{C}$  to  $125^{\circ}\text{C}$ .

**Note 5:** This parameter is not 100% tested.

**Note 6:** Output voltage swings are measured between the output and power supply rails.

**Note 7:** Limits are guaranteed by correlation to  $V_S = 5\text{V}$  tests.

**Note 8:** Limits are guaranteed by correlation to  $V_S = 1.8\text{V}$  tests

**Note 9:** Limits are guaranteed by correlation to  $V_S = \pm 8\text{V}$  tests

**Note 10:** Full-power bandwidth is calculated from the slew rate:

$$\text{FPBW} = \text{SR}/\pi V_{\text{P-P}}$$

**Note 11:** Slew rate measured at  $V_S = 1.8\text{V}$ ,  $V_{\text{OUT}} = 0.4\text{V}$  to  $1.4\text{V}$  is used to guarantee by correlation the slew rate at  $V_S = 5\text{V}$ ,  $V_{\text{OUT}} = 1\text{V}$  to  $4\text{V}$  and the slew rate at  $V_S = \pm 8\text{V}$ ,  $V_{\text{OUT}} = -5\text{V}$  to  $5\text{V}$ .

# Bibliography

- [1] Moore, G. E. ; , No Exponential is Forever: But Forever Can Be Delayed!, Solid-State Circuits Conference, 2003.
- [2] Paradiso, J.A.; Starner, T.; , "Energy scavenging for mobile and wireless electronics," Pervasive Computing, IEEE , vol.4, no.1, pp. 18- 27, Jan.-March 2005
- [3] Matsumoto, S.; Shodai, T.; Kanai, Y.; , "A novel strategy of a control IC for boost converter with ultra low voltage input and maximum power point tracking for single solar cell application," Power Semiconductor Devices & IC's, 2009. ISPSD 2009. 21st International Symposium on , vol., no., pp.180-183, 14-18 June 2009
- [4] Jiyong Li; Honghua Wang; , "Maximum Power Point Tracking of Photovoltaic Generation Based on the Optimal Gradient Method," Power and Energy Engineering Conference, 2009. APPEEC 2009. Asia-Pacific , vol., no., pp.1-4, 27-31 March 2009
- [5] Hung-Ching Lu; Te-Lung Shih; , "Design of DC/DC Boost converter with FNN solar cell Maximum Power Point Tracking controller," Industrial Electronics and Applications (ICIEA), 2010 the 5th IEEE Conference on , vol., no., pp.802-807, 15-17 June 2010
- [6] Wei Peiyu; Tan Boxue; Zhang Housheng; Zhao Yanlei; , "Research on maximum power point tracker based on solar cells simulator," Advanced Computer Control (ICACC), 2010 2nd International Conference on , vol.1, no., pp.319-323, 27-29 March 2010

- [7] Holmes, A.S.; Guodong Hong; Pullen, K.R.; , "Axial-flux permanent magnet machines for micropower generation," *Microelectromechanical Systems, Journal of* , vol.14, no.1, pp. 54- 62, Feb. 2005
- [8] Philipose, M.; Smith, J.R.; Jiang, B.; Mamishev, A.; Sumit Roy; Sundara-Rajan, K.; , "Battery-free wireless identification and sensing," *Pervasive Computing, IEEE* , vol.4, no.1, pp. 37- 45, Jan.-March 2005
- [9] Roundy, S; Wright, P.K; Rabaey, J; , "A Study of Low Level Vibrations as a Power Source for Wireless Sensor Nodes," *Computer Communications*, 26(11):1131-1144, July 2003.
- [10] Mateu, L; Codrea, C; Lucas, N; Pollak, N; and Spies, P;, "Energy harvesting for wireless communication systems using thermogenerators," in *Proc. of the XXI Conference on Design of Circuits and Integrated Systems (DCIS)*, Barcelona, Spain, Nov 2006.
- [11] Brooks, G. A. ; Fahey, T. D. ; and Baldwin, K. M.;; "Exercise Physiology: Human Bioenergetics and Its Applications," McGraw-Hill, Boston, 2005.
- [12] Mitcheson, P. D; , "Analysis and Optimisation of Energy Harvesting Micro-Generator Systems," PhD Thesis, University of London, 2005.
- [13] Ottman, G.K.; Hofmann, H.F.; Bhatt, A.C.; Lesieutre, G.A.; , "Adaptive piezoelectric energy harvesting circuit for wireless remote power supply," *Power Electronics, IEEE Transactions on* , vol.17, no.5, pp. 669- 676, Sep 2002
- [14] Ottman, G.K.; Hofmann, H.F.; Lesieutre, G.A.; , "Optimized piezoelectric energy harvesting circuit using step-down converter in discontinuous conduction mode," *Power Electronics, IEEE Transactions on* , vol.18, no.2, pp. 696- 703, Mar 2003
- [15] Ammar, Y ; Buhning, A. ; Marzencki, M. ; Charlot, B. ; Basrour, S. ; Matou, K. ; and Renaudin, M.;; "Wireless sensor network node with asynchronous architecture and vibration harvesting micro power generator," pp. 287–292, 2005

- [16] Lefeuvre, E. ; Badel, A. ; Richard, C. ; and Guyomar, D. ; , Piezoelectric energy harvesting device optimization by synchronous electric charge extraction,"J. Intell. Master. Syst. Struct. vol. 16 pp. 865-76, 2005.
- [17] E. Lefeuvre, A. Badel, C. Richard, and D. Guyomar; , "High Performance Piezoelectric Vibration Energy Reclamation," Smart Structures and Integrated Systems, vol. 5390, pp. 865- 876, Bellingham, WA, 2004.
- [18] Badel, A; Guyomar, D. ; Lefeuvre, E. ; and Richard, C. ; " Efficiency Enhancement of a piezoelectric energy harvesting device in pulsed operation by a synchronous charge inversion," J. Intell. Master. Syst. Struct.vol. 16, pp. 889- 901, Oct. 2005.
- [19] Guyomar, D.; Badel, A.; Lefeuvre, E.; Richard, C.; , "Toward energy harvesting using active materials and conversion improvement by nonlinear processing," Ultrasonics, Ferroelectrics and Frequency Control, IEEE Transactions on , vol.52, no.4, pp.584-595, April 2005
- [20] Shu, Y. C. ; Lien, I. C. ; and Wu. W. J.; , "An Improved Analysis of the SSHI Interface in Piezoelectric energy harvesting , "J. Smart Mater. Struct. vol. 16, pp. 2253-2264, 2007.
- [21] Lefeuvre, E. ; Badel, A. ; Richard, A. ; Petit, L. ; Guyomar, D. ; , " A comparison between several vibration-powered piezoelectric generators for standalone systems," Sensors and Actuators A: Physical, vol. 126, pp. 405-416, 14 February 2006
- [22] Lefeuvre, E.; Audigier, D.; Richard, C.; Guyomar, D.; , "Buck-Boost Converter for Sensorless Power Optimization of Piezoelectric Energy Harvester," Power Electronics, IEEE Transactions on , vol.22, no.5, pp.2018-2025, Sept. 2007
- [23] Jansen, A.J.; Stevels, A.L.N.; , "Human power, a sustainable option for electronics," Electronics and the Environment, 1999. ISEE -1999. Proceedings of the 1999 IEEE International Symposium on , vol., no., pp.215-218, 1999
- [24] Shenck, N.S.; Paradiso, J.A.; , "Energy scavenging with shoe-mounted piezoelectrics," Micro, IEEE , vol.21, no.3, pp.30-42, May/Jun 2001

- [25] Mateu, L. ; Fonellosa, F. ; and Moll, F. ; , "Electrical characterization of a piezoelectric film-based power generator for autonomous wearable devices" Proc. 18th Conf. on Design of Circuits and Integrated Systems, pp. 67782, 2003
- [26] Donelan, J. M., Li, Q. and Naing, V.; , Biomechanical energy harvesting: Generating electricity during walking with minimal user effort Science, vol. 139, pp. 807810, Feb. 2008.
- [27] Granstrom, J., Feenstra, J., Sodano, H. A. and Farinholt, K.; , Energy harvesting from a backpack instrumented with piezoelectric shoulder straps Smart Materials and Structures, (16) pp. 1810-1820, 2007.
- [28] Vijayaraghavan, K.; Rajamani, R.; , "Active Control Based Energy Harvesting for Battery-Less Wireless Traffic Sensors," American Control Conference, 2007. ACC '07 , vol., no., pp.3106-3111, 9-13 July 2007 Conf., 2007, pp. 31063111.
- [29] Vijayaraghavan, K.; Rajamani, R.; , "Novel Batteryless Wireless Sensor for Traffic-Flow Measurement," Vehicular Technology, IEEE Transactions on , vol.59, no.7, pp.3249-3260, Sept. 2010
- [30] Tan, Y.K.; Hoe, K.Y.; Panda, S.K.; , "Energy Harvesting using Piezoelectric Igniter for Self-Powered Radio Frequency (RF) Wireless Sensors," Industrial Technology, 2006. ICIT 2006. IEEE International Conference on , vol., no., pp.1711-1716, 15-17 Dec. 2006
- [31] Ertuk, A., Renno, J. M. and Inman, D. J.; , Modeling of piezoelectric energy harvesting from an L-shaped beam-mass structure with an application to UAVs Intelligent Mate. Sys. Struct., vol. 20, no. 5, pp. 529-544, 2009.
- [32] Khameneifar, F.; Arzanpour, S. and Moallem, M.; , Vibration energy harvesting from a hydraulic engine mount via PZT decoupler, ASME International Mechanical Engineering Congress and Exposition, Vancouver, BC, Canada, pp. 1-8, 2010.
- [33] Leland, E. S. ; Lai, E. M. ; and Wright, P. K. ; , " A self-powered sensor for indoor environmental monitoring, " 2004 Wireless Networking Symposium, October, 2004.

- [34] Ng, T. H. ; and Liao. W. H. ; , "Sensitivity analysis and energy harvesting for a self-powered piezoelectric sensor, " *J. Intell. Mater. Syst. Struct.* vol. 16, pp. 785- 797, Oct. 2005.
- [35] Sodano, H. A. ; and Inman, D. J. ; "Generating and storage of Electricity from power harvesting devices," *J. Intell. Mater. Syst. Struct.*, 2005. vol. 16 (1), pp. 67-75, 2005.
- [36] <http://canmetenergy-canmetenergie.nrcan-rncan.gc.ca/eng/renewables/standalone/publications/2006046.html>
- [37] Petreus, D.; Ciocan, I.; Farcas, C.; , "An improvement on empirical modelling of photovoltaic cells," *Electronics Technology*, 2008. ISSE '08. 31st International Spring Seminar on , vol., no., pp.598-603, 7-11 May 2008
- [38] Hussein, K.H.; Muta, I.; Hoshino, T.; Osakada, M.; , "Maximum photovoltaic power tracking: an algorithm for rapidly changing atmospheric conditions," *Generation, Transmission and Distribution, IEE Proceedings-* , vol.142, no.1, pp.59-64, Jan 1995
- [39] Brambilla, A.; Gambarara, M.; Garutti, A.; Ronchi, F.; , "New approach to photovoltaic arrays maximum power point tracking , " *Power Electronics Specialists Conference, 1999. PESC 99. 30th Annual IEEE* , vol.2, no., pp.632-637 vol.2, 1999
- [40] Irisawa, K.; Saito, T.; Takano, I.; Sawada, Y.; , "Maximum power point tracking control of photovoltaic generation system under non-uniform insolation by means of monitoring cells," *Photovoltaic Specialists Conference, 2000. Conference Record of the Twenty-Eighth IEEE* , vol., no., pp.1707-1710, 2000
- [41] T.-Y. Kim, H.-G. Ahn, S. K. Park, and Y.-K. Lee, "A novel maximum power point tracking control for photovoltaic power system under rapidly changing solar radiation," *IEEE International Symp. on Ind. Electron.* , pp. 1011-1014, 2001.
- [42] Kuo, Y. C; Liang, T. J; Chen, J. F; , "Novel maximum-power-point-tracking controller for photovoltaic energy conversion system," *Industrial Electronics, IEEE Transactions on* , vol.48, no.3, pp.594-601, Jun 2001

- [43] Hashimoto, O.; Shimizu, T.; Kimura, G.; , "A novel high performance utility interactive photovoltaic inverter system," Industry Applications Conference, 2000. Conference Record of the 2000 IEEE , vol.4, no., pp.2255-2260 vol.4, Oct 2000
- [44] Koutroulis, E.; Kalaitzakis, K.; Voulgaris, N.C.; , "Development of a microcontroller-based, photovoltaic maximum power point tracking control system," Power Electronics, IEEE Transactions on , vol.16, no.1, pp.46-54, Jan 2001
- [45] Veerachary, M.; Senjyu, T.; Uezato, K.; , "Maximum power point tracking control of IDB converter supplied PV system," Electric Power Applications, IEE Proceedings - , vol.148, no.6, pp.494-502, Nov 2001
- [46] Weidong Xiao; Dunford, W.G.; , "A modified adaptive hill climbing MPPT method for photovoltaic power systems," Power Electronics Specialists Conference, 2004. PESC 04. 2004 IEEE 35th Annual , vol.3, no., pp. 1957- 1963 Vol.3, 20-25 June 2004
- [47] Masoum, M. A.; Dehbonei, H.; Fuchs, E. F.; , "Theoretical and Experimental Analyses of Photovoltaic Systems with Voltage and Current-Based Maximum Power Point Tracking," Power Engineering Review, IEEE , vol.22, no.8, pp.62, Aug. 2002
- [48] Hyeong-Ju Noh; Dong-Yun Lee; Dong-Seok Hyun; , "An improved MPPT converter with current compensation method for small scaled PV-applications," IECON 02 [Industrial Electronics Society, IEEE 2002 28th Annual Conference of the] , vol.2, no., pp. 1113- 1118 vol.2, 5-8 Nov. 2002
- [49] Kobayashi, K.; Matsuo, H.; Sekine, Y.; , "A novel optimum operating point tracker of the solar cell power supply system," Power Electronics Specialists Conference, 2004. PESC 04. 2004 IEEE 35th Annual , vol.3, no., pp. 2147- 2151 Vol.3, 20-25 June 2004
- [50] Bekker, B.; Beukes, H.J.; , "Finding an optimal PV panel maximum power point tracking method," AFRICON, 2004. 7th AFRICON Conference in Africa , vol.2, no., pp. 1125- 1129 Vol.2, 15-17 Sept. 2004



- [51] Noguchi, T.; Togashi, S.; Nakamoto, R.; , "Short-current pulse based adaptive maximum-power-point tracking for photovoltaic power generation system," *Industrial Electronics*, 2000. ISIE 2000. Proceedings of the 2000 IEEE International Symposium on , vol.1, no., pp.157-162 vol.1, 2000
- [52] Mutoh, N.; Matuo, T.; Okada, K.; Sakai, M.; , "Prediction-data-based maximum-power-point-tracking method for photovoltaic power generation systems," *Power Electronics Specialists Conference, 2002. pesc 02. 2002 IEEE 33rd Annual* , vol.3, no., pp. 1489- 1494 vol.3, 2002
- [53] Yuvarajan, S.; Shanguang Xu; , "Photo-voltaic power converter with a simple maximum-power-point-tracker," *Circuits and Systems, 2003. ISCAS '03. Proceedings of the 2003 International Symposium on* , vol.3, no., pp. III-399- III-402 vol.3, 25-28 May 2003
- [54] Roman, E.; Alonso, R.; Ibanez, P.; Elorduizapatarietxe, S.; Goitia, D.; , "Intelligent PV Module for Grid-Connected PV Systems," *Industrial Electronics, IEEE Transactions on* , vol.53, no.4, pp.1066-1073, June 2006
- [55] Tse, K.K.; Ho, B.M.T.; Chung, H.S.-H.; Hui, S.Y.R.; , "A comparative study of maximum-power-point trackers for photovoltaic panels using switching-frequency modulation scheme," *Industrial Electronics, IEEE Transactions on* , vol.51, no.2, pp. 410- 418, April 2004
- [56] J.M. Enrique, E. Durn, M. Sidrach-de-Cardona, J.M. Andjar.; , "Theoretical assessment of the maximum power point tracking efficiency of photovoltaic facilities with different converter topologies, ", *Solar Energy*, vol. 81,pp. 31-38, Jan 2007
- [57] <http://www.cedd.gov.hk/eng/publications/geo-reports/doc/er194/er194links.pdf>.
- [58] LFO) Adel S. Sedra and Kenneth C. Smith, " *Microelectronic Circuits*, " fourth edition, Oxford university press.
- [59] DS1104 R&D Controller Board, <http://www.dspaceinc.com/en/inc/home/products/hw/singbord/ds1104.cfm> (Accessed August 2011).

- [60] International Rectifier Power MOSFET, (IRF540),  
<http://www.datasheetcatalog.org/datasheet/irf/irf540.pdf>  
(Accessed August 2011).
- [61] Compensated Devices Incorporated: switching Diode (IN4148),  
<http://pdf1.alldatasheet.com/datasheet-pdf/view/57418/CDI-DIODE/IN4148-1.html>  
(Accessed August 2011).
- [62] Duracell: Rechargeable Battery,  
<http://www.duracell.ca/en-CA/category/rechargeable-batteries-and-battery-chargers.jsp>  
(Accessed August 2011).
- [63] Vishay Semiconductors, Optocoupler (4N26),  
<http://www.vishay.com/docs/83725/4n25.pdf>  
(Accessed August 2011).
- [64] Fairchild Semiconductor, NPN Switching Transistor (PN2222A),  
<http://www.fairchildsemi.com/ds/PN/PN2222A.pdf>  
(Accessed August 2011).
- [65] <http://www.sensortech.ca/site/index.cfm?DSP=Page&ID=10>  
(accessed Sept 2011)
- [66] Diode Incorporated: Surface Mount Schottkey Barrier Diode (BAT43WS),  
<http://www.datasheetcatalog.org/datasheet/diodes/ds30100.pdf>  
(Accessed August 2011).
- [67] Vishay Semiconductor: Low Threshold Voltage (SI1563EDH),  
<http://www.datasheetcatalog.org/datasheet/vishay/71416.pdf>  
(Accessed August 2011).
- [68] Linear Technology: Op-amp (LT6004),  
<http://cds.linear.com/docs/Datasheet/600345fd.pdf>